creative commons

COMMONS DEED

저작자표시-비영리-변경금지 2.0 대한민국

이용자는 아래의 조건을 따르는 경우에 한하여 자유롭게

- 이 저작물을 복제, 배포, 전송, 전시, 공연 및 방송할 수 있습니다.

다음과 같은 조건을 따라야 합니다:

**저작자표시.** 귀하는 원저작자를 표시하여야 합니다.

**비영리.** 귀하는 이 저작물을 영리 목적으로 이용할 수 없습니다.

**변경금지.** 귀하는 이 저작물을 개작, 변형 또는 가공할 수 없습니다.

- 귀하는, 이 저작물의 재이용이나 배포의 경우, 이 저작물에 적용된 이용허락조건을 명확하게 나타내어야 합니다.
- 저작권자로부터 별도의 허가를 받으면 이러한 조건들은 적용되지 않습니다.

**저작권법에 따른 이용자의 권리는 위의 내용에 의하여 영향을 받지 않습니다.**

이것은 이용허락규약(Legal Code)을 이해하기 쉽게 요약한 것입니다.

Disclaimer

dCollection

공학박사 학위논문

# Stress relaxation-dependent piezoresistive behavior of carbon nanotube/polymer composite

## 탄소나노튜브/고분자 복합재료에서의 응력 완화에 따른 저항 변화

2020 년 8월

서울대학교 대학원

재료공학부

심 원 보

# Stress relaxation-dependent piezoresistive behavior of carbon nanotube/polymer composite

Advisor: Woong-Ryeol Yu

by

Wonbo Shim

2020

Department of Materials Science and
Engineering Graduated School Seoul
National University

# Stress relaxation-dependent piezoresistive behavior of carbon nanotube/polymer composite

탄소나노튜브/고분자 복합재료에서의 응력 완화에 따른 저항 변화

지도 교수 유 웅 열

이 논문을 공학박사 학위논문으로 제출함

**2020 년 6 월**

서울대학교 대학원

재료공학부

**심 원 보**

심원보의 공학박사 학위논문을 인준함

**2020 년 6 월**

| | | |
|---|---|---|
| 위 원 장 | 안 철 희 | (인) |
| 부위원장 | 유 웅 열 | (인) |
| 위 원 | 이 명 규 | (인) |
| 위 원 | 조 대 환 | (인) |
| 위 원 | 나 원 진 | (인) |

# Abstract

Carbon nanotubes (CNTs) have been investigated for many structural and electronic applications due to their excellent electrical and mechanical properties. Many studies have shown that CNT can be used as a reinforcement filler for polymer composites. In addition, CNT/polymer composites show the piezoresistive behavior, which makes them potentially applicable to strain sensing applications, e.g., an adhesive for structural health monitoring purposes. This study aimed to study the resistance changing behavior of CNT/polymer composites during stress relaxation and develop a new method of characterizing the residual stress. To achieve goals, a series of research was carried out as follows.

Predicting the mechanical behavior of adhesives is important, because adhesives strongly influence the strength and reliability of adhesive–adherend structures. The rate and temperature dependent mechanical behavior of an adhesive, including its failure strength was studied. We carried out a simulation of the mechanical behavior of an adhesive, including its failure strength, using Schapery's nonlinear viscoelastic model. A detailed derivation of the nonlinear viscoelastic model for 3D implementation in finite-element software was presented. Experimental procedures for obtaining the model

parameters from dynamic mechanical testing of lap-joint specimens were proposed. Strain-rate dependent failure criterion was employed using the shift factor and experimental lap shear tests at different strain rates to calculate the failure strain at different temperature. Then, the mechanical behavior of the adhesive in the adhesive joint at different rates and temperatures until its failure was simulated. The simulation results were compared with the experiments, demonstrating the validity of the current approach.

The electrical properties of CNT/graphene hybrids were studied. In this study, a predictive model that quantitatively describes the synergistic behavior of the CNTs and graphene to the electrical conductivity of CNT/graphene hybrids was proposed. The number of CNT-to-CNT, graphene-to-graphene and graphene-to-CNT contacts were calculated assuming random distribution of particles in the hybrids. The calculation showed optimum electrical conductivity at certain compositions. The calculation result was validated by measuring electrical conductivity of inkjet-printed CNT/graphene hybrids.

Lastly, the piezoresistive behavior of CNT/polymer composites during stress relaxation was studied. In this study, the dependence of CNT aspect ratio and concentration on the resistance change during stress relaxation was studied. The resistance was measured during stress relaxation of CNT/epoxy

composites. The resistance change varied according to different CNT aspect ratio and concentrations. To explain this behavior, a simulation model that was based on a new resistor model and the number of contacts between CNTs within tunneling distance was developed. This model can also explain the dependence of CNT aspect ratio and concentration on the resistance change during tensile test. CNT composite was used as an adhesive in this work, the residual stress of which was measured during cooling. The normal stress formed in the adhesive, which was obtained from numerical simulation result using viscoelastic model, showed a good agreement with experiments, suggesting that CNT composites can be used as an adhesive that can detect the residual stress change and can monitor structural health of joints.

Keywords: CNT/polymer composite, Piezoresistivity, viscoelasticity, stress relaxation, electrical conductivity

Student number: 2014-21444

# Contents

# List of Tables

# List of Figures

**Figure 3-3** The parallelepiped formed by a CNT $B$ $(\theta', \varphi')$ moving around a fixed CNT $A$ $(\theta, \varphi)$ while maintaining contact [135].

**Figure 3-4** A schematic drawing for calculating the contact probability of graphene particles $A$ and $B$. Mobile graphene particle $B$ will contact fixed particle $A$ when the center of mass of $B$ enters the region surrounded by the blue and red lines.

**Figure 3-5** A schematic diagram for explaining the contact condition of a CNT with graphene particle $A$. The CNT will contact $A$ when the center of mass of the CNT enters into the region surrounded by the dotted lines.

**Figure 3-6** Calculated number of contacts made by CNT and graphene particles in their hybrid assembly. (a) The number of CNT-to-CNT, graphene-to-graphene, and graphene-to-CNT contacts in the CNT/graphene hybrids as a function of the CNT content. In this system, 56.7 wt% is the CNT fraction that can bring about the maximum number of contacts in the modeled CNT/graphene hybrids. At this concentration, the proportion of graphene-to-CNT contact is the largest (75.0%), followed by CNT-to-CNT (19.2%), and graphene-to-graphene (5.8%) contacts. A synergistic behavior of CNT/graphene hybrids can be observed at this CNT content. (b) The effect of graphene particle radius and CNT diameter on CNT content at the maximum number of contacts. (c) The number of contacts calculated for different graphene and CNT sizes in (b).

**Figure 3-7** An example of a graph showing size distribution of CNTs

**Figure 3-8** The relation between aspect ratio of CNT and percolation threshold.

**Figure 3-9** Viscosities of (a) CNT ink and (b) graphene ink.

**Figure 3-10** Particle sizes of PAN-wrapped CNTs and graphene particles measured using DLS as a function of PAN content.

**Figure 3-11** Zeta potentials of PAN-wrapped CNTs and graphene particles measured using ELS as a function of PAN content.

**Figure 3-12** TGA curves of (a) CNT and (b) graphene inks.

**Figure 3-13** SEM images of graphene particles, CNTs, and their hybrid inks printed on photo paper. The scale bar is 500 nm in all images. (a) and (b): Graphene inks printed 3 and 15 times. The graphene particles were randomly deposited on the paper. The PAN molecules attached to the graphene gave a rough surface to the printed ink. The printed layer was densified as the number of printings increased. (c) and (d): CNT inks printed 3 and 15 times. The CNTs were randomly oriented and distributed on the substrate. (e) and (f): Morphologies of hybrid inks prepared with the CNT fractions of 12 and 81 wt% after printing 15 times. The graphene and CNT particles were randomly distributed and oriented by the inkjet printing process and had

# Chapter 1. Introduction

## 1.1. Carbon nanotube (CNT)

Carbon nanotubes (CNTs) were discovered by Iijima in 1991 [1]. After its discovery, for the past few decades, CNTs have been studied intensively due to their excellent electrical, mechanical, thermal properties [2-5]. CNTs can carry electric current density of about $10^{10}\mathrm{A/cm^2}$, which is much greater than other conductive metals [6] . Young's modulus and tensile strength of multiwalled carbon nanotubes (MWCNT) are about 270~950GPa and 11~63GPa respectively [7]. The strength of CNT results from strong sp2 bonding between carbon atoms [8]. Thermal conductivity of CNT along its axis is $3500\mathrm{W/m}\cdot\mathrm{K}$, which is about ten times higher than that of copper [9].

Carbon nanotube is a tube which is composed of layer of hexagonal lattice of carbon atoms. Electrical conductivity of CNT depends on the tube diameter and helicity of the tube lattice [10]. CNTs can be categorized by the number of walls they have. When CNT consists of only one wall, it is called single-walled carbon nanotubes (SWCNT). When CNT consists of more than one wall, it is called multi-walled carbon nanotubes (MWCNT). Double-walled carbon nanotube (DWCNT) is when MWCNT consists of two walls [11]. Figure 1-1 shows the structure of different types of CNTs. They have different material properties. It is difficult to use CNT by itself. CNTs have been processed into different forms such as yarns [12, 13], films

[14-17], polymer composites [18-21] etc.

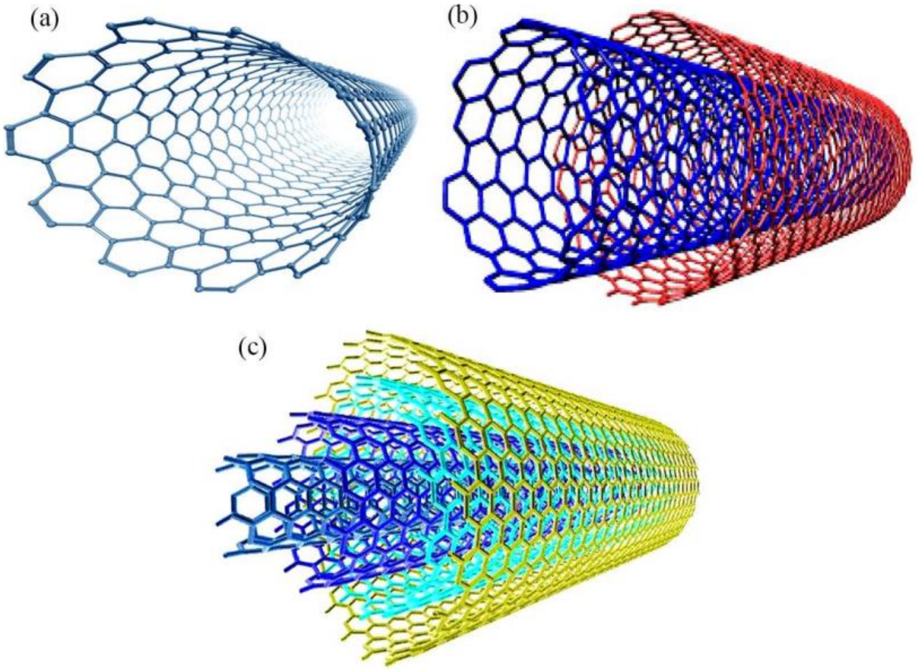

**Figure 1-1** Structure of (a) Single-walled carbon nanotubes, (b), Double-walled carbon nanotubes and (c) Multi-walled carbon nanotubes [11].

Thin films of CNTs are the most versatile form for applications such as supercapacitors [22], field-emission devices [23], and sensor devices [24]. Various processing methods have been developed to fabricate thin films from CNT solutions. The methods include filtration [14], dip coating, electrophoretic deposition [15] and inkjet printing [16, 25]. These solution-based processing methods are advantageous for large-scale and low-cost manufacturing. However, the fabricated films might have lower electrical properties due to poor contact resistance between CNTs. This problem can be solved by adding different types of conductive particles such as graphene [17, 25-27]. Enhanced properties than graphene films and CNT films were found in the CNT/graphene hybrid films. The improvement in the electrical conductivity by CNT/graphene hybridization was also found in fiber form [28, 29]. The mechanisms for this improvement are graphene particles filling the space between CNTs, and CNTs acting as bridge between graphene flakes [28, 30-33]. These explanations have common feature of an increased number of contacts between the graphene particles and the CNTs, which is proportional to the electrical conductivity [25].

CNT/polymer composites have been developed by many researchers for different purposes. CNT can be used as a reinforcing agent for polymers leading to better mechanical properties. Studies have shown that tensile strength and modulus increases when CNT is used as a filler [34-37]. CNT composite can be potentially used in lightweight flexible electronics due to its electrical conductivity [38-40]. Concentration, aspect ratio of CNTs, and how CNTs are dispersed in the resin affects the electrical conductivity of the CNT composites [19, 35-37, 41]. Electrical conductivity increases as CNT concentration and aspect ratio increases. Percolation threshold is proportional to the inverse of aspect ratio [25, 42]. Kovacs et al., have found that percolation threshold is higher when CNTs are more uniformly dispersed [41]. The flocculation of CNTs increases the network formation, leading to higher electrical conductivity. Tarlton et al., have explained the role of agglomeration on the electrical conductivity using simulation [43]. Studies have also found that resistance of CNT composite changes when it's under deformation. This piezoresistive behavior of CNT composite can be used in strain sensing applications.

## 1.2. Piezoresistive behavior of CNT composite

Studies have shown that CNT composites show piezoresistive behavior [18-21, 44, 45]. When CNT composite is under tensile deformation, the resistance changes as strain increases. Figure 1-2 shows an example of resistance change of CNT/epoxy composite with CNT concentration of 0.3wt% during cyclic tensile loading-unloading test [46]. Maximum strain in this example is 1.65% and the result showed that resistance increases as strain increases and resistance decreases as strain decreases. The maximum value of $\Delta \mathrm{R}/\mathrm{R}$ remained constant after number of cycles meaning that strain sensing ability is stable. The piezoresistivity of the CNT composite can be defined using gauge factor $K$ as:

$$K = \frac{\Delta R/R_0}{\varepsilon} \qquad (1)$$

where $R_0, \Delta R$ and $\varepsilon$ are the initial resistance, the resistance change and the applied strain respectively [47]. Studies have found that gauge factor differs with concentration of CNTs in the composite [47-50]. Tallman et al. have explained the reason for the lower gauge factor at higher CNT concentrations [50]. They explained that distance between CNTs are smaller at higher concentration and that this leads to smaller change in tunneling resistance when strain is applied. Using these facts, gauge factor of CNT can be controlled to the wanted values by controlling the CNT concentrations. Due to piezoresistive behavior of CNT composites, CNT composites can be potentially applicable for structural health monitoring which can provide real-time measurement data of the deformation and damage of the structure [46].

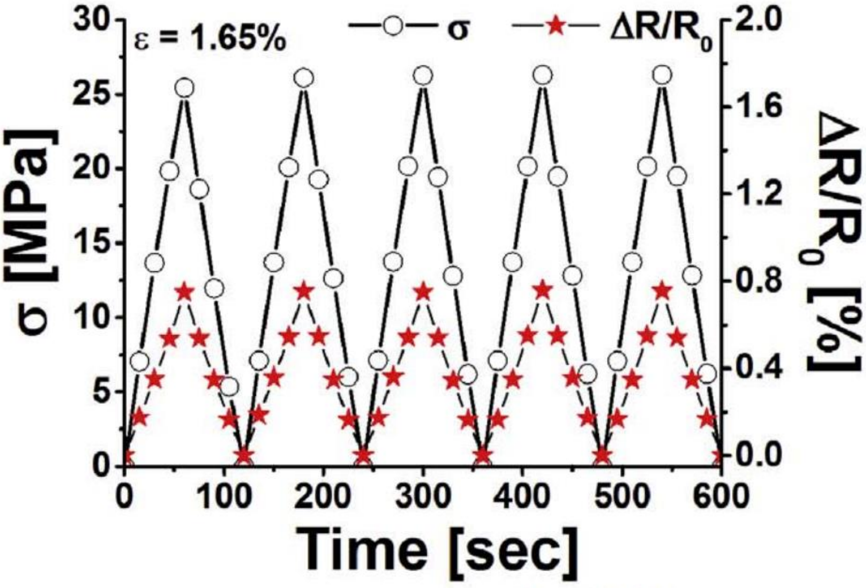

**Figure 1-2** Resistance change of CNT composite during cyclic tensile loading-unloading test [46]

Electrical conductivity of CNT assembly is mostly determined by the resistance at CNT-CNT junctions. Nirmalraj et al., have measured intrinsic resistance of a CNT and the resistance between two CNTs in contact using conductance atomic force microscopy (C-AFM) [51]. They have shown that junction resistance between CNTs is much higher than intrinsic resistance of CNT. In case of CNT/polymer composites, the distance between two adjacent CNTs in the conducting path can be larger. Tunneling effect, which is the electron hopping through the insulating polymer matrix between CNTs, occurs in CNT/polymer composites [52]. This is the main mechanism underlying the electrical conductivity of CNT composites. The tunneling resistance between two CNTs can be expressed as:

$$R_{tunnel} = \frac{h^2 d}{Ae^2\sqrt{2m\Psi}} \exp\left(\frac{4\pi\sqrt{2m\Psi}}{h} d\right) \qquad (2)$$

where $h$, $\Psi$, $A$, $m$, and $d$ are Planck's constant, CNT work function, contact area, mass of the electron, and distance between two CNTs. It can be seen from Equation (2) that tunneling resistance is highly dependent on the distance between CNTs.

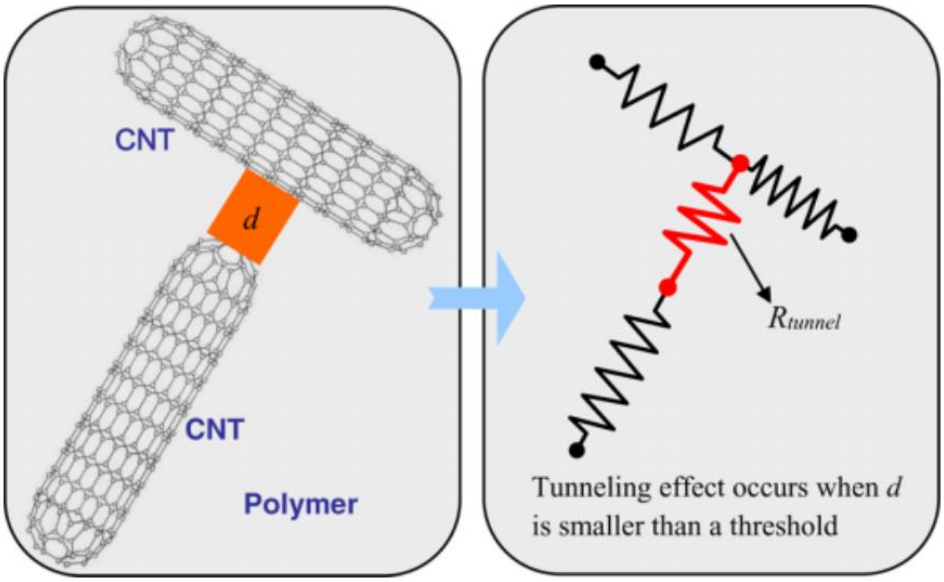

**Figure 1-3** Schematic diagram of tunneling effect of two neighboring CNTs in CNT/polymer composite [53].

When CNT composite is under deformation, center of CNTs inside the matrix moves equal to that of polymer matrix at the same position and rotation of the CNT also occurs due to deformation of surrounding polymer matrix [54]. Due to changes in CNT position and orientation, the distance between CNTs also changes. Figure 1-4 shows a schematic image of mechanism of piezoresistive behavior of CNT/polymer composite [47]. Changes in tunneling distance have huge influence on the tunneling resistance as in Equation (2). Therefore, since the tunneling resistance is highly related to the overall resistance of CNT, the distance change between CNTs can be said as the main mechanism for the piezoresistivity of CNT composite [18, 55-57].

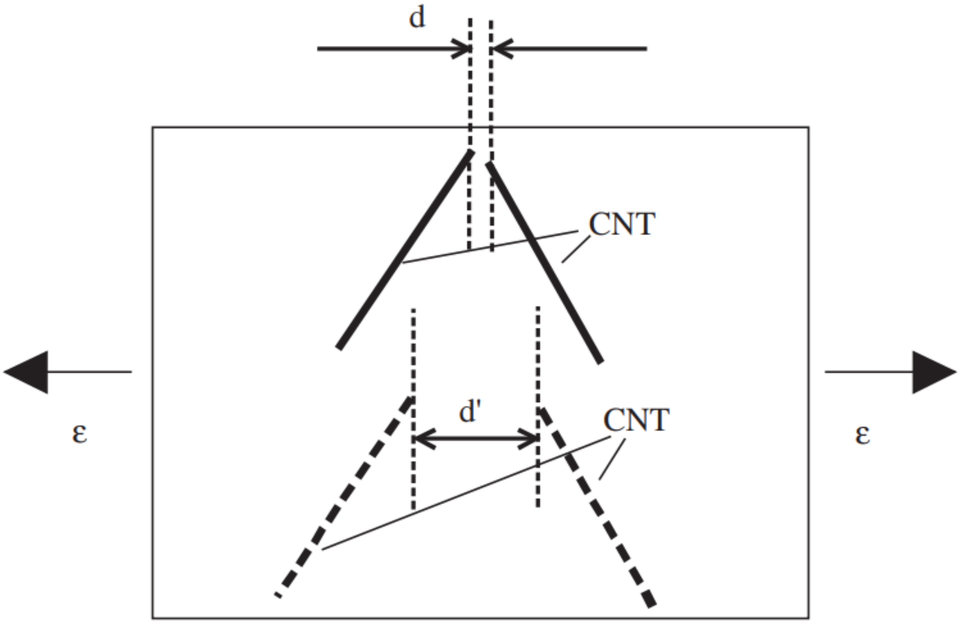

**Figure 1-4** Schematic image of mechanism of piezoresistive behavior of CNT/polymer composite [47].

Studies have found that resistance of CNT composite also changes during stress relaxation test [58-61]. Stress decreases with time when the strain of CNT composite is fixed at certain level. They have shown that resistance also changes as stress decreases. Mechanism of resistance change during stress relaxation is unclear. It has been proposed that during stress relaxation, rearrangement of polymer chains occurs, which disrupts the conductive filler network [61]. The changes in conductive filler network leads to change in the tunneling distance between CNTs and as a result, the overall resistance changes.

## 1.3. Research objectives

In this study, the main objective is to model the electrical resistance change during stress relaxation of CNT composite. A model to calculate electrical conductivity of CNT/graphene hybrids was also proposed, which can be applied in calculating piezoresistive behavior of CNT composites. This study also proposed a method to simulate behavior of an adhesive using nonlinear viscoelastic model.

In chapter 2, rate(time) and temperature dependent adhesive property was simulated using nonlinear viscoelastic model. Methods for implementing finite-element modeling of Schapery's nonlinear viscoelastic model with strain-dependent parameters proposed. Parameters for nonlinear viscoelastic model were obtained from stress relaxation tests of lap joint specimens at various strains above linear viscoelastic limit. The time-temperature dependence of the adhesive was obtained from results of dynamic mechanical analysis tests (DMA). Time-temperature superposition of the storage modulus data gave master curve, and shift factor was obtained during this procedure. Relationship between time-to-failure and strain rate which is obtained from the lap shear test was fitted using Monkman-Grant equation. This equation was used as the failure criterion. Reduced strain rate was used in this equation so that it can be used to calculate failure strain at different temperatures. The adhesive behavior, including the stress-strain curve and failure strength at different strain rates and temperatures, were simulated by using nonlinear viscoelastic model and Monkman-Grant equation. The simulated results were validated experimentally.

In chapter 3, the synergistic behavior in electrical properties of CNT/graphene hybrid was studied experimentally and theoretically. Since the electrical conductivity is proportional to the number of contacts between the conductive particles, a predictive model that can calculate the number of contacts was developed. CNT-to-CNT, graphene-to-graphene and graphene-to-CNT contacts at different compositions were calculated using this model assuming the particles were distributed and oriented randomly. Total number of contacts reached maximum at a specific composition and it depended on the particle sizes of the graphene and CNTs. To validate this result, conductivity of CNT/graphene hybrids prepared using inkjet printing at different compositions were measured. At certain composition ratios, higher electrical conductivity than that of 100% CNT or graphene was found. These experimental results show that this calculation approach involving constituent element contacts is suitable for investigating the properties of particulate hybrid materials.

In chapter 4, piezoresistive behavior of CNT/polymer composite during stress relaxation was studied. CNT composite was made using epoxy resin and CNT. CNT of two different aspect ratios were used. Resistance change of CNT composite during stress relaxation were measured and the results showed that the resistance change depends strongly on the concentration and aspect ratio of CNTs. At low concentration, the resistance increased during stress relaxation. However, at high concentration, resistance decreased during stress relaxation. The concentration where this trend changes is lower when high aspect ratio CNT is used. To investigate this mechanism, a new resistor model was developed which considers multiple pathways merging into one conducting path. The number of contacts between CNTs were calculated. Changes in tunneling resistance during stress relaxation was simulated, assuming the orientation of CNTs changes during stress relaxation. Using the proposed model and the simulated results, the resistance change of the conducting path at various concentrations and aspect ratios was calculated. The calculated results showed similar behavior to the experimental results. At low concentration, the number of contacts between CNTs at a low concentration is not enough to form alternative conducting pathways, therefore, increased tunneling resistance had more influence on the overall resistance than the decreased tunneling resistance due to multiple conducting pathways. At higher concentration, influence of decreased tunneling resistance is greater. This model was validated by analyzing aspect ratio and concentration dependence of resistance during tensile test. CNT composite is used as an adhesive to measure residual stress during cooling. The residual stress was measured by measuring the resistance change. The result was validated by simulation result using viscoelastic model.

# Chapter 2. Nonlinear viscoelastic property of adhesive

## 2.1. Introduction

Adhesives are used in many areas such as in aerospace and automotive industries since it can reduce the weight of a structure [62-64]. Shock absorbing and vibration damping abilities can also be improved by using an adhesive for the joint [65]. There are advantages to using adhesives instead of welding or riveting to make joints. For example, stresses can be more uniformly distributed in the bonding area, thereby reducing the risk of failure due to stress concentration. However, when using an adhesive instead of welding or riveting, the adhesive should be sufficiently strong to ensure a stable joint structure. Additionally, adhesives used in aerospace or automotive applications are exposed to various environmental conditions and are subject to widely ranging strain rates and temperatures; the adhesives must be able to endure these environments. Predicting adhesive behavior in adhesive joints in different environments using numerical simulations will greatly assist adhesive design and application.

Adhesives are typically made of viscoelastic polymers such that their properties are time (rate)- and temperature-dependent; a viscoelastic model can describe this behavior. Additionally, the time (rate) and temperature dependence of mechanical properties such as dynamic modulus and failure strength can be analyzed using time–

temperature superposition [63, 66-71]. Adhesive behavior has been described extensively using different types of viscoelastic models, especially the linear viscoelastic model [72-75]. This model provides information on the behavior of the polymer only over a small strain range. However, adhesive failure occurs at high strains that are outside the linear viscoelastic range; a nonlinear model is needed to describe adhesive behavior at these high strains [75, 76]. Various nonlinear viscoelastic models have been reported, among which Schapery's model is the most commonly used [77, 78]. This model uses creep compliance with stress-dependent parameters or relaxation modulus with strain-dependent parameters. The applicability of nonlinear viscoelastic model in high strain can be found in literatures [79-82]. Spathis and Kontou simulated stress-strain behavior of high damping rubber using nonlinear viscoelastic model at shear strain level of about 250% [79]. Liu and Bilston have used nonlinear viscoelastic model to simulate behavior of liver tissue at strain level up to about 1000% [80]. Xu and Engquist simulated stress-strain behavior of hydrogel using nonlinear viscoelastic model up to strain level of 700% [82]. These researches show that nonlinear viscoelastic model can be used to simulate material behavior at very high strain. However, these researches only showed nonlinear viscoelastic behavior at various strain ranges, and the failure of the material at different temperature and strain rates wasn't simulated.

The cohesive zone model is also frequently used to predict adhesive behavior [83-87]. The failure strength, fracture toughness, and elastic modulus (modes I and II) are needed to implement the traction–separation law. Adhesive properties change with changing strain rate or temperature. Thus, the mechanical properties at different strain rates and temperatures are required to simulate adhesive behavior using the cohesive zone model [83, 87, 88]. To avoid the high experimental cost associated with the cohesive zone model, a viscoelastic model was chosen for the adhesive finite-element simulation in this study because it can be directly implemented as an adhesive element.

Herein, we propose a method for implementing finite-element modeling of Schapery's model with strain-dependent parameters. Schapery's model was implemented in ABAQUS software via the user-defined material subroutine (UMAT). The parameters for this nonlinear viscoelastic model were obtained from stress relaxation tests of lap-joint specimens at various strains. The time–temperature dependence of the adhesive was obtained from dynamic mechanical analysis (DMA) shift factors. Monkman-Grant equation which is a relationship between time-to-failure and strain rate was used as the failure criterion. In fact, the reduced strain rate was used in this equation so that it can calculate failure strain at different temperatures as well. By using nonlinear viscoelastic model and Monkman-Grant equation, the adhesive behavior, including the stress–strain curve and failure strength at different strain rates and temperatures, was simulated and validated experimentally.

## 2.2. Experiment

### 2.2.1. Materials and specimen

A polyurethane-based two-component adhesive was used in the experiments. Resin and hardener were mixed at the weight ratio of 2:1 and cured at 60°C for 10 min, and then at 25°C for 3–4 days. Steel (SAPH440) with a thickness of 3 mm was used as the adherend. The elastic modulus and yield strength of the steel were 180 GPa and 384 MPa, respectively.

### 2.2.2. Characterization

#### 2.2.2.1 Dynamic mechanical analysis

Dynamic mechanical analysis was used to measure the time–temperature dependency (shift factor) of the adhesive. The width, thickness, and length of the bulk adhesive specimens were 4, 1, and 25 mm, respectively. A temperature–frequency sweep was used to measure the dynamic modulus. The test temperature ranged from –60°C to 70°C, and the frequency from 0.1 to 100/s.

#### 2.2.2.2 Lap shear test

The single lap shear test was used to determine the shear properties of the adhesive. A universal tensile testing machine with a temperature-controlled chamber (QUASAR 5; Galdabini, Italy) was used. The maximum load capacity of the testing machine was 5,000 N, which was insufficient to measure the failure strength of the adhesive in the lap-joint specimens prepared according to the dimensions provided in the standard ASTM D1002. Hence, lap-joint specimens with smaller bonded areas were used in this study. Steel with length and width of 101.6 and 12.7 mm, respectively, was used. The length and width of the bonded area was 6.35 and 12.7 mm, respectively, and the thickness of the adhesive was about 0.5 mm.

The single-lap shear testing was carried out at temperatures ranging from –10°C to 60°C and deformation rate ranging from 0.0005 to 3 mm/s. The nonlinear viscoelasticity of the adhesive was determined by stress relaxation testing of the lap-joint specimens at shear strains ranging from 0.091 to 1.136. The shear strain used in this work was the engineering shear strain since the deflection of steel was negligible due to large difference in the modulus between the adhesive and the steel. The shear strain was calculated by dividing displacement of the steel adherend by the thickness of the adhesive.

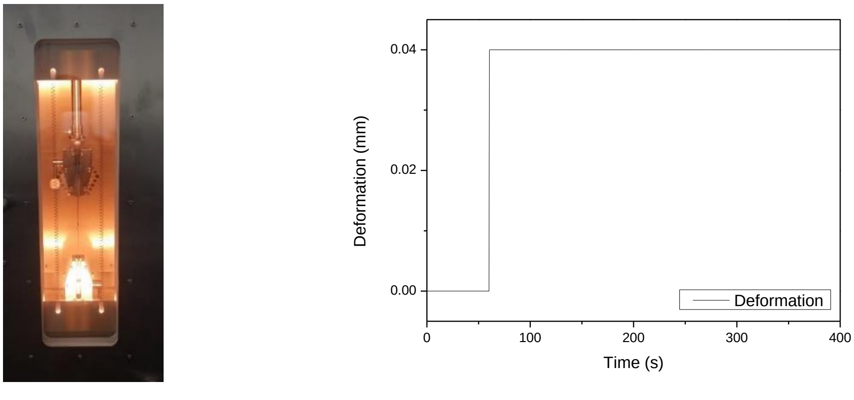

(a) (b)

**Figure 2-1** (a) Lap shear test was performed in a temperature-controlled chamber. (b) Test condition of the stress relaxation test.

## 2.3. Model formulation and implementation

### 2.3.1. One-dimensional nonlinear viscoelastic model

A nonlinear model is briefly introduced for the simulation of adhesive behavior. The constitutive equations for uniaxial tensile loading of a linear viscoelastic material can be expressed as:

$$\sigma(t) = E_\infty \varepsilon + \int_0^t \Delta E(t - t') \frac{d\varepsilon}{dt'} dt' \qquad (3)$$

where $E_\infty$ and $\Delta E$ are the long-term relaxation modulus and transient component of the relaxation modulus, respectively, which vary with time [89]. For a nonlinear viscoelastic model, more parameters are needed to express the material's dependency on strain or stress. Schapery [77] developed a nonlinear viscoelastic model that enables the material properties to be expressed in terms of stress or strain. Herein, we used Schapery's model for the simulation because it is strain-dependent. Schapery's model for one-dimensional uniaxial tensile loading can be expressed as:

$$\sigma(t) = h_0 E_\infty \varepsilon + h_1 \int_0^t \Delta E(\rho(t) - \rho(t')) \frac{d(h_2 \varepsilon)}{dt'} dt' \qquad (4)$$

where $E_\infty$ and $\Delta E$ are the material properties defined in the linear viscoelastic model and $\rho(t)$, $h_0$, $h_1$, and $h_2$ are parameters that depend on the strain. $\rho(t)$ is the reduced time, defined as:

$$\rho(t) = \int_0^t \frac{dt'}{a_\varepsilon} \qquad (5)$$

and the nonlinear terms $h_0$, $h_1$, $h_2$, and $a_\varepsilon$ are functions of strain. Changes in $h_0$ show the changes in the long term modulus ( $E_\infty$ ) in Prony series. Changes in $h_1$ and $h_2$ show the changes in the transient component of the Prony series $E_1$~ $E_n$. Changes in $a_\varepsilon$ is related to changes in the reduced time $\rho(t)$. Changes in $h_0$, $h_1$ and $h_2$ are due to third and higher order strain effects onn the Helmholtz free energy, while changes in $a_\varepsilon$ arise from similar strong strain influences on both entropy production and free energy [77, 90]. At small strain, the values of $h_0$, $h_1$, $h_2$, and $a_\varepsilon$ become 1, leading to the linear viscoelastic model of Equation (3).

Herein, a Prony series, which can be obtained from the generalized Maxwell model, was used for the viscoelastic model [91]. The transient component of the relaxation modulus becomes:

$$\Delta E(t) = \sum_{n=1}^{N} E_n \exp\left( -\frac{t}{\tau_n} \right) \qquad (6)$$

where $E_n$ and $r_n$ are constants that can be obtained by fitting to the stress relaxation test results. Using the Prony series as the viscoelastic model, Schapery's model in Equation (4) can be expressed as:

$$\sigma(t) = h_0 E_\infty \varepsilon + h_1 \sum_{n=1}^{N} \int_0^t E_n \exp\left( -\frac{\rho(t) - \rho(t')}{\tau_n} \right) \frac{d(h_2 \varepsilon)}{dt'} dt' \qquad (7)$$

### 2.3.2. Three-dimensional nonlinear viscoelastic model

To use Schapery's model in the numerical simulation of adhesives, a three-dimensional (3D) form of the model was derived assuming that the material is isotropic, and that the adhesive's volumetric and deviatoric responses are uncoupled [92]. The stress can be divided into its volumetric and deviatoric components as follows:

$$\sigma_{ij} = \frac{1}{3} \delta_{ij} \sigma_{kk} + S_{ij} \qquad (8)$$

where $\frac{1}{3} \delta_{ij} \sigma_{kk}$ is the volumetric stress and $S_{ij}$ is the deviatoric stress. Then, the volumetric stress in Schapery's model can be expressed as:

$$\frac{1}{3} \sigma_{kk} = h_0 \frac{1}{3} \sigma_{kk}{}^{0}(t) + h_1 \sum_{n=1}^{N} \frac{1}{3} \sigma_{kk}{}^{n}(t) \qquad (9)$$

where

$$\frac{1}{3} \sigma_{kk}{}^{0}(t) = K_0 \varepsilon_{kk}(t) \qquad (10)$$

and

$$\frac{1}{3}\sigma_{kk}{}^{n}(t) = \int_0^t K_n \exp\left(-\frac{\rho(t)-\rho(t')}{\tau_n}\right)\frac{dh_2\varepsilon_{kk}}{dt'}dt' \qquad (11)$$

Similarly, the deviatoric stress is given by:

$$S_{ij} = h_0 S_{ij}{}^{0}(t) + h_1 \sum_{n=1}^{N} S_{ij}{}^{n}(t) \qquad (12)$$

where

$$S_{ij}{}^{0}(t) = G_0 \gamma_{ij}(t) \qquad (13)$$

and

$$S_{ij}{}^{n}(t) = \int_0^t G_n \exp\left(-\frac{\rho(t)-\rho(t')}{\tau_n}\right)\frac{dh_2\gamma_{ij}}{dt'}dt' \qquad (14)$$

### 2.3.3. Algorithm to update stress and tangent stiffness

Increments for the volumetric and deviatoric stress components were required to implement the 3D form of the Schapery model into the finite-element software. The increments of the two stress components of the volumetric stress, i.e., $\frac{1}{3}\sigma_{kk}{}^{0}(t)$ and $\frac{1}{3}\sigma_{kk}{}^{n}(t)$, are derived below. The increment of the $\frac{1}{3}\sigma_{kk}{}^{0}(t)$ stress component is expressed as follows:

$$\frac{1}{3}\Delta\sigma_{kk}{}^{0}(t) = K_0(\varepsilon_{kk}(t) - \varepsilon_{kk}(t-\Delta t)) = K_0\Delta\varepsilon_{kk}(t) \qquad (15)$$

where $\varepsilon_{kk}(t)$ and $\varepsilon_{kk}(t-\Delta t)$ are the volumetric strains from the current and previous steps, respectively. $\Delta\varepsilon_{kk}(t)$ is the increment of the volumetric strain. The increment of the $\frac{1}{3}\Delta\sigma_{kk}{}^{n}(t)$ stress component is derived by the following procedure. Equation (11) can be rewritten as follows:

$$\begin{aligned} &\frac{1}{3}\sigma_{kk}{}^{n}(t) \\ &= \int_0^{t-\Delta t} K_n \exp\left(-\frac{\rho(t)-\rho(t')}{\tau_n}\right)\frac{dh_2\varepsilon_{kk}}{dt'}dt' + \int_{t-\Delta t}^{t} K_n \exp\left(-\frac{\rho(t)-\rho(t')}{\tau_n}\right)\frac{dh_2\varepsilon_{kk}}{dt'}dt' \end{aligned} \qquad (16)$$

Equation (16) indicates volumetric stress due to nth transient component of relaxation modulus in Prony series. To implement second integral on the right side of Equation (16), assumptions should be made for changing parameters.

Lai and Bakker assumed stress dependent nonlinear parameter $g_2$ to remain constant and stress $\sigma$ to change linearly during time step between $t-\Delta t$ and $t$ when calculating strain due to nth transient component of creep compliance in Prony series [92]. However, this give wrong results when calculating $d(g_2\sigma)/dt$ in time step between $t-\Delta t$ and $t$. Its value is very different from its value when changes in nonlinear parameter is considered. In our work, we assumed both the volumetric strain $\varepsilon_{kk}$ and nonlinear parameter $h_2$ to change linearly during time step between $t-\Delta t$ and $t$ for more precise calculation. With these assumptions, Equation (16) can be expressed as follows:

$$\begin{aligned}
&\frac{1}{3}\sigma_{kk}{}^{n}(t) \\
&=\int_{0}^{t-\Delta t}K_n\exp\left(-\frac{\rho(t)-\rho(t')}{\tau_n}\right)\frac{dh_2\varepsilon_{kk}}{dt'}dt'+\int_{\rho(t-\Delta t)}^{\rho(t)}K_n\exp\left(-\frac{\rho(t)-\rho(t')}{\tau_n}\right)\frac{dh_2\varepsilon_{kk}}{d\rho(t')}d\rho(t') \\
&=\exp\left(-\frac{\Delta\rho}{\tau_n}\right)\int_{0}^{t-\Delta t}K_n\exp\left(-\frac{\rho(t)-\Delta\rho-\rho(t')}{\tau_n}\right)\frac{dh_2\varepsilon_{kk}}{dt'}dt'+K_n\tau_n\left(1-\exp\left(-\frac{\Delta\rho}{\tau_n}\right)\right)\frac{\Delta(h_2\varepsilon_{kk})}{\Delta\rho} \\
&=\exp\left(-\frac{\Delta\rho}{\tau_n}\right)\frac{1}{3}\sigma_{kk}{}^{n}(t-\Delta t)+K_n\tau_n\left(1-\exp\left(-\frac{\Delta\rho}{\tau_n}\right)\right)\frac{\Delta(h_2\varepsilon_{kk})}{\Delta\rho}
\end{aligned} \tag{17}$$

where

$$\Delta\rho=\rho(t)-\rho(t-\Delta t) \tag{18}$$

The increment of the $\frac{1}{3}\sigma_{kk}{}^{n}(t)$ stress component is derived from Equation (17) as follows:

$$\begin{aligned}
\frac{1}{3}\Delta\sigma_{kk}{}^{n}(t)&=\frac{1}{3}\sigma_{kk}{}^{n}(t)-\frac{1}{3}\sigma_{kk}{}^{n}(t-\Delta t) \\
&=\left(\exp\left(-\frac{\Delta\rho}{\tau_n}\right)-1\right)\frac{1}{3}\sigma_{kk}{}^{n}(t-\Delta t)+K_n\tau_n\left(1-\exp\left(-\frac{\Delta\rho}{\tau_n}\right)\right)\frac{\Delta(h_2\varepsilon_{kk})}{\Delta\rho}
\end{aligned} \tag{19}$$

The increments of the two stress components of the deviatoric stress, i.e., $S_{ij}{}^{0}(t)$ and $S_{ij}{}^{n}(t)$, are derived using the same procedure. The increment of the $S_{ij}{}^{0}(t)$ stress component is expressed as follows:

$$\Delta S_{ij}{}^{0}(t) = G_0 \Delta\gamma_{ij}(t) \qquad (20)$$

The $S_{ij}{}^{n}(t)$ stress component from Equation (14) can be rewritten as follows:

$$\begin{aligned}
&S_{ij}{}^{n}(t) \\
&= \int_0^{t-\Delta t} G_n \exp\left( -\frac{\rho(t)-\rho(t')}{\tau_n} \right) \frac{dh_2\gamma_{ij}}{dt'} dt' + \int_{t-\Delta t}^{t} G_n \exp\left( -\frac{\rho(t)-\rho(t')}{\tau_n} \right) \frac{dh_2\gamma_{ij}}{dt'} dt' \\
&= \int_0^{t-\Delta t} G_n \exp\left( -\frac{\rho(t)-\rho(t')}{\tau_n} \right) \frac{dh_2\gamma_{ij}}{dt'} dt' + \int_{\rho(t-\Delta t)}^{\rho(t)} G_n \exp\left( -\frac{\rho(t)-\rho(t')}{\tau_n} \right) \frac{dh_2\gamma_{ij}}{d\rho(t')} d\rho(t') \\
&= \exp\left( -\frac{\Delta\rho}{\tau_n} \right) \int_0^{t-\Delta t} G_n \exp\left( -\frac{\rho(t)-\Delta\rho-\rho(t')}{\tau_n} \right) \frac{dh_2\gamma_{ij}}{d\tau} d\tau + G_n\tau_n \left( 1-\exp\left( -\frac{\Delta\rho}{\tau_n} \right) \right) \frac{\Delta(h_2\gamma_{ij})}{\Delta\rho} \\
&= \exp\left( -\frac{\Delta\rho}{\tau_n} \right) S_{ij}{}^{n}(t-\Delta t) + G_n\tau_n \left( 1-\exp\left( -\frac{\Delta\rho}{\tau_n} \right) \right) \Delta(h_2\gamma_{ij})
\end{aligned} \qquad (21)$$

From Equation (21), the increment of the $S_{ij}{}^{n}(t)$ stress component is derived as follows:

$$\begin{aligned}
\Delta S_{ij}{}^{n}(t) &= S_{ij}{}^{n}(t) - S_{ij}{}^{n}(t-\Delta t) \\
&= \left( \exp\left( -\frac{\Delta\rho}{\tau_n} \right) - 1 \right) S_{ij}{}^{n}(t-\Delta t) + G_n\tau_n \left( \exp\left( -\frac{\Delta\rho}{\tau_n} \right) - 1 \right) \frac{\Delta(h_2\gamma_{ij})}{\Delta\rho}
\end{aligned} \qquad (22)$$

For simplification, new terms $g_n$, $k_n$, and $A_n$ are defined according to Equations (23), (24), and (25), respectively, as follows:

$$g_n = \frac{G_n\tau_n}{\Delta\rho} \left( 1-\exp\left( -\frac{\Delta\rho}{\tau_n} \right) \right) \qquad (23)$$

$$k_n = \frac{K_n \tau_n}{\Delta\rho}\left(1 - \exp\left(-\frac{\Delta\rho}{\tau_n}\right)\right) \qquad (24)$$

$$A_n = \exp\left(-\frac{\Delta\rho}{\tau_n}\right) - 1 \qquad (25)$$

Since the material is assumed to be isotropic, the stress increment of each stress component is updated as follows:

$$\boldsymbol{\Delta\sigma}^0(t) = (G_\infty \mathbf{M_D} + K_\infty \mathbf{M_V})\boldsymbol{\Delta\varepsilon}(t) \qquad (26)$$

$$\boldsymbol{\Delta\sigma}^n(t) = (g_n \mathbf{M_D} + k_n \mathbf{M_V})\Delta(h_2 \boldsymbol{\varepsilon}(t)) + A_n(\boldsymbol{\sigma_D}^n(t-\Delta t) + \boldsymbol{\sigma_V}^n(t-\Delta t)) \qquad (27)$$

The components of Equations (26) and (27) are described by Equations (28) to (34):

$$\mathbf{M_V} = \begin{bmatrix} 1 & 1 & 1 & 0 & 0 & 0 \\ 1 & 1 & 1 & 0 & 0 & 0 \\ 1 & 1 & 1 & 0 & 0 & 0 \\ 0 & 0 & 0 & 0 & 0 & 0 \\ 0 & 0 & 0 & 0 & 0 & 0 \\ 0 & 0 & 0 & 0 & 0 & 0 \end{bmatrix} \qquad (28)$$

$$\mathbf{M_D} = \begin{bmatrix} \frac{4}{3} & -\frac{2}{3} & -\frac{2}{3} & 0 & 0 & 0 \\ -\frac{2}{3} & \frac{4}{3} & -\frac{2}{3} & 0 & 0 & 0 \\ -\frac{2}{3} & -\frac{2}{3} & \frac{4}{3} & 0 & 0 & 0 \\ 0 & 0 & 0 & 1 & 0 & 0 \\ 0 & 0 & 0 & 0 & 1 & 0 \\ 0 & 0 & 0 & 0 & 0 & 1 \end{bmatrix} \qquad (29)$$

$$\boldsymbol{\sigma} = (\sigma_{11} \quad \sigma_{22} \quad \sigma_{33} \quad \sigma_{12} \quad \sigma_{13} \quad \sigma_{23})^T \qquad (30)$$

$$\boldsymbol{\Delta\varepsilon} = (\Delta\varepsilon_{11} \quad \Delta\varepsilon_{22} \quad \Delta\varepsilon_{33} \quad \Delta\gamma_{12} \quad \Delta\gamma_{13} \quad \Delta\gamma_{23})^T \qquad (31)$$

$$\boldsymbol{\Delta}(h_2\boldsymbol{\varepsilon}) = (\Delta(h_2\varepsilon_{11}) \quad \Delta(h_2\varepsilon_{22}) \quad \Delta(h_2\varepsilon_{33}) \quad \Delta(h_2\gamma_{12}) \quad \Delta(h_2\gamma_{13}) \quad \Delta(h_2\gamma_{23}))^T \quad (32)$$

$$\boldsymbol{\sigma}_{\mathbf{V}}{}^{n}(t) = \exp\left(-\frac{\Delta\rho}{\tau_n}\right)\boldsymbol{\sigma}_{\mathbf{V}}{}^{n}(t-\Delta t) + k_n \mathbf{M_V}\Delta(h_2\boldsymbol{\varepsilon}(t)) \qquad (33)$$

$$\boldsymbol{\sigma}_{\mathbf{D}}{}^{n}(t) = \exp\left(-\frac{\Delta\rho}{\tau_n}\right)\boldsymbol{\sigma}_{\mathbf{D}}{}^{n}(t-\Delta t) + g_n \mathbf{M_D}\Delta(h_2\boldsymbol{\varepsilon}(t)) \qquad (34)$$

Each stress component is updated according to Equations (35) and (36). The strain-dependent nonlinear parameters *h0* and *h1* are multiplied by each stress component and added together to obtain the final stress.

$$\boldsymbol{\sigma}^0(t) = \boldsymbol{\sigma}^0(t-\Delta t) + \boldsymbol{\Delta\sigma}^0(t) \qquad (35)$$

$$\boldsymbol{\sigma}^{\mathbf{n}}(t) = \boldsymbol{\sigma}^n(t-\Delta t) + \boldsymbol{\Delta\sigma}^n(t) \qquad (36)$$

$$\boldsymbol{\sigma}(t) = h_0 \boldsymbol{\sigma}^0(t) + h_1 \sum_{n=1}^{N} \boldsymbol{\sigma}^n(t) \qquad (37)$$

The Jacobian matrix must be defined in the ABAQUS UMAT. Herein, the Jacobian matrix is defined as follows:

$$\mathbf{J}(t) = h_0 (G_\infty \mathbf{M_D} + K_\infty \mathbf{M_V}) + h_1 (g_n \mathbf{M_D} + k_n \mathbf{M_V}) \qquad (38)$$

When described in this way, the Jacobian matrix is sufficient to ensure good convergence of the simulation.

### 2.3.4. Implementation of failure criteria

In this study, a failure criterion which is dependent on strain rate is used. Failure occurs when strain exceeds failure strain. The failure strain is dependent on the strain rate and is obtained from a relationship between time-to-failure and strain rate. This relationship is obtained from experiment using Monkman-Grant equation as follows [93].

$$t_f \left(\dot{\varepsilon}\right)^m = C \qquad (39)$$

where $t_f$ is time-to-failure and $m$ and $C$ are constants obtained by fitting the experimental data. The detailed procedure to get the parameters in Monkman-Grant equation is discussed in section 4.3. On the other hand, since the reduced strain rate at reference temperature ($T_0$) is equivalent to the strain rate at tested temperature ($T$) multiplied by the shift factor ($a_T$), the reduced strain rate is used in the implementation. The reduced strain rate can be expressed as follows [62, 66-68, 71].

$$\dot{\varepsilon}_{red}(T_0) = \dot{\varepsilon}(T)a_T \qquad (40)$$

By using Monkman-Grant equation, failure strain ($\varepsilon_f$) at different reduced strain rate can be calculated as follows:

$$\varepsilon_f = \dot{\varepsilon}_{red} t_f = \left(\dot{\varepsilon}_{red}\right)^{1-m} C \qquad (41)$$

Using Equation (41), failure strain at different strain rates and temperature can be calculated. Constants in Monkman-Grant are obtained from lap shear test results at different strain rates.

Temperature and strain rate determine failure strain, which is used in the maximum shear strain criterion. In UMAT subroutine, the strain rate of the adhesive and the following failure strain are calculated. When the maximum shear strain of an element of the adhesive reaches the failure strain, it indicates where the failure starts. We indicate elements that have reached the failure strain using a state variable to distinguish it from elements that have not reached the failure strain yet. Elements that haven't reached the failure strain is saved in the state variable as 0, while elements that have reached failure strain is saved as 1. The failure strength is reached when adhesive element that reached failure strain is found. As a result, in ABAQUS implementation, the behavior of adhesive was simulated until adhesive element that reached failure strain was found.

### 2.3.5. Parameters for the numerical simulation

All of the parameters for the numerical simulation were obtained experimentally, as follows: $G_\infty$, $G_1 \sim G_N$, $K_\infty$, $K_1 \sim K_N$, $\tau_1 \sim \tau_N$, $a_\varepsilon$, $h_0$, $h_1$, $h_2$, and $a_T$. Here, $G_\infty$, $G_1 \sim G_N$, and $\tau_1 \sim \tau_N$ are linear viscoelastic model constants and are obtained from stress relaxation tests at a low strain level. $K_\infty$ and $K_1 \sim K_N$ were obtained using the relationship between the shear and bulk moduli in an isotropic material according to Equation (42). The Poisson's ratio ($\nu$) of 0.45 was obtained from tensile tests of the adhesive.

$$K = \frac{2(1+\nu)}{3(1-2\nu)} \qquad (42)$$

The $a_\varepsilon$, $h_0$, $h_1$, and $h_2$ are nonlinear viscoelastic parameters. Herein, we assumed that $a_\varepsilon$ and $h_1$ were equal to 1. $h_0$ and $h_2$ were obtained from stress relaxation tests at a high strain level; the procedure is explained in more detail below. $a_T$ is the temperature-dependent shift factor. Simulation at different temperatures was done using $a_T\tau_n$ instead of $\tau_n$. The shift factor was obtained from the DMA tests and is explained in detail below.

## 2.4. Experimental results

### 2.4.1. Dynamic mechanical analysis

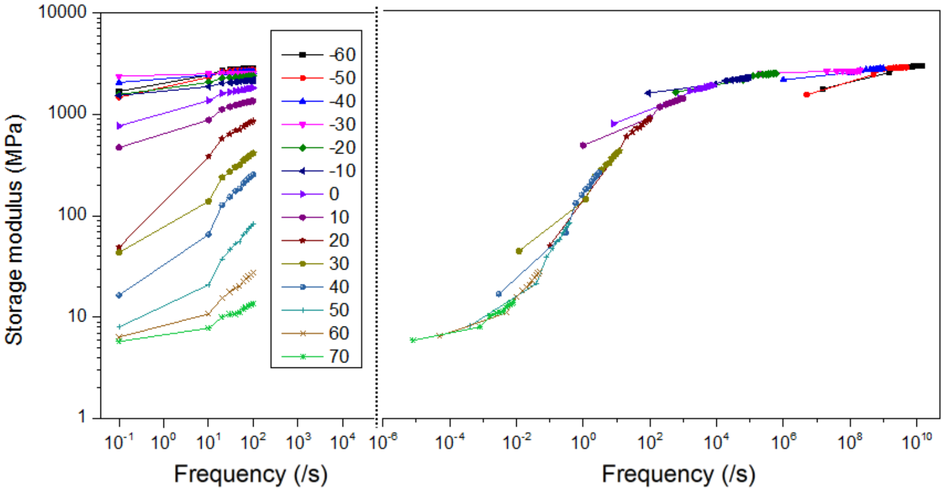

**Figure 2-2** Dynamic mechanical test results and master curve obtained using time–temperature superposition.

Dynamic mechanical tests were performed in the oscillation mode at frequencies ranging from 0.1 to 100/s. These tests were done over a wide temperature range (–60°C to 70°C) with a temperature step of 10°C. The storage modulus of the adhesive obtained from this test (see the left side of Figure 2-2) increased with increasing frequency and decreasing temperature. Time–temperature superposition of the storage modulus data provided the master curve, which showed the influence of frequency (time) and temperature on the viscoelastic properties (see the right side of Figure 2-2). The reference temperature ($T_{ref}$) was selected as 20°C. Then, the storage modulus at $T_{ref}$ and frequency $f$ can be defined as:

$$E'(T_{ref}, a_T f) = E'(T, f) \qquad (43)$$

where $a_T$ is the shift factor. The temperature dependence of the shift factor was obtained from time–temperature superposition of the storage modulus. The temperature dependence of the shift factor was fitted using a well-known empirical relationship (the WLF equation) given by Equation (44) [94]:

$$\log(a_T) = \frac{-C_1(T - T_{ref})}{C_2 + (T - T_{ref})} \qquad (44)$$

The $T_{ref}$ was chosen as 293 K. Constants $C_1$ and $C_2$ were obtained by fitting the experimental data; they were 26.316 and 283.68 K, respectively. This equation fitted the experimental results quite well at most temperatures (Figure 2-3).

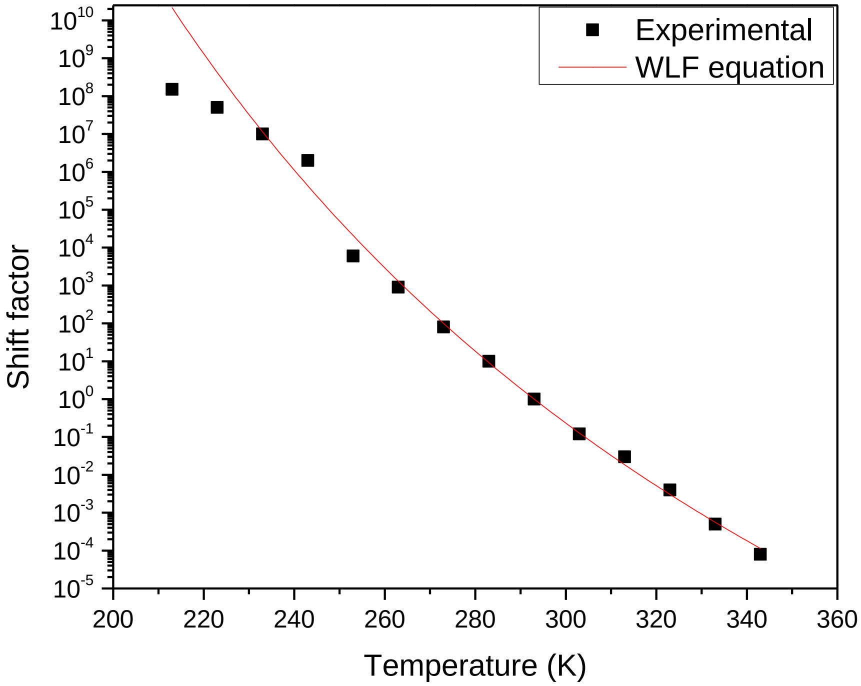

**Figure 2-3** Shift factor used in the time–temperature superposition to obtain the master curve of the storage modulus.

### 2.4.2. Stress relaxation tests

Stress relaxation tests were performed at various shear strains using lap-joint specimens. The shear strain ranged from 0.09 to 1.14. The relaxation modulus was obtained by dividing the shear stress by the shear strain (Figure 2-4). Plotting the relaxation modulus as a function of the logarithm of the shear strain clearly showed that the relaxation modulus decreased with increasing strain, due to the nonlinear viscoelastic behavior of the adhesive. The parameters for the numerical simulation were obtained as follows. First, the test result at the lowest strain level (0.091) was fitted to the Prony series (Equation (45)) to obtain the linear viscoelastic model parameters. Figure 2-5 shows the experimental results and the fitted results obtained using the Prony series equation. The linear viscoelastic model parameters are given in Table 2-1.

$$G(t) = G_{\infty} + \sum_{i=1}^{n} G_i \exp(-t/\tau_i) \qquad (45)$$

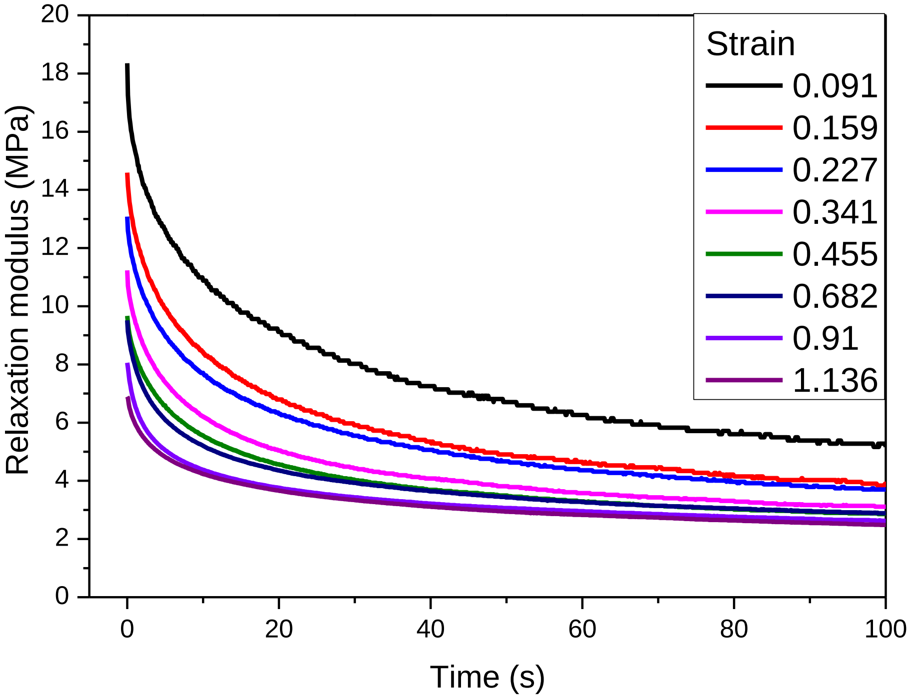

**Figure 2-4** Stress relaxation test results at different shear strains.

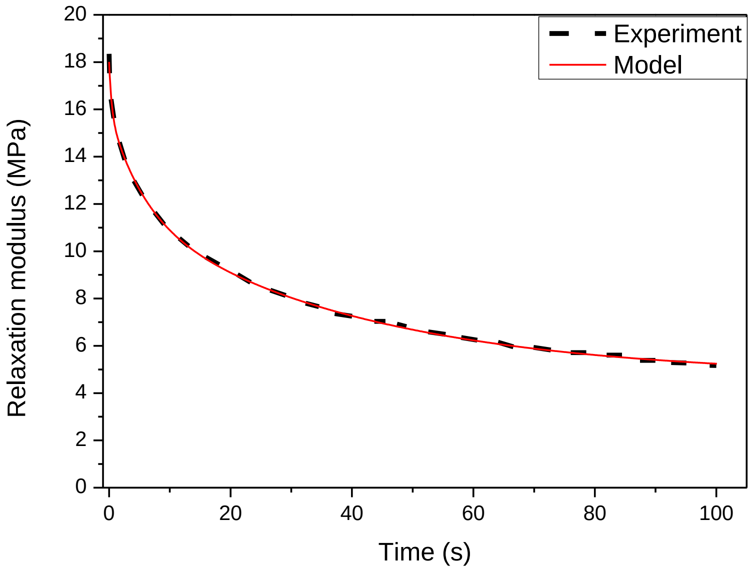

**Figure 2-5** Relaxation modulus at the shear strain of 0.091 (experimental data and fitted curve)

**Table 2-1** Constants of the linear viscoelastic model for the tested adhesive.

| Parameter | Value | Parameter | Value |
|---|---|---|---|
| $G_\infty$ | 4.695MPa | | |
| $G_1$ | 7.199MPa | $\tau_1$ | 38.83495s |
| $G_2$ | 4.006MPa | $\tau_2$ | 5.41126s |
| $G_3$ | 2.11Mpa | $\tau_3$ | 0.41841s |

Below Equation (46) is Schapery's model expressed in relaxation modulus form. By fitting Equation (46) to the stress relaxation test results at a higher strain level, the nonlinear viscoelastic parameters $h_0$, $h_1h_2$, and $a_\varepsilon$ can be obtained as follows:

$$G(t) = h_0 G_\infty + h_1 h_2 \sum_{i=1}^{n} G_i \exp(-t/(\tau_i a_\varepsilon)) \qquad (46)$$

In the case of the adhesive used in this work, the fitted $a_\varepsilon$ value changed without any clear pattern when $a_\varepsilon$ was used as a variable. Hence, $a_\varepsilon$ was set to 1. Also, $h_1$ and $h_2$ cannot be separated from a single stress relaxation test; two tests are needed to separate $h_1$ and $h_2$ from $h_1h_2$ [77]. Herein, we assumed $h_1$ to be 1 and $h_2$ was used as a variable. Figure 2-6 shows representative stress relaxation test results at different strains fitted to the nonlinear viscoelastic model (Equation (46)). The figure shows that by only changing the values of $h_0$ and $h_2$, Equation (46) can successfully express the relaxation modulus at different strains. Figure 2-7 details the values of $h_0$ and $h_2$ obtained by fitting Equation (46) to the stress relaxation test results at different strains. The parameters $h_0$ and $h_2$ are plotted against the octahedral shear strain for numerical simulation purposes. Shear strains were converted to octahedral shear strain using Equation (47) [95], as follows:

$$\varepsilon_s = \frac{2}{3}\sqrt{(\varepsilon_{11} - \varepsilon_{22}) + (\varepsilon_{11} - \varepsilon_{33}) + (\varepsilon_{22} - \varepsilon_{33}) + \frac{3}{2}({\gamma_{12}}^2 + {\gamma_{13}}^2 + {\gamma_{23}}^2)} \qquad (47)$$

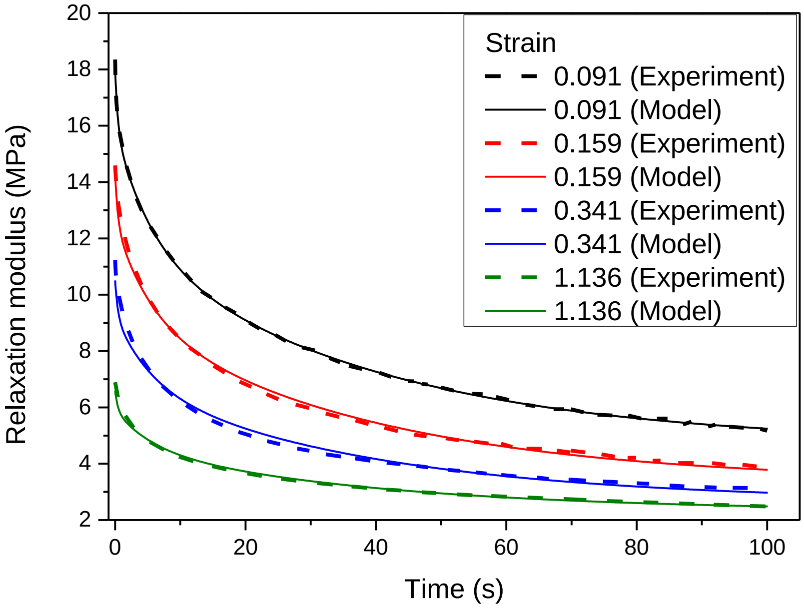

**Figure 2-6** Representative stress relaxation data and curves fitted using Equation (46).

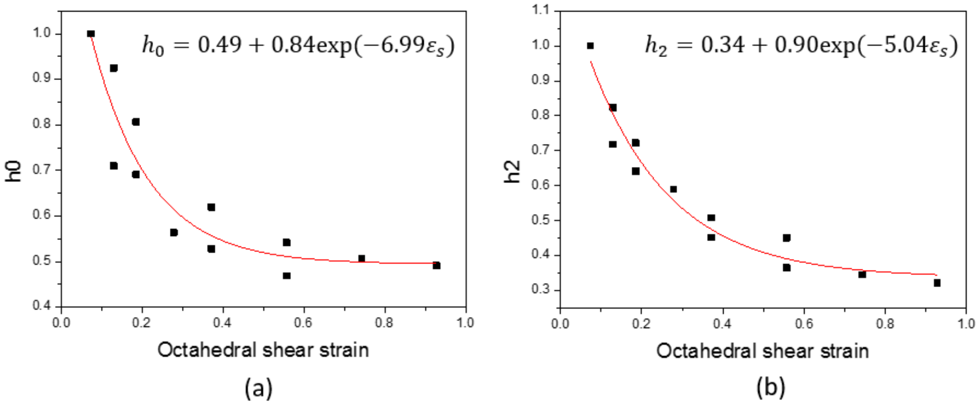

(a)

(b)

**Figure 2-7** Parameters $h_0$ and $h_2$ as a function of octahedral shear strain. The red line is the fitted curve that shows the relationships of $h_0$, $h_2$, and the octahedral shear strain.

Figure 2-7 shows the octahedral shear strain dependence of the nonlinear parameters $h_0$ and $h_2$. The octahedral shear strain dependence of the nonlinear viscoelastic parameters was expressed as an exponential function (Figure 2-7). These fitted equations were used in the numerical simulation of adhesive behavior at high strain.

### 2.4.3. Lap shear test at constant strain rate

Lap shear tests were performed at different strain rates and temperatures. Figure 2-8 shows the stress–strain curve from the test results. Figure 2-9 (a) shows the failure strength of the adhesive as a function of strain rate at different temperatures. The failure strength increased with increasing strain rate or decreasing temperature. The strain rate and temperature dependence of the failure strength can be expressed in a single master curve of failure strength, by superposing the strain rate at a certain temperature ($T$) on the reduced strain rate at a reference temperature ($T_0$). By multiplying the shift factor obtained from DMA testing to the strain rate at a certain temperature ($\dot{\varepsilon}(T)$), the reduced strain rate at the reference temperature ($\dot{\varepsilon}_{red}(T_0)$) can be defined as in Equation (40) [62, 66-68, 71]. $T_0$ in Equation (40) was set to 26°C. The plot of failure strength as a function of reduced strain rate shows that increasing temperature had the same effect as decreasing strain rate (Figure 2-9 (b)).

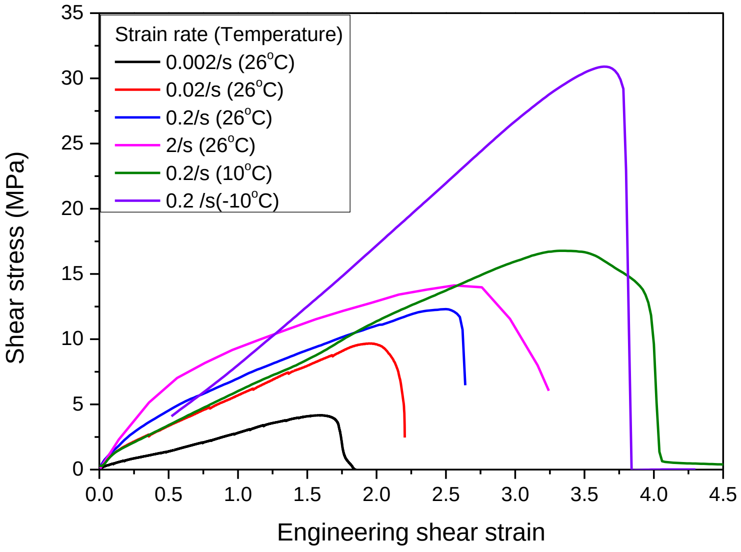

**Figure 2-8** Stress–strain curve of the lap shear test results at different strain rates and temperatures.

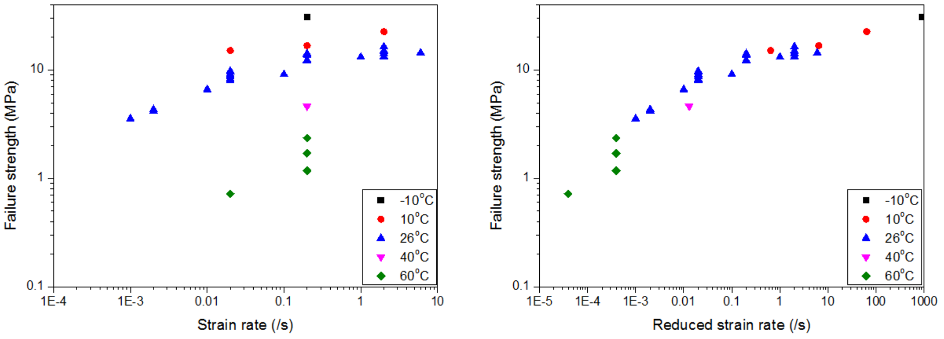

(a)

(b)

**Figure 2-9** (a) Failure strength as a function of strain rate at different temperatures. (b) Failure strength as a function of reduced strain rate.

Time-to-failure was plotted as a function of the logarithm of the strain rate (Figure 2-10). The relationship between the time-to-failure and strain rate can be expressed using the Monkman–Grant equation, as in Equation (39) [93]. This equation is widely used in the study of the creep of metals, polymers, and other materials. It can predict the time-to-failure from tensile testing of various materials including glass fiber, epoxy, and glass-reinforced epoxy composites over a large strain rate range [96-98]. Applying Equation (39) to our experimental results provided the time-to-failure as a function of strain rate (Figure 2-10). The constants $m$ and $C$ in Equation (39) were 0.9065 and 3.016, respectively. By using shift factor, strain rate at tested temperature can be converted to strain rate at reference temperature. This is defined as reduced strain rate and is shown in Equation (40). Reduced strain rate is used in Monkman-Grant equation as in Equation (41), and this allows failure strain at different temperature to be predicted. This equation was used as the failure criterion of the adhesive in the simulation.

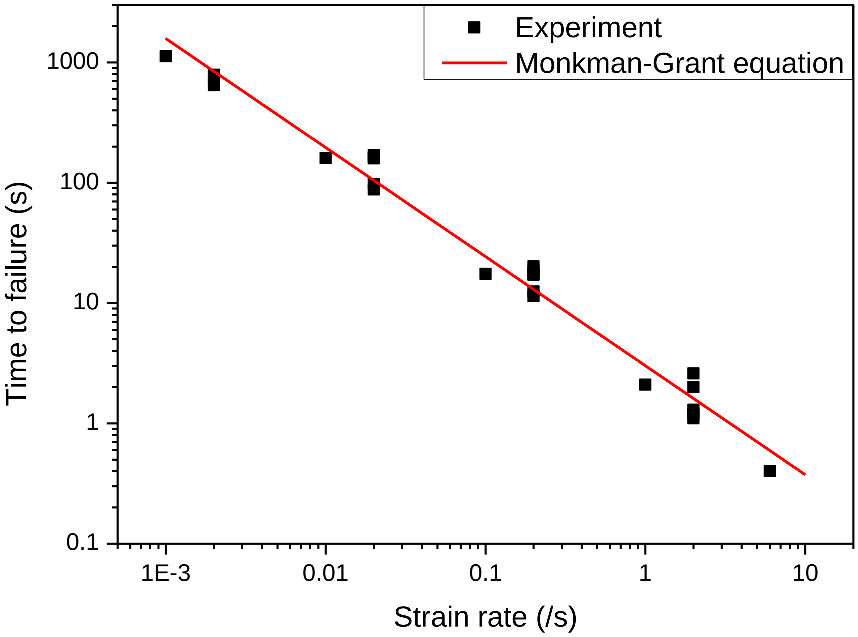

**Figure 2-10** Time-to-failure as a function of strain rate. The red line is the fitted result obtained using the Monkman–Grant equation.

## 2.5. Numerical simulation

### 2.5.1. Geometry

ABAQUS was used for the numerical simulation of the lap-joint specimen. Figure 2-11 shows the geometry of the simulated model; a planar strain element (CPE4R) was used. As shown in Figure 2-11, meshes near the adhesive joint region were formed very finely in order to get precise results. The experimentally measured length and thickness of the steel and adhesives were used in the simulation (steel adherend length: 100 mm; steel thickness: 3 mm; bonded adhesive length: 6 mm; adhesive thickness: 0.5 mm). A load was applied to the end of the steel adherend. Stress relaxation tests at room temperature and lap shear tests (at constant strain rate) at various strain rates and temperatures were simulated.

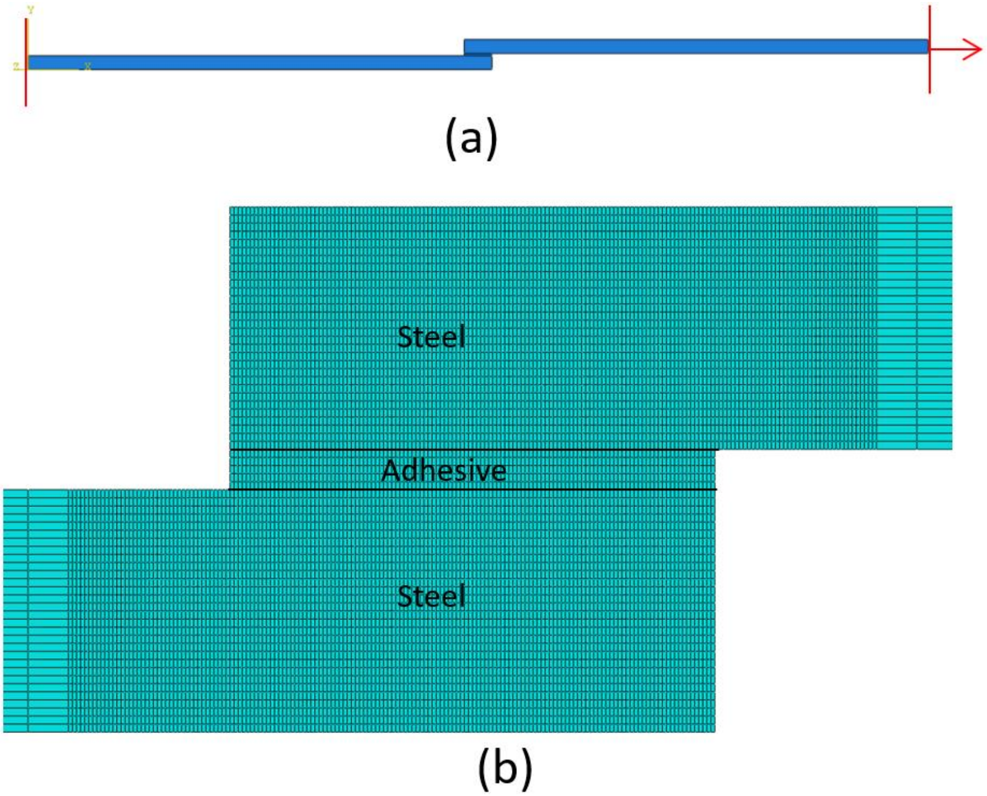

**Figure 2-11** Geometry of the simulated model. (a) Two-dimensional modelled lap-joint specimen. (b) Mesh near an adhesive joint.

### 2.5.2. Simulation results (stress relaxation test)

The simulation results were obtained using both linear and nonlinear viscoelastic models. Figure 2-12 shows the normal and shear stress distributions during stress relaxation testing of the lap-joint specimens at the engineering shear strain of 0.1. Figure 2-12 (a) and (b) show the shear stress distribution immediately and 30 s after deformation, respectively. The uniform distribution of the shear stress across the adhesive is attributed to the very high modulus of the adherend compared to the adhesive [99]. It also shows that shear stress relaxation occurred almost uniformly across the adhesive joints. Figure 2-12 (c) and (d) shows the normal stress distribution of the adhesive joint immediately and 30 s after deformation, respectively. Normal stresses were concentrated at the edges of the adhesives. Deformation of the adherend caused rotation of the steel in the lap joint. Such rotation led to peel stress at the edge of the overlap [99]. Figure 2-12 (c) and (d) shows that the normal stress at the edge of the overlap also relaxed during the stress relaxation test. These results demonstrate that the viscoelastic behavior of the adhesive in the lap-joint specimen was well-implemented into the numerical simulation.

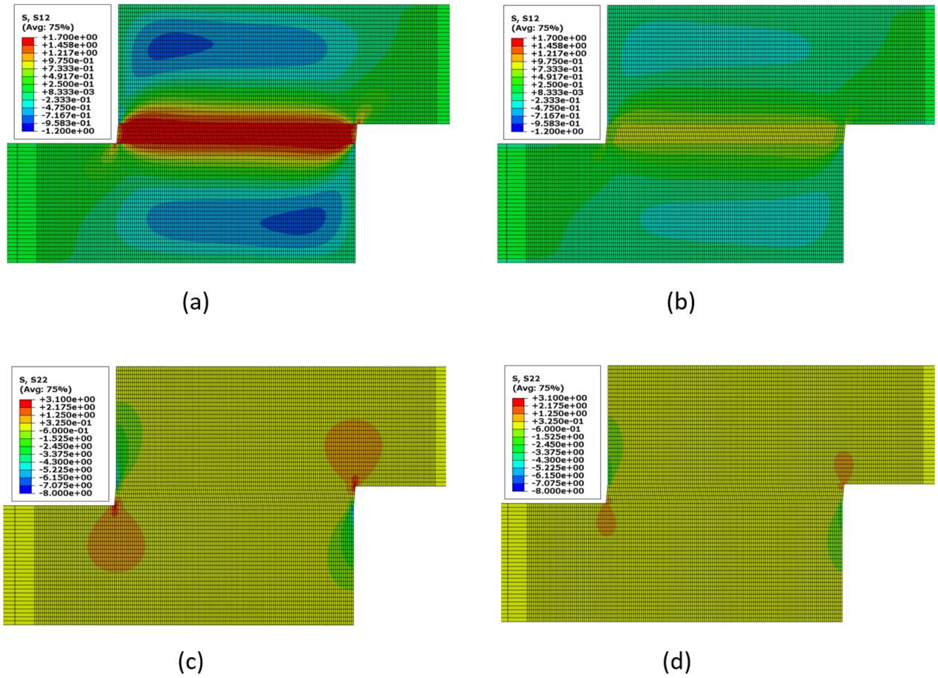

**Figure 2-12** Distributions of the shear and normal stresses obtained from the

simulations. (a) Shear stress immediately after deformation. (b) Shear stress after 30 s of stress relaxation. (c) Normal stress immediately after deformation. (d) Normal stress after 30 s of stress relaxation.

Figure 2-13 compares the experimental and simulation stress relaxation results for the lap-joint specimens. The shear stress was calculated by dividing the force at the end of steel by the adhesion area. The shear strain used here is the engineering shear strain which was calculated by dividing the displacement of the steel by the thickness of the adhesive. At low strain level, the simulation results using the linear viscoelastic and nonlinear viscoelastic models were very similar, and were in good agreement with the experimental data. However, at higher strains, there was a discrepancy between the simulation results obtained using the linear viscoelastic model and the experimental results; the nonlinear viscoelastic model was superior. These results indicate that the nonlinear viscoelastic model was well-implemented into the numerical simulations and, more importantly, was appropriate for adhesives at high strains.

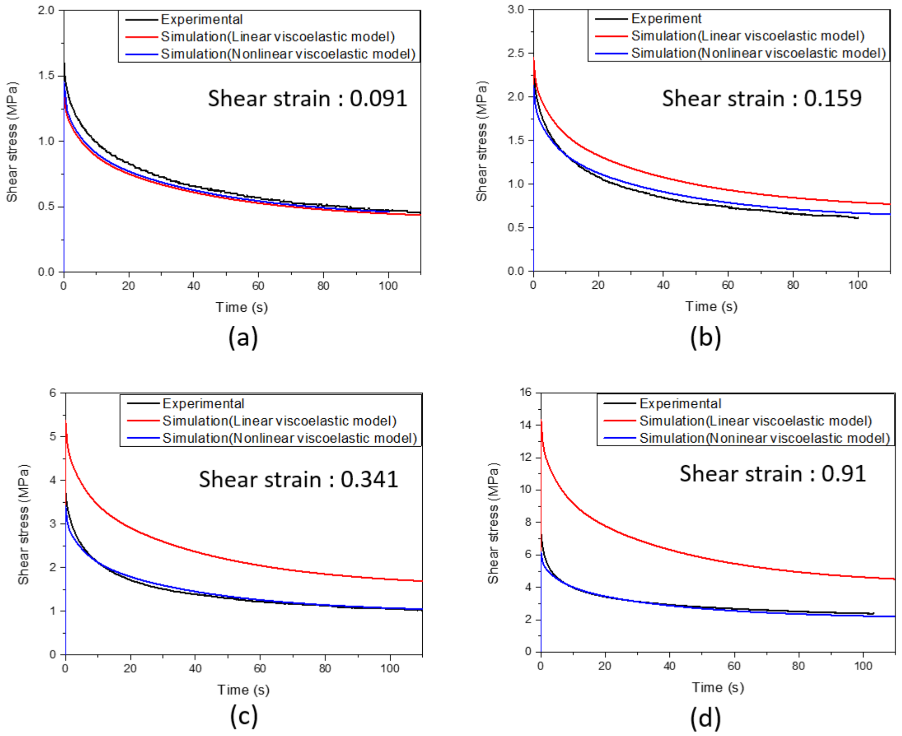

**Figure 2-13** Comparison of the experimental and simulation stress relaxation results of lap-joint specimens at various strains.

### 2.5.2. Simulation results (lap shear test until failure)

Adhesive behavior of lap-joint specimen was simulated until failure occurred to investigate if the simulation results at very high strain are reasonable as in other researches [79-82]. Figure 2-14 shows the stress and strain distribution obtained from simulation results of lap shear test with strain rate of 0.2/s at 10°C. The shear strain in Figure 2-14 is 3.74, which was the shear strain right before failure occurred. Critically distorted mesh was not found in the results even at high shear strain. It is shown that the shear stress is well distributed in the adhesive and the normal stress is concentrated at the edge of the adhesive joint. The stress concentration in this type of simulation was also reported in other researches [100, 101]. Deflections of the adherend and the overlap, and the joint edge moment at the end of the overlap are important factors that affect the development of stress distribution in the adhesive layer [102, 103]. As the modulus of the adhesive becomes smaller, peak stress at the edge of the adhesive joint becomes smaller [100, 104]. The instantaneous modulus of adhesive and the modulus of steel used in our work are 52MPa and 180GPa respectively. Since the modulus of the adhesive is very small compared to the adherend, the shear stress is distributed nearly uniformly in the adhesive joint while small normal stress peak is still observed at the edge as in Figure 2-14 [100, 104, 105].

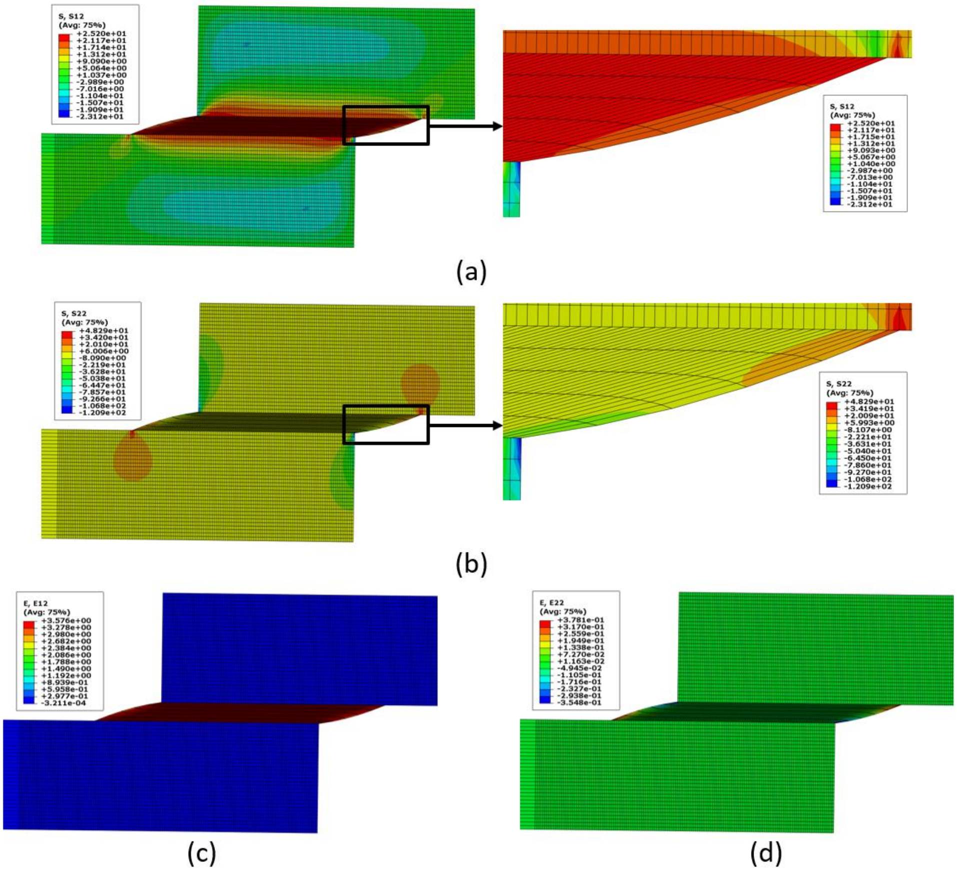

**Figure 2-14** Distributions of the stresses and strain near adhesive joint at shear strain of 3.74. Strain rate of 0.2/s at 10°C was the simulation condition. (a) Shear stress (b) Normal stress (c) Shear strain (d) Normal strain

Adhesive behavior in the lap-joint specimen at different strain rates and temperatures was also simulated. Figure 2-15 compares the experimental and simulation results of the constant strain rate tests of lap-joint specimens at different strain rates and temperatures. The shear stress is plotted against the engineering shear strain in Figure 2-15. It is evident that the linear viscoelastic model described the adhesive behavior only at small strains, while the nonlinear viscoelastic model simulated the adhesive behavior until failure. It is also evident that the adhesive behavior at different rates and temperatures was well-simulated using the nonlinear viscoelastic model.

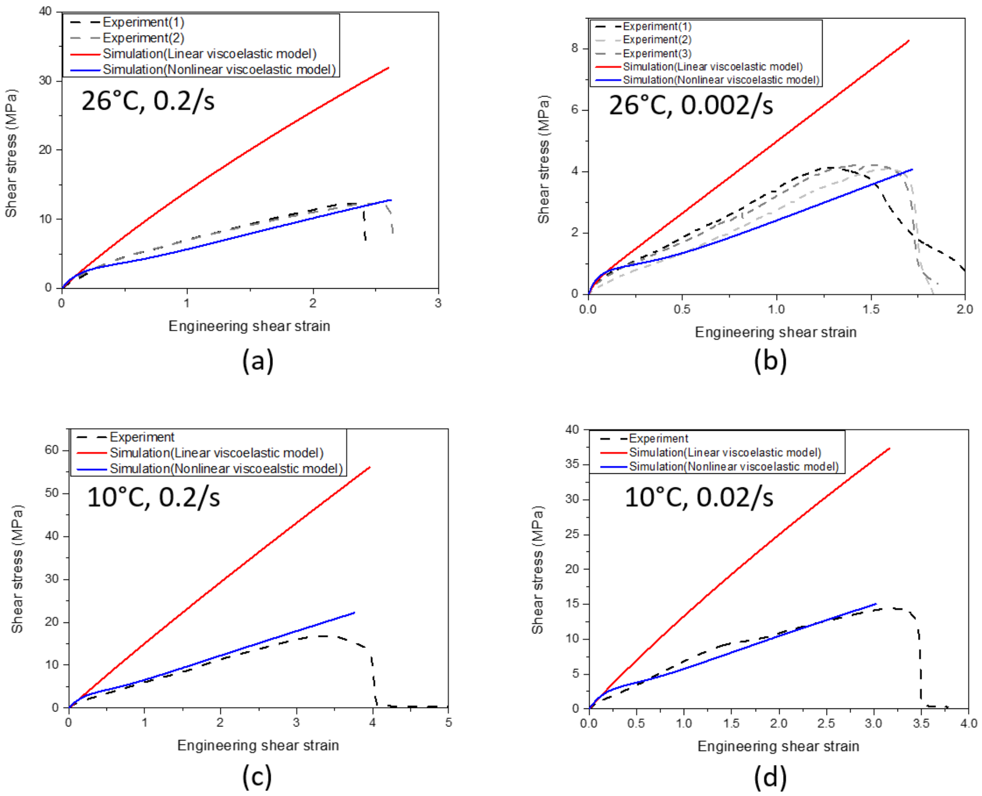

**Figure 2-15** Simulation and experimental results of lap-shear testing at different strain rates and temperatures.

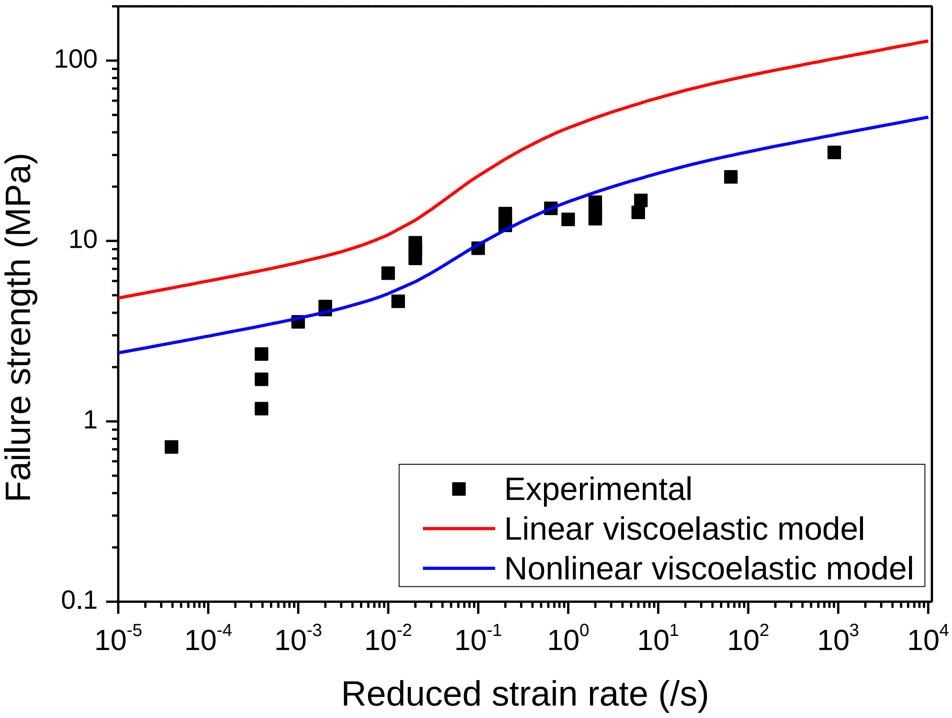

**Figure 2-16** Relationship between failure strength and strain rate. Simulation and experimental results are compared.

The failure strength of the adhesive was obtained from the simulation which used the relationship between the failure strain and reduced strain rate as failure criterion (Equation (41)). Figure 2-16 compares the experimental and simulation results. The failure strength calculated using the linear viscoelastic model was much higher than the experimental value at every strain rate. In contrast, the failure strengths predicted by the nonlinear viscoelastic model were similar to the experimental data at most strain rates. This finding again confirms that the nonlinear viscoelastic model should be used to simulate the mechanical behavior of adhesives at large strains. The simulation approach using nonlinear viscoelastic model and reduced strain dependent failure criterion is expected to be used in many areas. Material behavior until its failure at strain rate and temperature which are difficult to perform experiments can be calculated using this approach.

### 2.5.2. Hyperelastic model combined with Prony series

The nonlinear viscoelastic model can also be implemented by using hyperelasticity combined with Prony series. To compare it with Schapery's model, we carried out a numerical simulation using hyperelastic model combined with Prony series. ABAUS built-in model, Reduced Polynomial hyperelastic model and viscoelastic model (Prony series), was used. For Reduced Polynomial model, a strain energy potential order of 6, which is maximum in the model, was used. Constants $G_\infty$, $G_1 \sim G_n$, $\tau_1 \sim \tau_n$ in Prony series were obtained in the same way as in section 4.2.

To get the hyperelastic model parameters, relaxation data at different strain were fitted to equation as follows:

$$G(t) = h\left( G_\infty + \sum_{i=1}^{n} G_i \exp(-t/\tau_i) \right) \qquad (48)$$

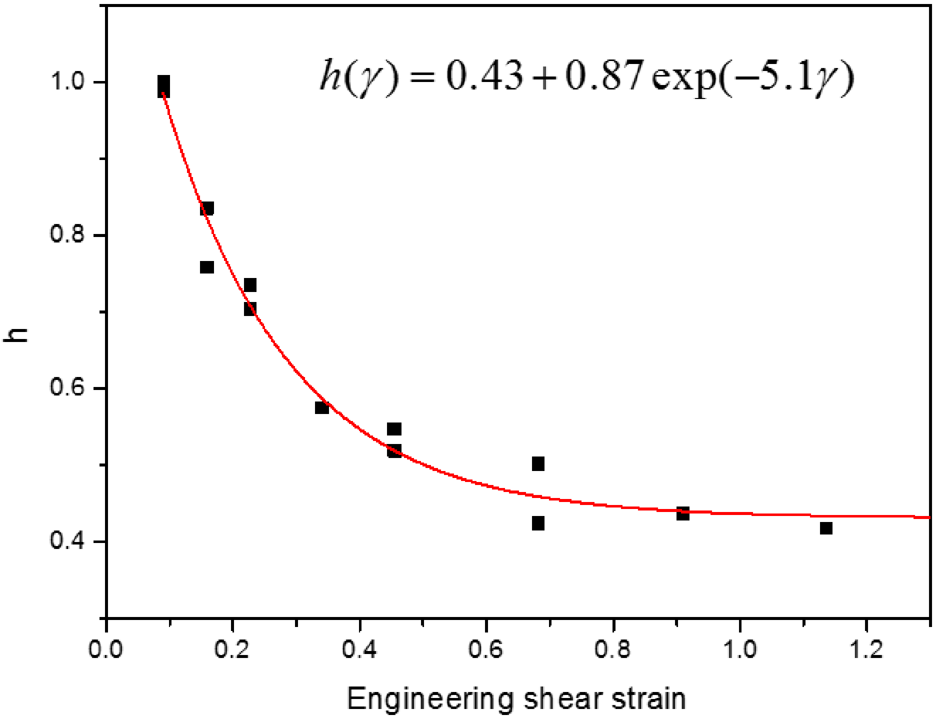

**Figure 2-17** Parameters $h$ as a function of shear strain. The red line is the fitted curve that shows the relationships of $h$ and the shear strain.

Using Equation (48), we were able to get shear strain dependent $h$ values. Figure 2-17 details the values of $h$ obtained by fitting Equation (48) to the stress relaxation test results at different strains. Instantaneous shear modulus which is sum of $G_\infty$, $G_1 \sim G_n$ is 18.01MPa. The shear stress-shear strain curve of hyperelastic part can be obtained by multiplying instantaneous modulus $G_0$ by shear strain dependent parameter $h$ and shear strain $\gamma$ as in Equation (49)

$$\tau = h(\gamma) G_0 \gamma \qquad (49)$$

The shear stress-shear strain curve of instantaneous hyperelastic part is shown in Figure 2-18. Equation (50) is the strain energy density function of Reduced Polynomial hyperelastic model [106].

$$W=\sum_{i=1}^{N}C_{i0}(I_1-3)^i+\sum_{i=1}^{N}D_i(J-1)^{2i} \qquad (50)$$

Where $I_1$ and $I_2$ are the first and second invariant of left Cauchy green deformation tensor and $J$ is determinant of deformation gradient. Shear stress component can be expressed as Equation (51) [107].

$$\tau=2\gamma\left(\frac{\partial W}{\partial I_1}+\frac{\partial W}{\partial I_2}\right) \qquad (51)$$

Using Equation (50) and (51), the shear stress can be expressed with shear strain as in Equation (52).

$$\tau=2\sum_{i=1}^{N}iC_{i0}\gamma^{2i-1} \qquad (52)$$

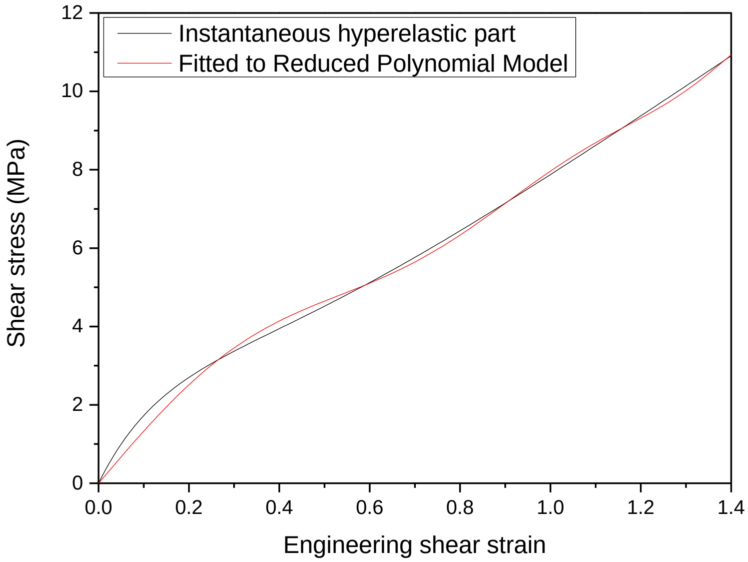

**Figure 2-18** Shear stress-shear strain curve of instantaneous hyperelastic part. The red line is the fitted curve of Equation (52).

We were able to obtain constants $C_{10} \sim C_{N0}$ by fitting Equation (52) to the shear stress-shear strain curve of hyperelastic part of the adhesive. The fitted result of Equation (52) is shown in Figure 2-18 in red line. $D_1$ was obtained using its relationship with instantaneous bulk modulus as in Equation (53) [108]. Since instantaneous bulk modulus $K_0$ is 174.1Mpa, $D_1$ value was calculated as 0.0115.

$$K_0 = \frac{2}{D_1} \qquad (53)$$

$D_2 \sim D_6$ were arbitrarily set to 0.0001 since these constants are only obtainable from volumetric test. By using hyperelastic model combined with Prony series, simulation of nonlinear viscoelastic model was possible. Figure 2-19 shows experimental and simulation results of stress relaxation test at 0.91 strain. It is shown that Schapery's model is more accurate than hyperelastic model combined with Prony series.

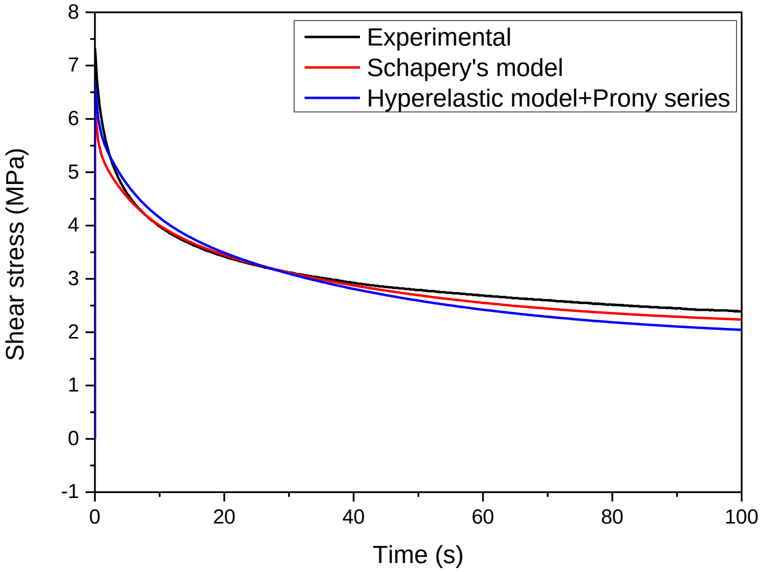

**Figure 2-19** Experimental and simulation results of stress relaxation test at 0.091 strain. Comparison of simulation results using Schapery's model and hyperelastic model combined with Prony series is shown.

Schapery's model uses $h_0$, $h_1$, $h_2$ and $a_\varepsilon$ to accurately show the nonlinear viscoelastic behavior. It can accurately distinguish the changes in long term modulus and transient component of the relaxation modulus. However, hyperelastic model combined with Prony series uses only one parameter to show nonlinear viscoelastic behavior. It assumes that instantaneous modulus is the only thing that change as strain increases. If strain dependency of $E_\infty$ and $E_i$ are the same, then hyperelastic model combined with Prony series will show the same behavior as the Schapery's model. But if the material's strain dependency of $E_\infty$ and $E_i$ has large difference, then hyperelastic model combined with Prony series wouldn't be enough to accurately show the material's nonlinear viscoelastic behavior.

## 2.6. Summary

A nonlinear viscoelastic model was used to describe the mechanical behavior of adhesives. Schapery's model was chosen as the nonlinear viscoelastic model. A procedure for implementing Schapery's model with strain-dependent parameters into a numerical simulation was derived and described in detail. Reduced strain rate dependent failure criterion was used so that failure strain at different strain rate and temperature can be calculated. Implementation in the ABAQUS finite-element software was done via a UMAT subroutine. Dynamic mechanical testing of bulk adhesive specimens and stress relaxation testing of lap-joint specimens were used to validate the mathematical derivations, implementation, and viscoelastic properties of a polyurethane-based adhesive. The thermomechanical deformation behavior of the adhesive was then simulated. Comparison of the simulation and experimental results showed that the nonlinear viscoelastic model was well-implemented into the finite-element software. The simulation results of lap shear testing at different strain rates and temperatures were in good agreement with the experimental data at every strain level. The results also demonstrated that the mechanical properties of the adhesive at very high strain rates, which are experimentally unobtainable, can be predicted with confidence using a nonlinear viscoelastic model.

# Chapter 3. CNT/graphene hybrids

## 3.1. Introduction

Carbon nanotubes (CNTs) and graphene have been intensively studied for various applications[2-4, 109, 110] including supercapacitors,[22, 111, 112] field-emission devices,[23, 113] and sensor devices[24] because of their excellent mechanical, thermal, electrical, and optical properties. Thin films are the most versatile form for such applications, so various processing methods have been developed to fabricate thin films from graphene and CNT solutions, including filtration,[14, 114] dip coating, electrophoretic deposition,[15] and inkjet printing.[16, 115, 116] These solution-based processing methods are advantageous for large-scale and low-cost manufacturing, but have some serious drawbacks. For example, graphene films made from solutions have lower electrical conductivities than the theoretical value, presumably because of poor interlayer junction resistance.[117] To overcome this problem, CNT/graphene hybrids have been suggested because the CNTs could then form conductive paths between the graphene flakes.[26, 118]

CNT/graphene hybrids have been studied in many researches due to its enhanced properties than that of graphene and CNT itself. In some work, it was found that the thermal conductivity increases by hybridizing CNT/graphene.[27] In that work, they claimed that the enhancement of thermal conductivity in CNT/graphene hybrid is due to bridging of graphene flakes by CNTs. Most of the works related to CNT/graphene hybrids is about its electrical conductivity. In case of CNT/graphene hybrids in a film form, the CNT/graphene hybrid films have higher electrical conductivities than pure graphene films.[14, 30, 33, 119-124] Additionally, in some researches, it was found that the CNT/graphene films with graphene and CNTs mixed and dispersed in the same layer have much higher electrical conductivities than graphene films coated with CNTs.[120] The improvement in the electrical conductivity by hybridization is also found in the CNT/graphene hybrids in fiber form.[29, 125] The proposed mechanism for this improvement is that the CNTs are acting as conducting bridges between the graphene flakes.[30, 125-128] CNT/graphene hybrids also have higher electrical conductivities than pure CNT films.[33, 120, 121, 123, 124] King *et al.* suggested that the synergism of the conductivities is derived from the graphene particles filling the space between the CNTs and thereby providing a lower junction resistance between the graphene and the CNTs. These two explanations for the synergistically improved electrical conductivity of CNT/graphene hybrids, i.e., CNTs acting as conducting bridges between the graphene flakes and graphene particles filling the space between CNTs, have the common feature of an increased number of contacts between the graphene particles and the CNTs. This study aimed to establish theoretical and experimental explanations for the synergistic effect. CNT/graphene hybrids prepared by simple dispersion and a film processing method were used in the experimental work.

Various processing methods have been developed to make CNT/graphene hybrid films. Vacuum filtration was the first solution approach.[33, 126] Spin coating and solution casting have been used more recently.[14, 26, 129] Sequential self-assembly of graphene and CNT on a substrate have also been reported.[130] The alternative solid-phase composition method, i.e., attaching a solid graphene film to a solid CNT film,[118] has been used in various applications such as transparent electrodes, field effect transistors, and supercapacitors.[120, 130] Recently, inkjet printing has been employed as a film processing method because of its simplicity and ability to make complex patterns; this approach has been used in applications such as memory devices, solar cells, organic thin film transistors, and light emitting diodes.[131] Inkjet printing was used in this study to prepare CNT/graphene hybrids from separate solutions, i.e., inks. It is important to avoid agglomeration of the particles in their respective solutions. Ball-milling, ultrasonication, or surfactant treatment[16, 116, 132, 133] have been previously used to prepare agglomeration-free graphene and CNT inks. However, in this study, a simple wrapping technique was used to prepare stable CNT/graphene hybrid inks.[134]

This paper presents a predictive model for quantitatively explaining the synergistic behavior of CNT/graphene hybrids. A quantitative analysis carried out using the model demonstrated that the hybrids can exhibit higher electrical conductivities than pure CNT or graphene films at certain composition ratios. CNT/graphene hybrids prepared by inkjet printing were used to validate the predictive model.

## 3.2. Experiment

### 3.2.1. Materials and ink formulation

Graphene particles (XG Sciences, Grade C750), multi-walled carbon nanotubes (MWCNT, Hanwha Nanotech, CM-95), poly(acrylonitrile) (PAN, Polysciences, homopolymer, MW 200000), and N,N-dimethylformamide (DMF, Daejung Chemical, EP grade, 99.5%) were used to prepare CNT and graphene hybrid inks using the following process. First, PAN solutions were prepared at 0.25, 0.5, 1, and 2 wt% concentrations in DMF (70 g). The solutions were stirred on a hot plate at 90°*C*. Graphene (0.7 g) was then added to each PAN solution. The graphene solutions were stirred and then ultrasonicated. Then, the solutions were centrifuged at 5000 rpm for 15 min and the supernatant was vacuum-filtered through filter paper having a pore size of 1.2 μm (GF3-grade glass microfiber filter, Whatman). CNT and graphene inks were prepared in the same manner. The separate graphene and CNT inks were then mixed together in various proportions to make different CNT/graphene hybrid inks.

### 3.2.2. Characterization and Inkjet Printing

The viscosity of each solution was measured using a rheometer (AR–G2, TA Instruments) at shear rates of 4.642, 10, 21.55, 46.42, 100, 215.5, and 464.2 $s^{-1}$ at 25°*C to adjust the printing parameters.* The average size of the particles in an ink was measured using a dynamic light scattering spectrophotometer (DLS–7000, Otsuka Electronics). The zeta potential was also measured using an electrophoretic light scattering spectrophotometer (ELS–8000, Otsuka Electronics) to evaluate the degree of dispersion of the particles. TGA was carried out to calculate the amount of graphene, CNT, and PAN in the inks.

An inkjet printer (Dimatix DMP–2800, Fujifilm) was used to print the prepared inks on a substrate. The droplet formation of the inks was controlled by changing the cartridge settings, including the jetting voltage, waveform, meniscus control, and temperature. Photo paper was selected as the substrate. The inks were printed in a square pattern 7 × 7 $mm^2$ with a drop spacing of 25 μm, varying the number of printings from 1–25. Details of the inkjet printer and printing conditions are shown in Figure 3-1. The thicknesses and morphologies of the printed inks were investigated using AFM and SEM, respectively. The electrical properties of the printed inks were measured using the four-point probe method.

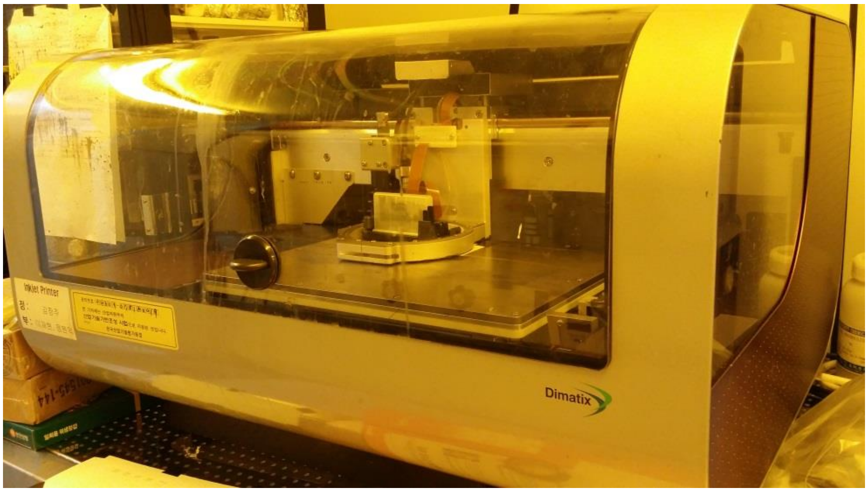

(a)

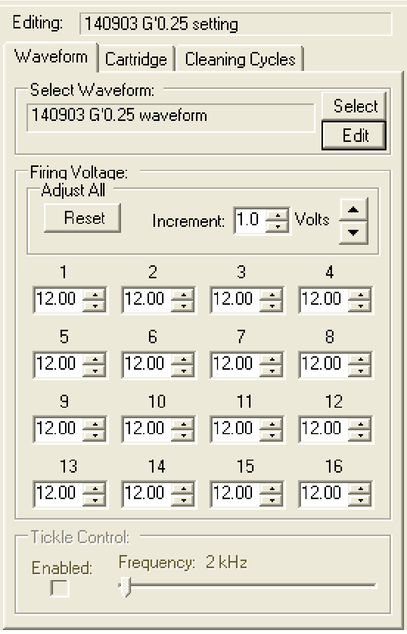

Editing: 140903 G'0.25 setting

Select Waveform: 140903 G'0.25 waveform

Firing Voltage:

Adjust All

Increment: 1.0 Volts

| 1 | 2 | 3 | 4 |
|---|---|---|---|
| 12.00 | 12.00 | 12.00 | 12.00 |
| **5** | **6** | **7** | **8** |
| 12.00 | 12.00 | 12.00 | 12.00 |
| **9** | **10** | **11** | **12** |
| 12.00 | 12.00 | 12.00 | 12.00 |
| **13** | **14** | **15** | **16** |
| 12.00 | 12.00 | 12.00 | 12.00 |

Tickle Control:

Enabled: ☐

Frequency: 2 kHz

(b)

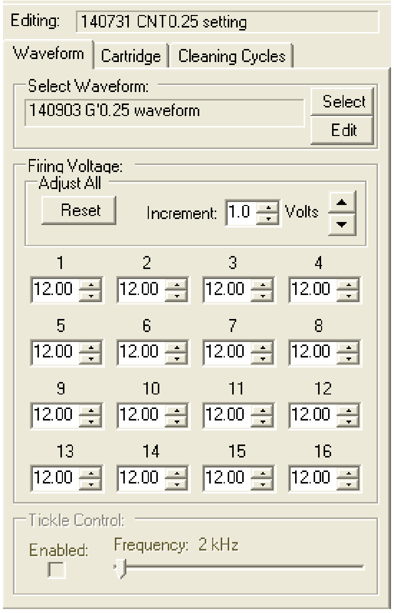

Editing: 140731 CNT0.25 setting

Select Waveform: 140903 G'0.25 waveform

Firing Voltage:

Adjust All

Increment: 1.0 Volts

| 1 | 2 | 3 | 4 |
|---|---|---|---|
| 12.00 | 12.00 | 12.00 | 12.00 |
| **5** | **6** | **7** | **8** |
| 12.00 | 12.00 | 12.00 | 12.00 |
| **9** | **10** | **11** | **12** |
| 12.00 | 12.00 | 12.00 | 12.00 |
| **13** | **14** | **15** | **16** |
| 12.00 | 12.00 | 12.00 | 12.00 |

Tickle Control:

Enabled: ☐

Frequency: 2 kHz

(c)

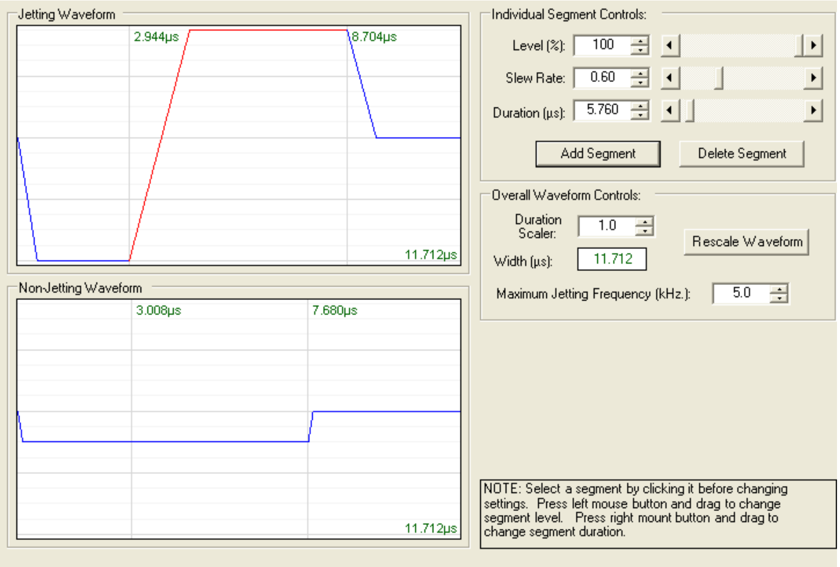

Individual Segment Controls:

Level (%): 100

Slew Rate: 0.60

Duration (µs): 5.760

Overall Waveform Controls:

Duration Scaler: 1.0

Width (µs): 11.712

Maximum Jetting Frequency (kHz.): 5.0

NOTE: Select a segment by clicking it before changing settings. Press left mouse button and drag to change segment level. Press right mount button and drag to change segment duration.

(d)

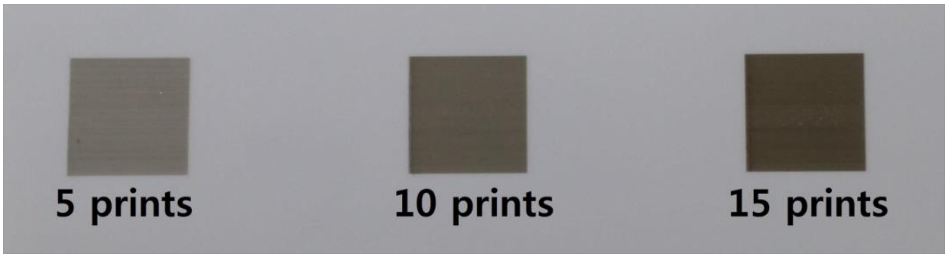

(e)

**Figure 3-1** (a) The inkjet printer used in this study (Dimatix DMP–2800, Fujifilm). Jetting voltage conditions of the (b) graphene ink and the (c) CNT ink, and (d) waveform setting conditions. (e) The inks were printed on the photopaper in a square pattern of 7 mm × 7 mm$^2$.

## 3.3. Predictive model for electrical conductivity of CNT/graphene hybrids

### 3.3.1. Relationship between conductivity and the number of contacts

A predictive model was developed to explain the synergistic behavior of graphene and CNT electrical conductivities in CNT/graphene hybrids. The conductivity of these hybrids is governed by inter-particle contacts. A random stick network model can be used to estimate the electrical conductivity of a CNT film.[135] This model assumes that a CNT behaves as a conductive stick and that an assembly of many conductive sticks (e.g., a film) is randomly distributed in two dimensions. The electrical conductivity of a CNT film can then be determined according to Equation (54):

$$\sigma \sim \frac{1}{\frac{b}{n_s G_s} + \frac{1}{n_j G_j}} \tag{54}$$

where $n_s$ is the number of conductive sticks and $n_j$ is the number of their junctions, i.e., the number of stick-to-stick contacts. Here, $b$ is a constant, $G_s$ is the stick conductance, and $G_j$ is the junction conductance. Because the conductivities of individual CNTs and graphene are much higher than the conductivity of their junctions (contacts),[51, 136] Equation (54) can be simplified to $\sigma \sim n_j G_j$ for CNT/graphene hybrids. On this basis, the electrical conductivity of CNT/graphene hybrids is proportional to the number of CNT-to-CNT, graphene-to-graphene, and graphene-to-CNT contacts. Furthermore, because the conductivity of a hybrid increases with increasing numbers of contacts made by the individual elements in the hybrid, the conductivity of the hybrid is maximized when the number of contacts is maximized. Consequently, the conductivity of CNT/graphene hybrids can be estimated by calculating all of the contacts made by the graphene and the CNTs.

### 3.3.2. Estimating the number of contacts

#### 3.3.2.1. Estimating the number of CNT-CNT contacts

Many studies have focused on predicting the mechanical properties of short-fiber assemblies. Calculation of the number of fiber-to-fiber contacts is very important because external loads are transferred between the short fibers through their contacts. Komori *et al.* defined the orientation of fibers in space using two angles (Figure 3-2) and developed a model to calculate the number of fiber-to-fiber contacts.[137] The fibers are assumed to have straight cylindrical geometries. Their approach was used here to calculate the number of CNT-to-CNT contacts by simply replacing fibers with CNTs in the model. The numbers of CNT-to-graphene and graphene-to-graphene contacts were also calculated by modifying the model.

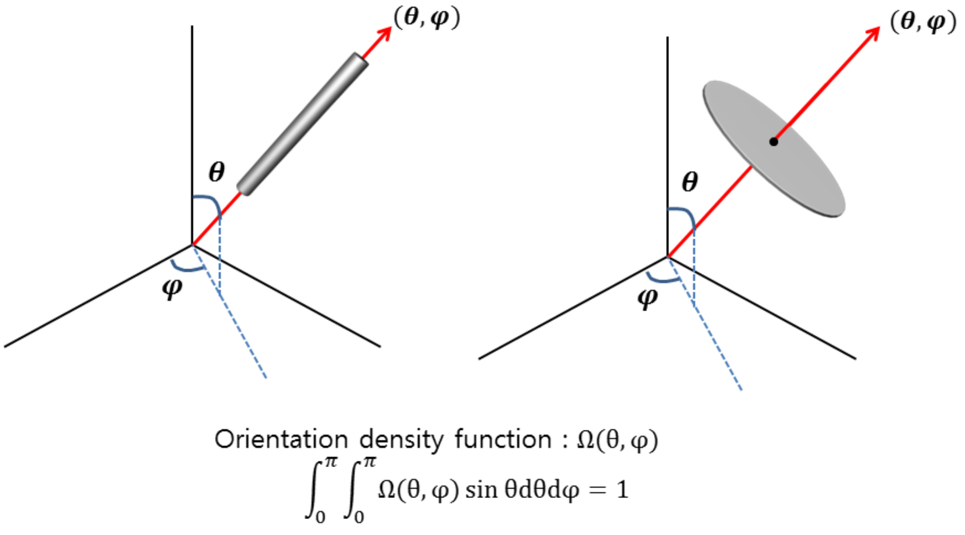

**Figure 3-2** Orientation density function describing the orientation of individual CNT and graphene particles in space

The orientation of a fiber can be expressed by two angles, i.e., a pair $(\theta, \varphi)$ where $0 \leq \theta \leq \pi$, $0 \leq \varphi \leq \pi$ represents an angle between the *z*-axis and the axis of the fiber and between the *x*-axis and the normal projection of the fiber axis onto the *xy* plane (Figure 3-2). The probability of finding the orientation of a fiber in the infinitesimal range of angles $\theta \sim \theta + d\theta$ and $\varphi \sim \varphi + d\varphi$ is $\Omega(\theta, \varphi)\sin\theta d\theta d\varphi$, where $\Omega(\theta, \varphi)$ is the orientation density function. The following condition must be satisfied for the probability density function:

$$\int_0^p\int_0^p W(q,j)\sin q dq dj = 1 \qquad (55)$$

For the random orientation case, Ω becomes a constant (1/2π). We consider two

CNTs, (*A*) and (*B*) having CNT orientations of $(q,j)$ and $(q¢,j¢)$, respectively, in arbitrary positions in a volume $V$. CNT *B* will contact CNT *A* when the center of mass of CNT *B* enters into the region shown in Figure 3-3. If the diameter and length of the CNT are $D$ and $\lambda$, respectively, then the volume of this region ($v_C$) becomes:

$$v_C(q,j;q¢,j¢) = 2Dl^2 \sin c_c \qquad (56)$$

where $\chi_C$ is the angle between the two CNTs.

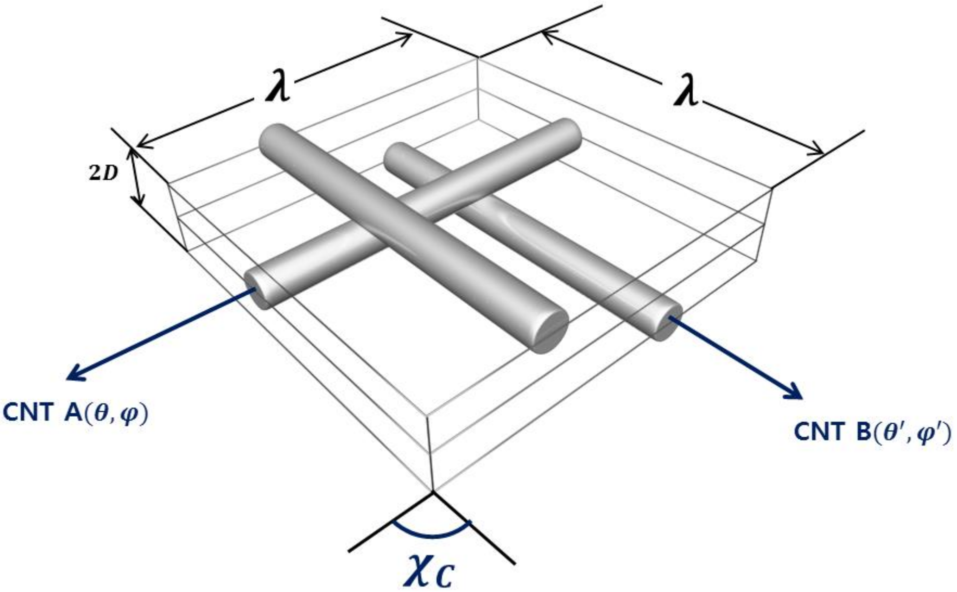

**Figure 3-3** The parallelepiped formed by a CNT *B* $(\theta', \varphi')$ moving around a fixed CNT *A* $(\theta, \varphi)$ while maintaining contact.[137]

The probability that CNT *B* contacts CNT *A* is then given by:

$$p_C(\theta,\varphi;\theta'\varphi') = \frac{v_C}{V} = \frac{2D\lambda^2}{V}\sin\chi_c \tag{57}$$

If there are $N_c$ CNTs in the volume $V$, the average number of CNTs that come into contact with CNT $A$ is calculated as:

$$n_C(\theta,\varphi) = \int_0^{\pi}\int_0^{\pi} p_C(\theta,\varphi;\theta',\varphi')(N_c - 1)\Omega(\theta',\varphi')\sin\theta' d\theta' d\varphi' \tag{58}$$

For large $N_c$ ($N_c >> 1$):

$$n_C(\theta,\varphi) = \frac{2D\lambda^2 N_c}{V} J(\theta,\varphi) \tag{59}$$

where:

$$J(\theta,\varphi) = \int_0^{\pi}\int_0^{\pi} \Omega(\theta',\varphi')\sin\chi_c \sin\theta' d\theta' d\varphi' \tag{60}$$

The average number of contacts $\overline{n_C}$ on an arbitrary CNT having a random orientation is:

$$\overline{n_C} = n(0,0) = \frac{2D\lambda^2 N_C}{V} J(0,0) = \frac{\pi D\lambda^2 N_C}{2V} \tag{61}$$

The total number of the contacts in a CNT assembly of volume $V$ containing $N_c$ CNTs in a random orientation is obtained by multiplying $\frac{N_C}{2}$ by $\overline{n_C}$. The factor 1/2 avoids double- counting of the contacts. Finally, the following equation can be obtained to calculate the number of CNT-to-CNT contacts:

$$\overline{n_{Ctot}} = \frac{\pi D l^{2} N_{C}^{2}}{4V} \tag{62}$$

Equation (62) can be directly used to calculate the number of CNT-to-CNT contacts, assuming CNTs are straight cylinders with a constant length and diameter.

#### 3.3.2.2. Estimating the number of graphene-graphene contacts

The Komori model is modified to accommodate different geometrical entities, i.e., CNT-to-graphene and graphene-to-graphene contacts.

To estimate the number of graphene-to-graphene contacts, we considered graphene to be a disk with a radius of $r$ and negligible thickness. We oriented a graphene particle *A* with its normal vector having an orientation of $(\theta, \varphi)$ placed in an arbitrary position in volume *V*. Similar to the CNT-to-CNT contact case, another graphene particle *B* with orientation $(\theta', \varphi')$ was considered to contact graphene *A* when the center of mass of *B* enters into the region shown in Figure 3-4. The volume $v_G$ of this region is given by:

$$v_G(\theta,\varphi;\theta',\varphi') = 4\pi r^{3} \sin \chi_G \tag{63}$$

where $\chi_G$ is the angle between the normal vectors of graphene particles *A* and *B*.

The probability that graphene particles *A* and *B* contact is:

$$p_G(\theta,\varphi;\theta',\varphi') = \frac{v_G}{V} = \frac{4\pi r^3}{V}\sin\chi_G \qquad (64)$$

If there are $N_G$ graphenes in a volume $V$, the average number of graphenes that come into contact with the graphene particle $A$ is:

$$n_G(\theta,\varphi) = \int_0^{\pi}\int_0^{\pi} p_G(\theta,\varphi;\theta',\varphi')(N_G - 1)\Omega(\theta',\varphi')\sin\theta' d\theta' d\varphi' \qquad (65)$$

where $\Omega(\theta',\varphi')$ is the orientation density function. For large $N_G$ ($N_G >> 1$), the method used for the derivation of Equations (59)~(61) gives the total number of graphene-to-graphene contacts in the assembly ($\overline{n_{Gtot}}$ ) as:

$$\overline{n_{Gtot}} = \frac{(2\pi^2 r^3)N_G^2}{4V} \qquad (66)$$

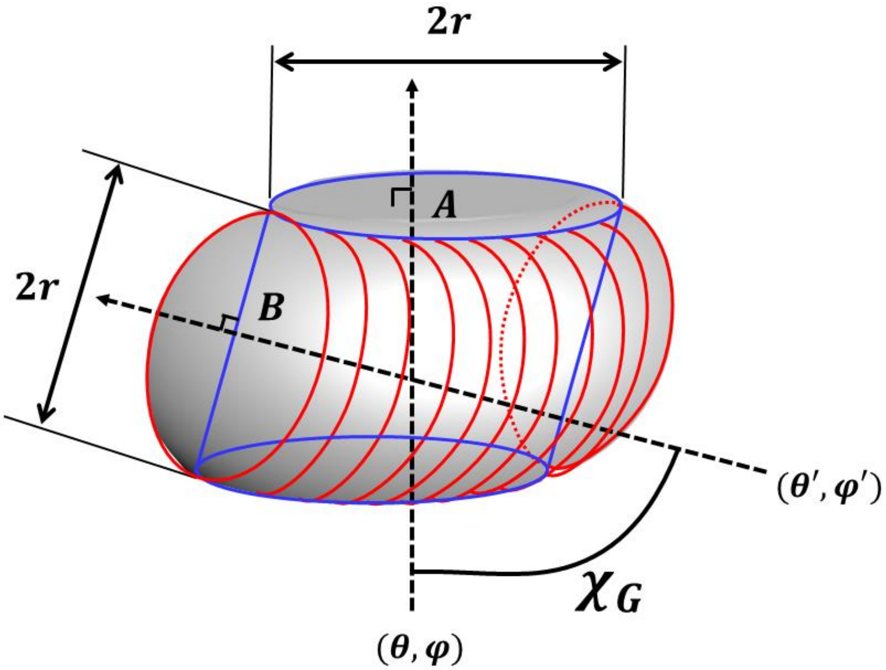

**Figure 3-4** A schematic drawing for calculating the contact probability of graphene particles *A* and *B*. Mobile graphene particle *B* will contact fixed particle *A* when the center of mass of *B* enters the region surrounded by the blue and red lines.

#### 3.3.2.2. Estimating the number of CNT-graphene contacts

The number of graphene-to-CNT contacts was calculated in a similar way to that used for the CNT-to-CNT and graphene-to-graphene contacts. Consider that arbitrary graphene particle *A* having an orientation of $(\theta, \varphi)$ is placed in a volume *V*. A CNT with an orientation of $(\theta', \varphi')$ will contact the graphene particle *A* when the center of mass of the CNT enters the region surrounded by the dotted lines shown in Figure 3-5. The volume of this region $v_{GC}$ can be calculated by:

$$v_{GC}(\theta,\varphi;\theta',\varphi') = \pi r^2 \lambda \left|\cos \chi_{GC}\right| \qquad (67)$$

where $\chi_{GC}$ is the angle between the CNT axis and the normal vector of the graphene particle.

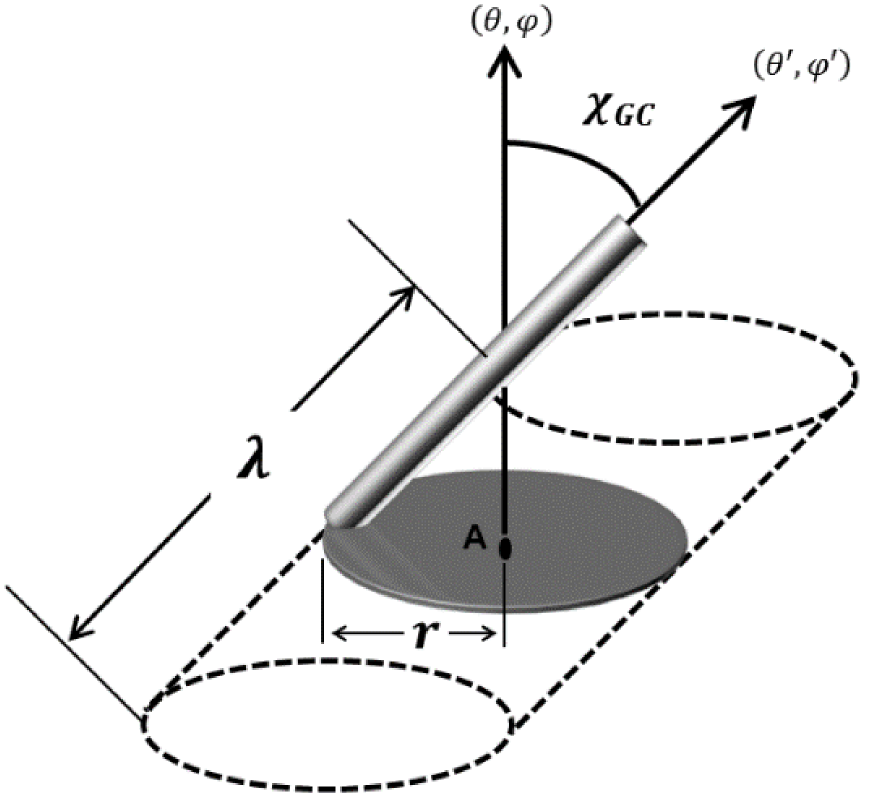

**Figure 3-5** A schematic diagram for explaining the contact condition of a CNT with graphene particle *A*. The CNT will contact *A* when the center of mass of the CNT enters into the region surrounded by the dotted lines.

The probability $p_{GC}$ that a CNT will contact $A$ is:

$$p_{GC}(\theta,\varphi;\theta'\varphi') = \frac{v_{GC}}{V} = \frac{\pi r^2 l}{V}\left|\cos\chi_{GC}\right| \tag{68}$$

The average number of contacts between CNTs and $A$ when a total of $N_C$ CNTs exist in the CNT/graphene assembly in a volume V is:

$$n_{GC}(\theta,\varphi) = \int_0^\pi\int_0^\pi p_{GC}(\theta,\varphi;\theta',\varphi')N_C\Omega(\theta',\varphi')\sin\theta' d\theta' d\varphi' \tag{69}$$

Using the same approach as that used in the derivation of Equations (59)–(61), the total number of graphene-to-CNT contacts ($\overline{n_{GCtot}}$) in the assembly of volume $V$ with $N_C$ CNTs and $N_G$ graphenes is:

$$\overline{n_{GCtot}} = \frac{\pi r^2 l N_C N_G}{2V} \tag{70}$$

### 3.3.2.4. Total number of contacts in CNT-graphene hybrids

Total number of contacts in CNT-graphene hybrids can be calculated by summing the number of CNT-to-CNT contacts ($\overline{n_{Ctot}}$), number of graphene-to-graphene contacts ($\overline{n_{Gtot}}$), and the number of graphene-to-CNT contacts ($\overline{n_{GCtot}}$). The total number of contacts between the CNTs and graphene particles in a hybrid can be expressed as:

$$\overline{n}_{TOT} = \frac{pDl^{2} N_{c}^{2}}{4V} + \frac{\left(2p^{2}r^{3}\right) N_{G}^{2}}{4V} + \frac{pr^{2} l \, N_{C} N_{G}}{2V} \tag{71}$$

Equation (71) assumes that the number of CNTs and graphene particles and their geometrical parameters are known in a specific volume. The morphologies and sizes of the CNTs and graphene are assigned as follows. Multi-walled CNTs (MWCNTs) having five walls and a length and diameter of 5 μm and 2 nm, respectively, are considered. The radius of a single-layered disk-shaped graphene particle is assigned to 160-nm (by considering the same mass as MWCNT). If the weight fraction of graphene and CNT are $m_G$ and $m_C$ ($m_G + m_C = 1$), with the assumed geometries and sizes of graphene particles and CNTs, then the total number of CNTs and graphene particles in a specific volume is $N_C = km_C$ and $N_G = km_G$ with an arbitrary proportional constant of $k$. Equation (71) can then be evaluated term-by-term. Figure 3-6a shows the calculated number of CNT-to-CNT, graphene-to-graphene, and CNT-to-graphene contacts. As the concentration of CNTs increases, the number of CNT-to-CNT contacts naturally increases, while the number of graphene-to-graphene contacts decreases. For the same mass case, the number of CNT-to-CNT contacts in the CNT-only assembly (i.e., the 100% CNT content case in Figure 3-6a) is larger than the number of graphene-to-graphene contacts in the graphene-only assembly (i.e., the 0% CNT content case in Figure 3-6a). This analysis suggests there is a high probability that a CNT will contact another CNT because of the high aspect (length/diameter) ratio, and furthermore that CNTs have an advantage over graphene particles concerning contacts. Thus, the total number of contacts in CNT/graphene hybrids increases as the CNT content increases and reaches a maximum when the packing of CNTs and graphene particles is densest. To obtain the CNT fraction at the maximum, Equation (71) is rewritten into a parabolic equation as a function of CNT content as follows:

$$\overline{n_{tot}} = -a\left(m_c - 0.567\right)^2 + b \tag{72}$$

where $\alpha$ and $\beta$ are positive constants. In this system, 56.7 wt% is the CNT fraction that can bring about the maximum number of contacts in the modeled CNT/graphene hybrids. At this concentration, the proportion of graphene-to-CNT contact is the largest (75.0%), followed by CNT-to-CNT (19.2%), and graphene-to-graphene (5.8%) contacts. A synergistic behavior of CNT/graphene hybrids can be observed at this CNT content.

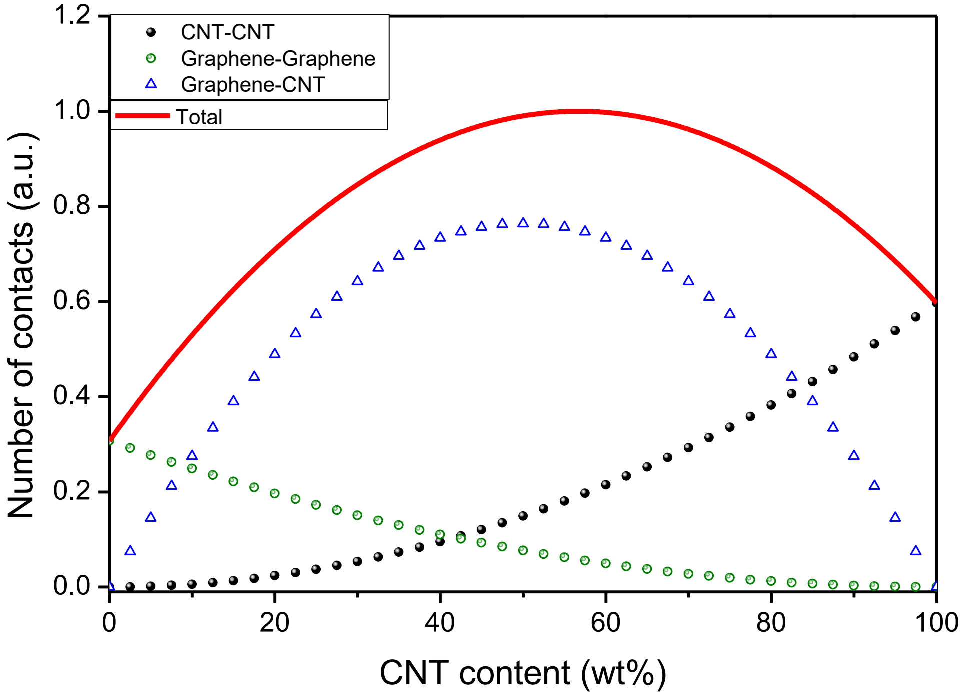
CNT-CNT
Graphene-Graphene
Graphene-CNT
Total
Number of contacts (a.u.)
1.2
1.0
0.8
0.6
0.4
0.2
0.0
0
20
40
60
80
100
CNT content (wt%)

(a)

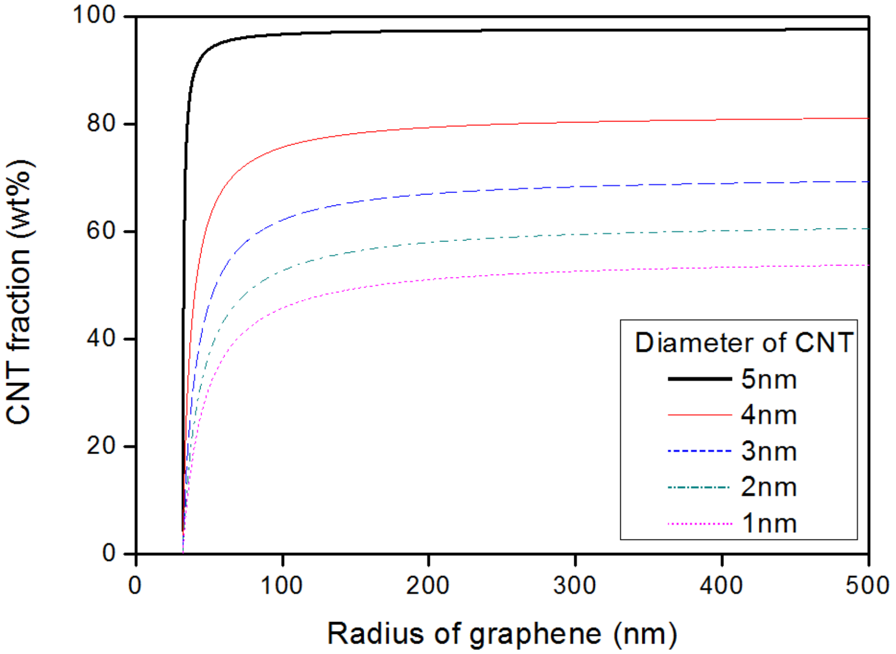
CNT fraction (wt%)
100
80
60
40
20
0
0
100
200
300
400
500
Radius of graphene (nm)
Diameter of CNT
5nm
4nm
3nm
2nm
1nm

(b)

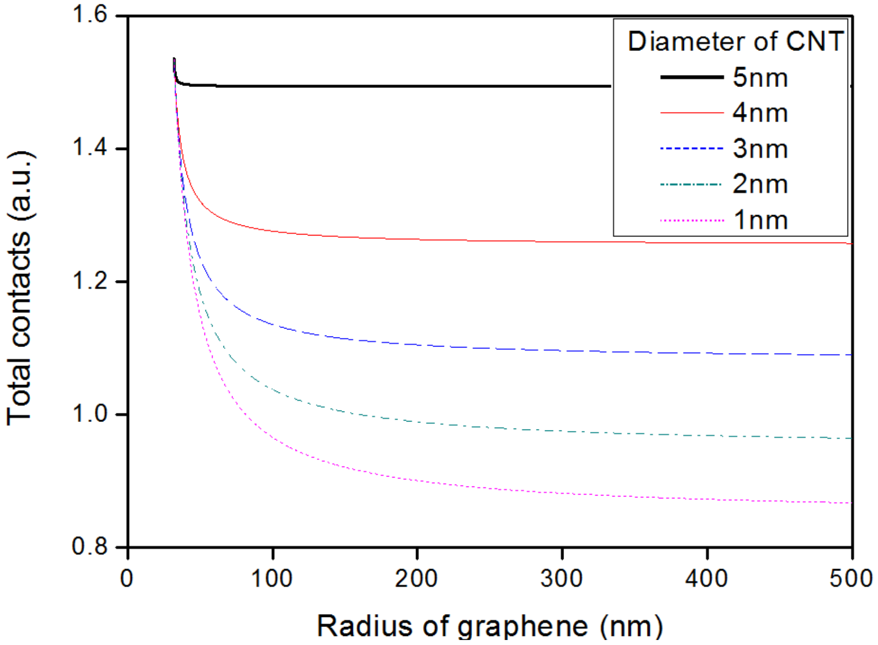

(c)

**Figure 3-6** Calculated number of contacts made by CNT and graphene particles in their hybrid assembly. (a) The number of CNT-to-CNT, graphene-to-graphene, and graphene-to-CNT contacts in the CNT/graphene hybrids as a function of the CNT content. In this system, 56.7 wt% is the CNT fraction that can bring about the maximum number of contacts in the modeled CNT/graphene hybrids. At this concentration, the proportion of graphene-to-CNT contact is the largest (75.0%), followed by CNT-to-CNT (19.2%), and graphene-to-graphene (5.8%) contacts. A synergistic behavior of CNT/graphene hybrids can be observed at this CNT content. (b) The effect of graphene particle radius and CNT diameter on CNT content at the maximum number of contacts. (c) The number of contacts calculated for different graphene and CNT sizes in (b).

Next, the effect of graphene particle size on the number of contacts was investigated. For simplification, the size of the graphene particles was assumed to be 160´ $g$ $(nm)$. The optimal CNT/graphene mass composition depends on the graphene particle size. Since we assumed the total mass of the CNT/graphene hybrids is fixed, if the mass fraction of graphene particles is $m_G$, the number of graphene particles can be expressed as $N_G = km_G/\gamma^2 = k(1 - m_C)/\gamma^2$ when the radius of the graphene particle changes from 160 nm to $160\gamma$ nm. The total number of contacts is then given by:

$$\overline{n_{tot}} = -\alpha'(m_c - m_{c\max})^2 + \beta' \qquad (73)$$

where $\alpha'$ and $\beta'$ are positive constants and $m_{c\max}$ represents the CNT content with the maximum number of contacts. Figure 3-6b shows the change in this quantity as a function of graphene particle size. As the radius of the graphene particle increases in the hybrid, the CNT content providing the maximum number of contacts also increases. However, this number levels off at a certain graphene size, suggesting that the CNT content does not need to further increase to maintain this maximum number of contacts in a hybrid containing large-sized graphene particles. The number of contacts itself decreases as the graphene particle size increases (Figure 3-6c).

The effect of CNT size on the number of contacts can be investigated by changing either its diameter or length. For simplicity, the mass of a CNT is assumed to be independent of its diameter and proportional to its length. By changing the length from 5 to 5$x$ μm, the number of CNTs can be expressed as $N_C = km_C/x$, assuming 2that the total mass of CNTs is fixed. Introducing this into Equation (71) reveals that the number of contacts is not influenced by the CNT length. Next, the effect of changing the CNT diameter is explored. The CNT content for the maximum contacts varies as shown in Figure 3-6b. As the diameter of a CNT increases, the CNT content for maximum contacts increases. Additionally, the number of contacts at its maximum increases with increasing CNT diameter.

The number of contacts that graphene and CNT particles can make in their hybrids can thus be calculated using a simplified geometry for the CNT and graphene. The model demonstrates that the condition of maximum contact occurs at a specific concentration of both materials. We can deduce that properties sensitive to such contact, e.g., electrical conductivity (see Equation (54)), will be maximized at that composition. We prepared randomly-mixed CNT/graphene hybrids using inkjet printing technology to validate this hypothesis.

### 3.3.3. Number of contacts for hybrids composed of different particle sizes

In section 3.3.2, we derived the number of CNT-to-CNT, CNT-to-graphene, and graphene–to-graphene contacts for same sized CNTs and graphene. Here, we extend our approach to cover CNTs and graphene with size distribution. If we consider the size distribution function of CNT length as $f_c(\lambda)$ as in Figure 3-7, the number of CNT-to-CNT contacts for mixture of CNTs with different sizes can be calculated as follows.

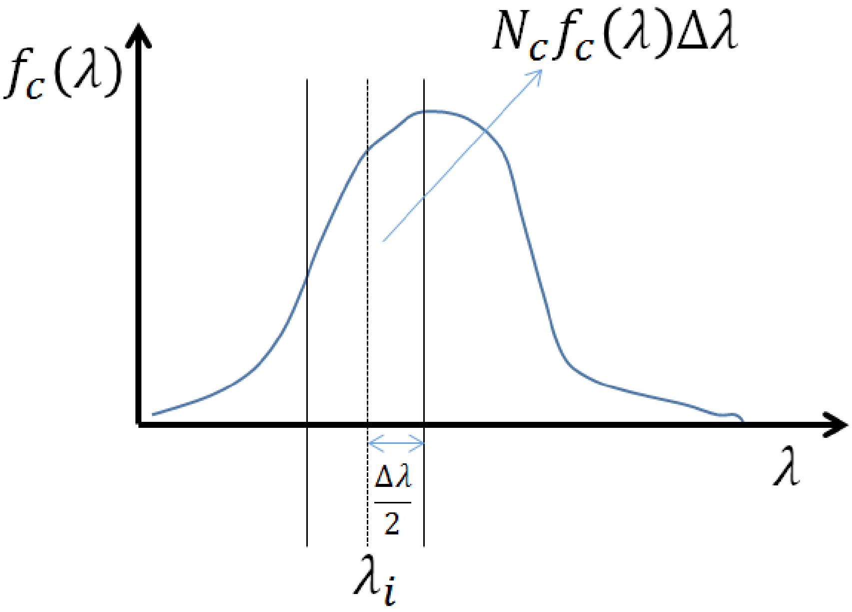

**Figure 3-7** An example of a graph showing size distribution of CNTs

If we consider the length of two CNTs in Figure 3-3 as $\lambda_i$ and $\lambda_j$, the volume of the region in this figure becomes

$$v_C = 2D\lambda_i\lambda_j \sin\chi_C \tag{74}$$

By using the same method from equation (57)-(61), the average number of contacts on CNT of length $\lambda_i$ with CNT of length $\lambda_j$ for random orientation is calculated by:

$$N_C f_C(\lambda_j)\Delta\lambda \frac{2D\lambda_i\lambda_j}{V}\frac{\pi}{4} \tag{75}$$

The average number of contacts on CNT of length $\lambda_i$ can be calculated by considering the length of all the other CNTs and is given by:

$$\overline{n_C} = \sum_{j=1}^{n} N_C f_C(\lambda_j)\Delta\lambda \frac{2D\lambda_i\lambda_j}{V}\frac{\pi}{4} \tag{76}$$

The total number of contacts can be calculated by multiplying half the number of CNTs of all length and is given by:

$$\overline{n_{Ctot}} = \frac{1}{2}\sum_{i=1}^{n}\sum_{j=1}^{n}(N_C f_C(\lambda_i)\Delta\lambda)(N_C f_C(\lambda_j)\Delta\lambda)\frac{2D\lambda_i\lambda_j}{V}\frac{\pi}{4} \tag{77}$$

Equation (77) can be changed into the following integral form:

$$\overline{n_{Ctot}} = \int_0^\infty\int_0^\infty \frac{1}{2}\frac{\pi N_C{}^2 D}{2V} f_C(\lambda')\lambda' f_C(\lambda)\lambda d\lambda' d\lambda \tag{78}$$

By integrating Equation (78), the total number of CNT-to-CNT contacts for CNTs with size distribution is calculated:

$$\overline{n_{Ctot}} = \frac{\pi D}{4V} N_C{}^2 (\overline{\lambda})^2 \tag{79}$$

where $\overline{\lambda}$ is the mean length of CNTs. Comparing Equation (79) with (62), it is clear that only the mean length of CNTs is necessary for estimating the number of CNT-to-CNT contacts for CNT assembly with size distribution. If we also consider the diameter of CNTs with different sizes, $D$ will be replaced with $\overline{D}$ ( the mean diameter of CNTs) in Equation (79). Therefore, the total number of CNT-to-CNT contacts is proportional to the average length, average diameter and total number of CNTs.

In case of graphene-to-graphene contacts, we consider the size distribution of graphene radius as $f_G(\lambda)$. In Figure 3-4, if we consider the radius of two graphene particles in contact as $r_i$ and $r_j$, the volume of the region shown in that figure becomes:

$$v_G = 2\pi r_i r_j (r_i + r_j) \sin \chi_G \tag{80}$$

By using the same method we have shown above, the average number of contacts on graphene of radius $r_i$ with graphene of radius $r_j$ becomes:

$$(N_G f_G(r_j)\Delta r) \frac{2\pi r_i r_j (r_i + r_j)}{V} \frac{\pi}{4} \tag{81}$$

The average number of contacts on graphene of radius $r_i$ becomes:

$$\overline{n_G} = \sum_{j=1}^{n} (N_G f_G(r_j)\Delta r) \frac{2\pi r_i r_j (r_i + r_j)}{V} \frac{\pi}{4} \tag{82}$$

The total number of graphene to graphene contacts in mixture of graphene particles with different sizes becomes:

$$\overline{n_{Gtot}} = \frac{1}{2} \sum_{i=1}^{n} \sum_{j=1}^{n} (N_G f_G(r_j)\Delta r)(N_G f_G(r_i)\Delta r) \frac{2\pi r_i r_j (r_i + r_j)}{V} \frac{\pi}{4} \tag{83}$$

$$\overline{n_{Gtot}} = \frac{1}{2}\int_0^\infty \int_0^\infty \frac{\pi^2 N_G{}^2}{2V} f_G(r') f_G(r) r' r (r'+r) dr' dr \qquad (84)$$

By calculating equation (84), the total number of graphene-to-graphene contacts is obtained and is given by:

$$\overline{n_{Gtot}} = \frac{\pi^2 N_G{}^2 \overline{r^2}\,\overline{r}}{2V} \qquad (85)$$

Equation (85) shows that the total number of graphene-to-graphene contacts for different graphene sizes is proportional to the mean radius of graphene, mean square of graphene radius, and the total number of graphene particles.

In case of graphene-to-CNT contacts, if we consider mixture of graphene particles and CNTs with different sizes, the volume of the region in the Figure 3-5 becomes:

$$v_{GC} = \pi r_i^2 \lambda_j \left|\cos \chi_{GC}\right| \qquad (86)$$

By using the same method we used above, the total number of graphene-to-CNT contacts is calculated as

$$\overline{n_{GCtot}} = \int_0^\infty \int_0^\infty \frac{N_C N_G f_C(\lambda) f_G(r) r^2 \lambda \pi}{2V} dr d\lambda \qquad (87)$$

Finally, Equation (87) gives:

$$\overline{n_{GCtot}} = \frac{\pi}{2V} N_C N_G \overline{r^2}\,\overline{\lambda} \qquad (88)$$

Equation (88) shows that total number of graphene-to-CNT contacts in mixture of graphene and CNT with different sizes is proportional to the mean square of graphene radius, the mean length of CNTs, the number of CNTs and graphene particles.

### 3.3.4. Calculation of percolation threshold for CNT assembly

Our model was aimed to estimate the electrical conductivity of CNT/graphene hybrids. We have found out that the percolation threshold of CNT composites can be estimated using the equations derived in our work. In previous research, the critical volume fraction ensuring the percolation was estimated by calculating the probability of one cylinder intersecting at least two other cylinders. In a work by Munson-McGee, the critical volume fraction was chosen when the probability that one cylinder intersecting at least two other cylinder is 0.5.[138] The probability that one cylinder contact another cylinder is obtained by dividing the excluded volume by the total volume where the cylinders can be located as in our work. Following Munson-McGee's work, the critical volume fraction can be obtained using our approach (the number of contacts) as follows.

We assume that each CNT in the conducting paths must have at least 2 contacts with other CNTs. We set the critical concentration of percolation when the average number of contacts becomes 2. The average number of contacts on an arbitrary CNT can be expressed by,

$$\bar{n} = \frac{\pi D \lambda^2 N}{2V} (= 2) \tag{89}$$

The volume fraction of CNT (*Φ*) can be calculated by dividing the total volume of CNTs by the total volume where CNT can be located.

$$\phi = \frac{N \pi D^2 \lambda}{4V} \tag{90}$$

The critical volume fraction ($\Phi_c$) of the CNTs when the average number of contacts on CNT becomes 2 can be calculated by relating Equations (89) and (90), resulting in,

$$\phi_C = \frac{D}{\lambda} = (aspect\ ratio)^{-1} \tag{91}$$

As shown in Equation (91), the critical volume fraction of CNT ($\Phi_c$) is the inverse of the aspect ratio. The relation between the aspect ratio of CNT and the percolation threshold is shown in the Figure 3-8. The calculated percolation threshold here has almost the same value with the percolation threshold calculated in other works.[139]

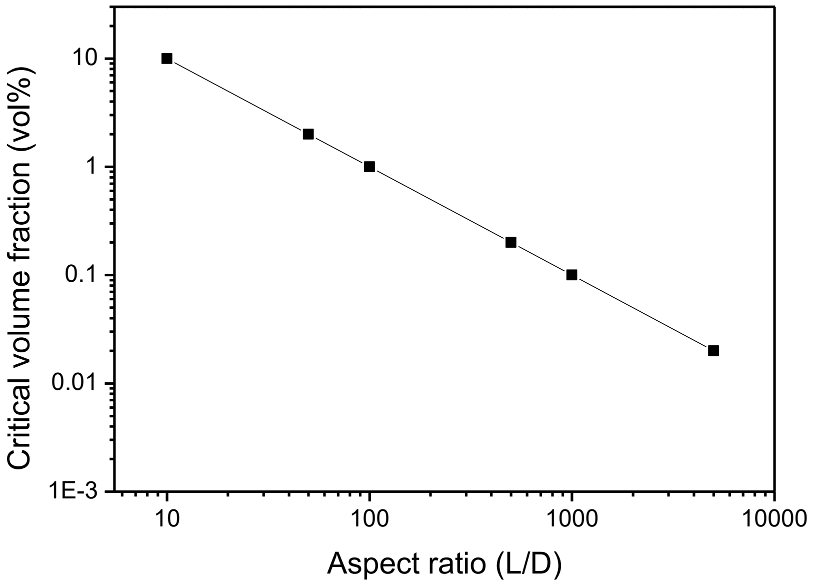

**Figure 3-8** The relation between aspect ratio of CNT and percolation threshold.

## 3.4. Experimental results

### 3.4.1. Characterization of the CNT/graphene hybrid inks

There are several requirements for inks to be printed acceptably by an inkjet printer. The inks should have relatively low viscosity (e.g., 1–30 cP) and low volatility (boiling point > 100 ºC)[140] Furthermore, the particles in the inks should be smaller than 1/100 times the nozzle diameter (e.g., 200 nm in the printer used in this study) to prevent nozzle clogging. The Methods section provides details of the various graphene and CNT inks that were prepared; each ink viscosity was within the printable range (Figure 3-9).

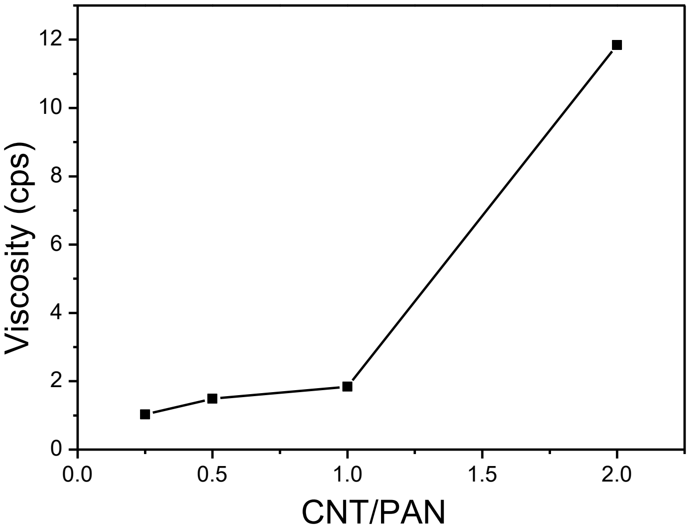

(a)

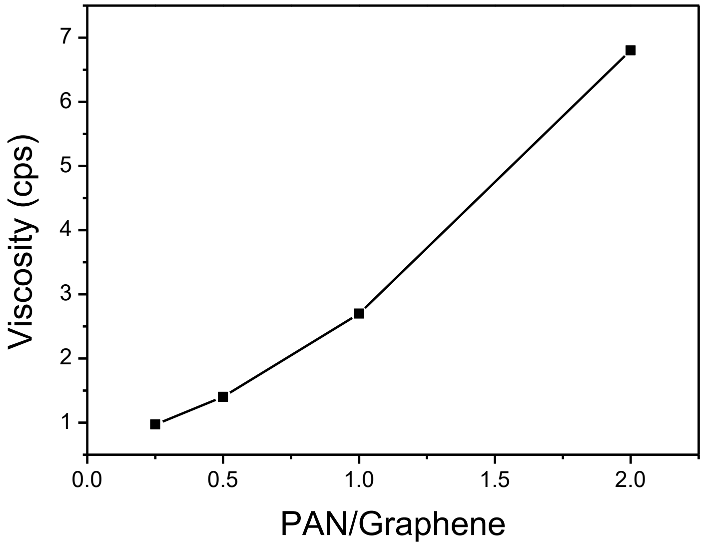

(b)

**Figure 3-9** Viscosities of (a) CNT ink and (b) graphene ink.

The particle sizes measured using dynamic light scattering (DLS) showed that those inks prepared with less poly(acrylonitrile) (PAN) (used as a dispersion aid for the graphene and CNT particles) had smaller particle sizes. Graphene and CNT inks prepared with graphene:PAN fractions of 1:0.25, 1:0.5, 1:1, and 1:2 and with CNT:PAN fractions of 1:0.25, 1:0.5, 1:1, and 1:2, respectively, had average particle sizes < 200 nm (Figure 3-10). CNT and graphene inks containing less PAN had higher zeta potentials and smaller particle sizes (Figure 3-11).

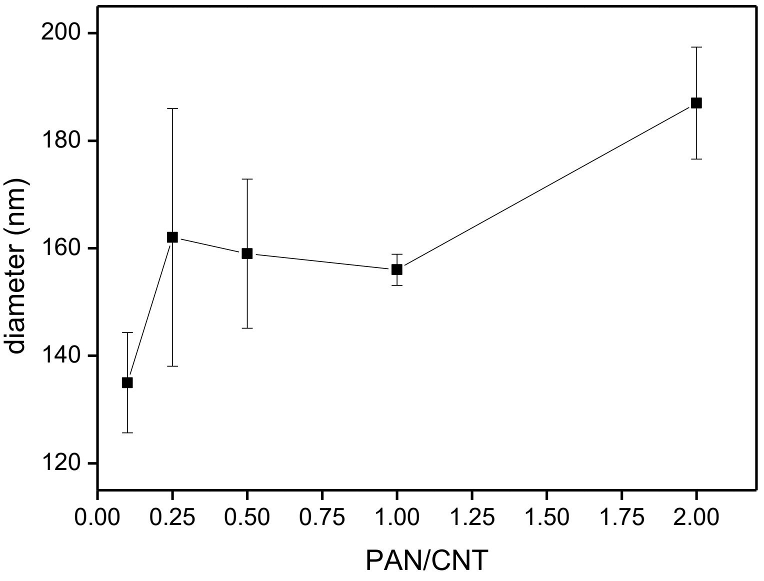

(a)

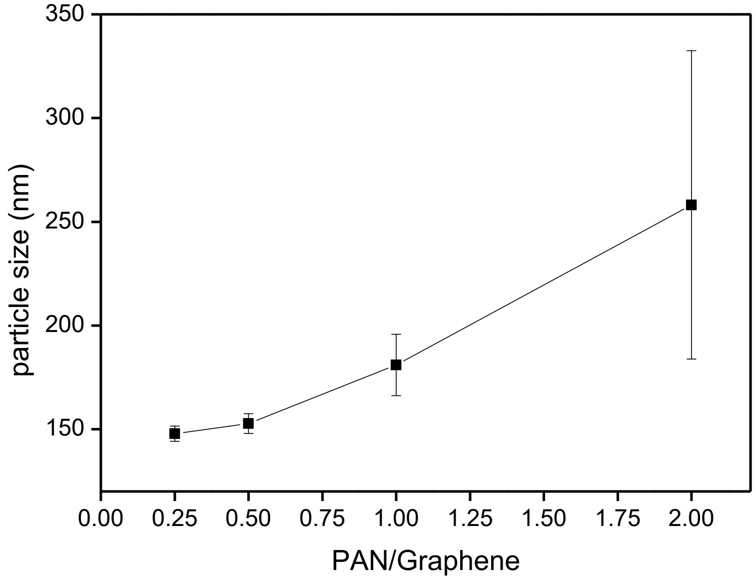

(b)

**Figure 3-10** Particle sizes of PAN-wrapped CNTs and graphene particles measured using DLS as a function of PAN content.

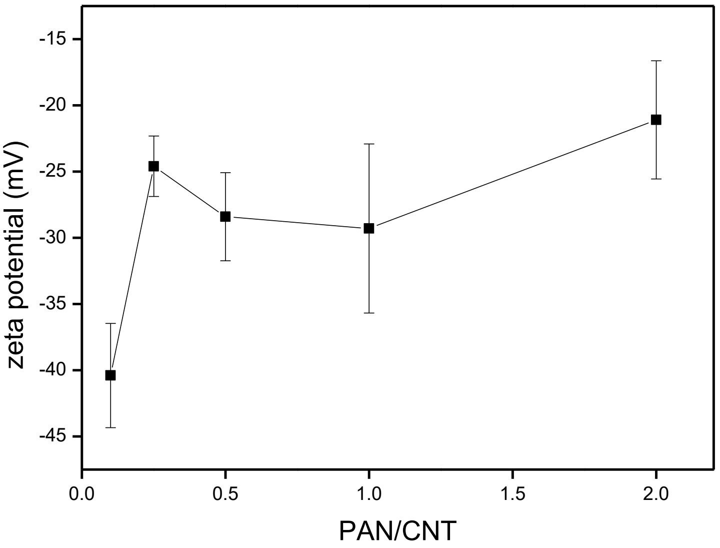

(a)

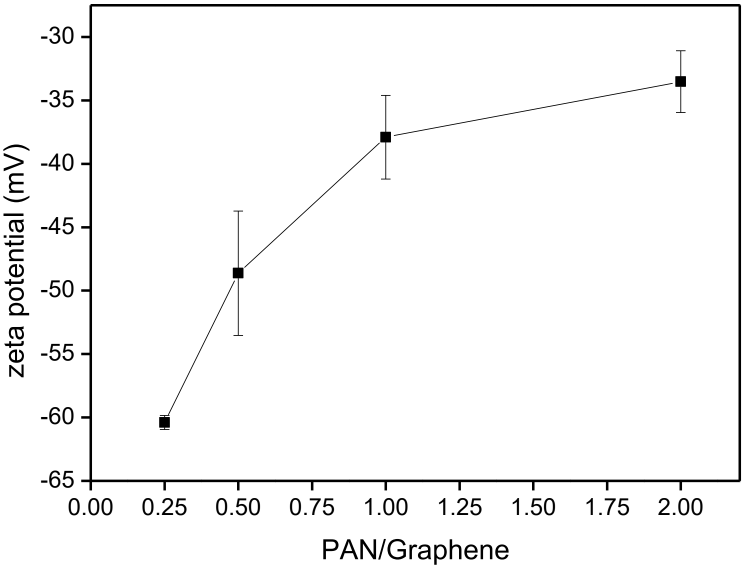

(b)

**Figure 3-11** Zeta potentials of PAN-wrapped CNTs and graphene particles measured using ELS as a function of PAN content.

Those graphene and CNT inks with graphene:PAN and the CNT:PAN fractions of 1:0.25 were selected for inkjet printing because they satisfied the ink requirements and were expected to have greater electrical conductivity because of the smaller amount of PAN. Thermogravimetric analysis (TGA) determined the weight fractions of graphene and CNT in the graphene and CNT inks with respect to the solvent as 0.394 and 0.178%, respectively (Figure 3-12).

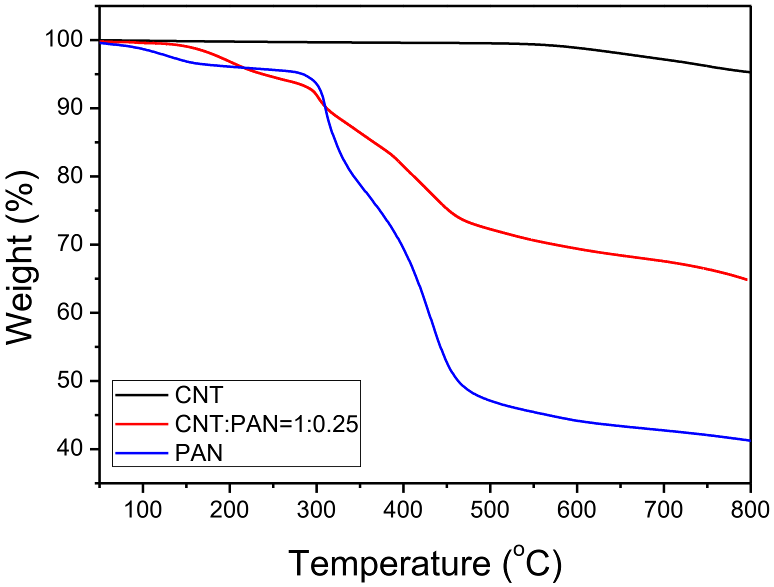

(a)

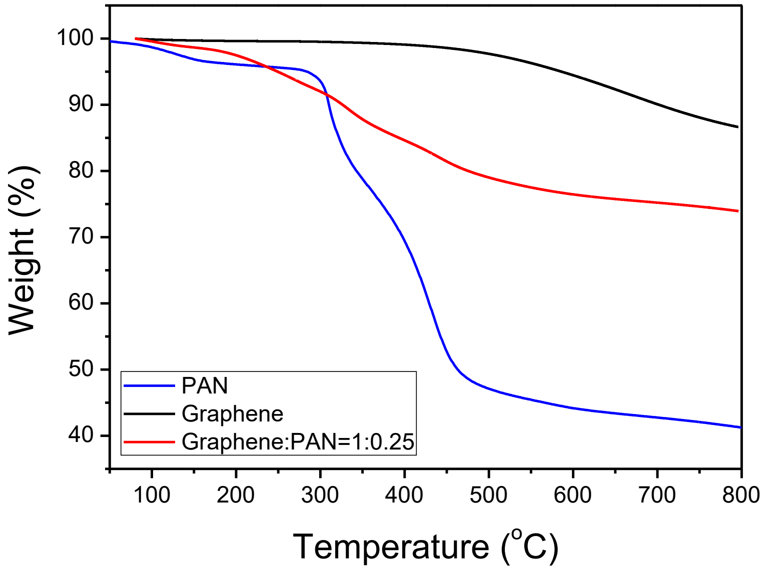

(b)

**Figure 3-12** TGA curves of (a) CNT and (b) graphene inks.

### 3.4.2. Morphology of the inkjet-printed CNT/graphene hybrids

The morphologies of the printed inks on photo paper were analyzed using scanning electron microscopy (SEM). The graphene particles were randomly deposited on the paper (Figure 3-13a). The PAN molecules attached to the graphene gave a rough surface to the printed ink. Figure 3-13b shows that the printed layer densified as the number of printings increased. Figures 3-13c and d show the morphologies of the CNT inks printed 3 and 15 times, respectively. The CNTs were randomly oriented and distributed on the substrate, suggesting that the printed CNTs exhibited isotropic properties. The packing densities of the printed CNT and graphene particles increased with increasing numbers of printings, implying that the conducting path also increased. Figures 3-13e and f show SEM images of the graphene and CNT hybrid inks that were printed 15 times; the inks contained 12 and 81 wt% of CNTs, respectively. The graphene and CNT particles were randomly distributed and oriented by the inkjet printing process and had multiple interparticle contacts.

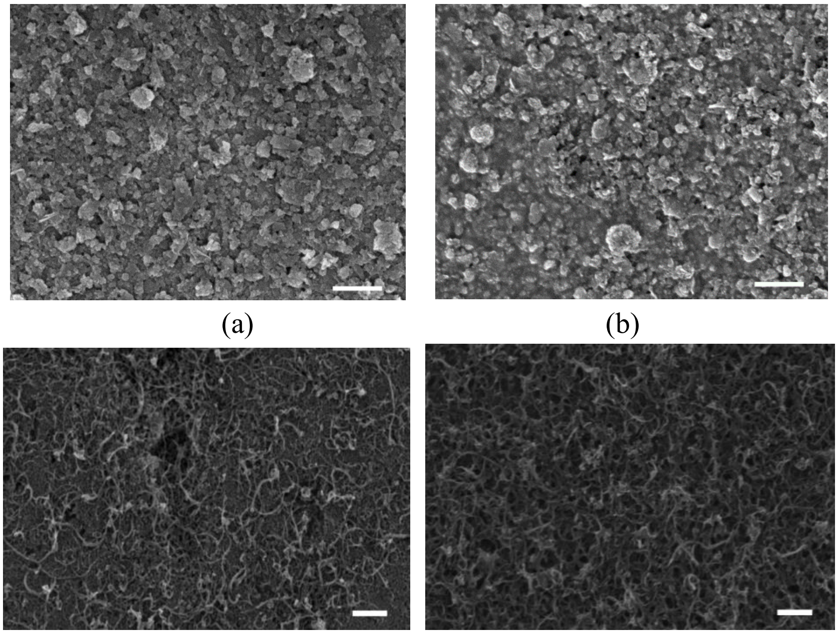

(a) (b)

(c) (d)

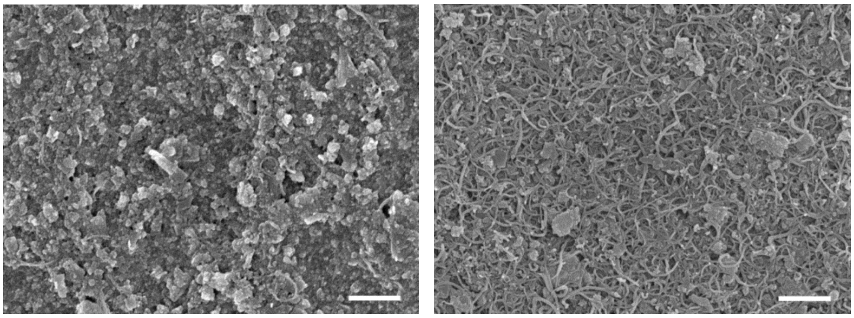

(e) (f)

**Figure 3-13** SEM images of graphene particles, CNTs, and their hybrid inks printed on photo paper. The scale bar is 500 nm in all images. (a) and (b): Graphene inks printed 3 and 15 times. The graphene particles were randomly deposited on the paper. The PAN molecules attached to the graphene gave a rough surface to the printed ink. The printed layer was densified as the number of printings increased. (c) and (d): CNT inks printed 3 and 15 times. The CNTs were randomly oriented and distributed on the substrate. (e) and (f): Morphologies of hybrid inks prepared with the CNT fractions of 12 and 81 wt% after printing 15 times. The graphene and CNT particles were randomly distributed and oriented by the inkjet printing process and had multiple interparticle contacts.

### 3.4.3. Electrical conductivity of CNT/graphene hybrids

The electrical conductivity of printed ink was measured using the four-point probe method. Figure 3-15a shows the sheet resistance of the printed graphene and CNT inks. The printed films prepared with a small number of printings were not electrically conductive because the concentration of conductive particles was insufficient to form conducting paths. The sheet resistance of the printed inks decreased as the number of printings increased. The electrical conductivities of the various inks were compared by measuring the thickness of a printed film by atomic force microscopy (AFM) (Figure 3-14).

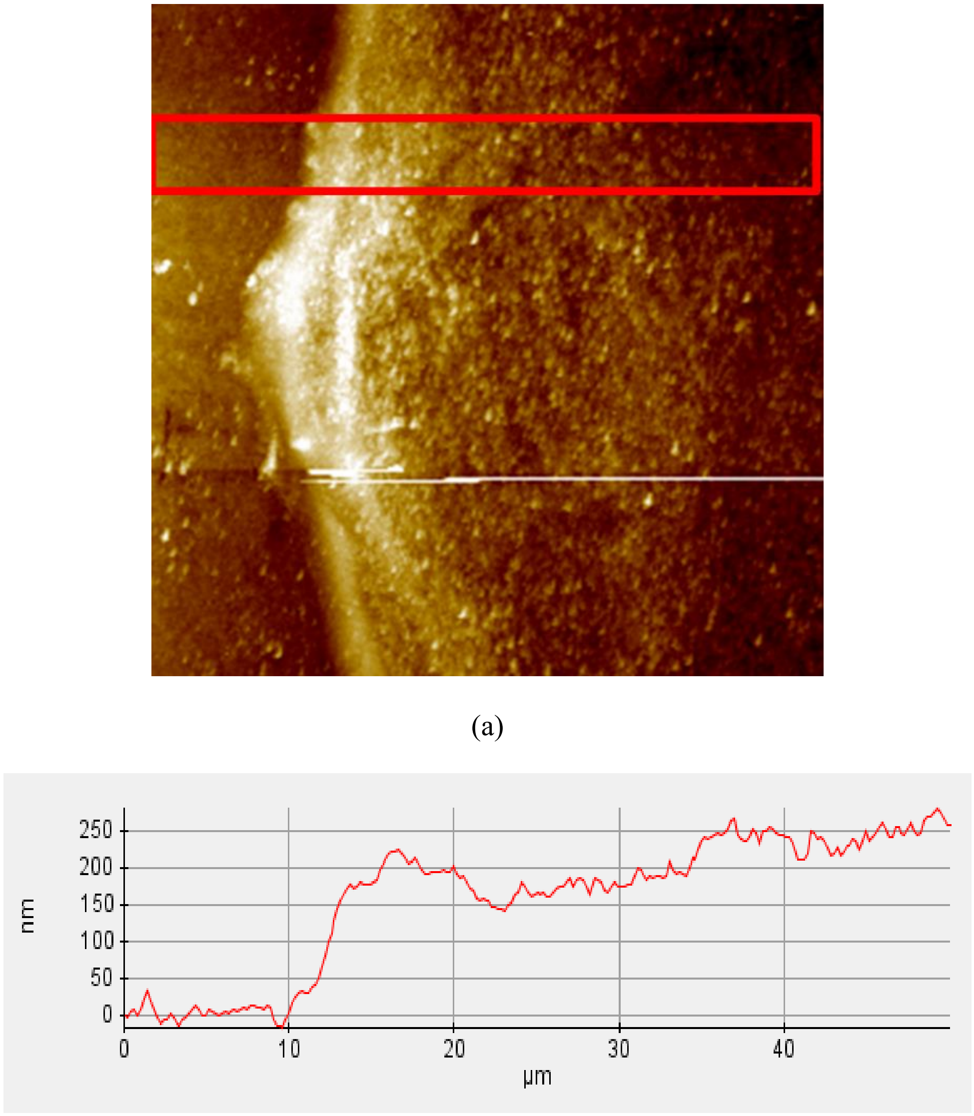

(a)

(b)

**Figure 3-14** (a) An AFM image of a printed CNT ink and (b) heights of the region surrounded by the red rectangle shown in (a).

The thickness of the printed inks linearly increased with increasing number of printings. The thickness of the printed film was 21.3 nm and 15.9 nm per printing for the CNT and graphene inks, respectively (Figure 3-15b). Thickly printed inks had a constant conductivity for all thicknesses and thus resembled the bulk material, whereas thinly printed inks showed a percolation threshold, i.e., the conductivity decreased as the thickness decreased. The sheet resistances of the printed graphene and CNT inks at the thickness of 320 nm were 82000 and 5000 $\Omega$ sq$^{-1}$, respectively. Although pure graphene has a higher electrical conductivity than pure CNTs,[51, 136] in this work the CNT inks had higher electrical conductivities than pure graphene because the CNTs formed a better conductive network. The electrical conductivities of the printed CNT and graphene inks were lower than published elsewhere;[133, 141] this was attributed to the presence of PAN in the printed film. TGA showed that the weight fraction of PAN with respect to the solvent was 0.28 and 0.56 wt% for the graphene and CNT inks, respectively, which are not negligible amounts. PAN improved the dispersion of graphene and CNT particles in solution but it also blocked the conductive paths between particles. Reducing the amount of PAN without disrupting the stability of the inks will improve the electrical properties of the printed inks.

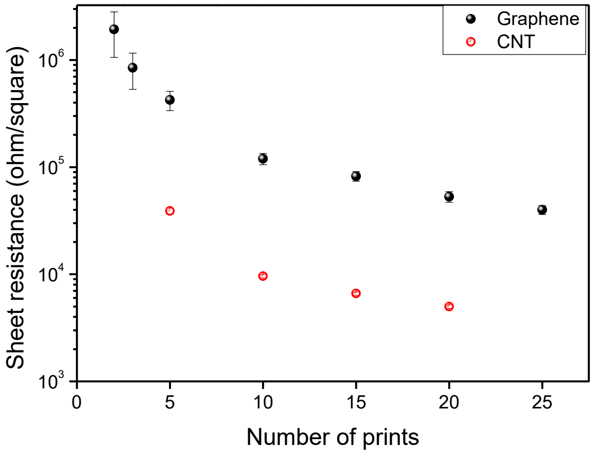
Graphene
CNT
Sheet resistance (ohm/square)
$10^6$
$10^5$
$10^4$
$10^3$
0
5
10
15
20
25
Number of prints

(a)

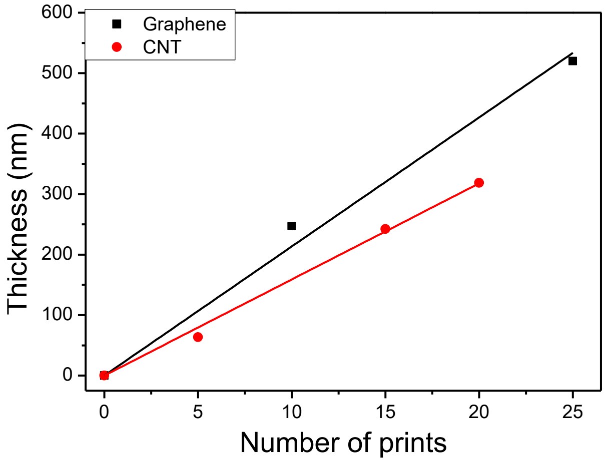
Graphene
CNT
Thickness (nm)
600
500
400
300
200
100
0
0
5
10
15
20
25
Number of prints

(b)

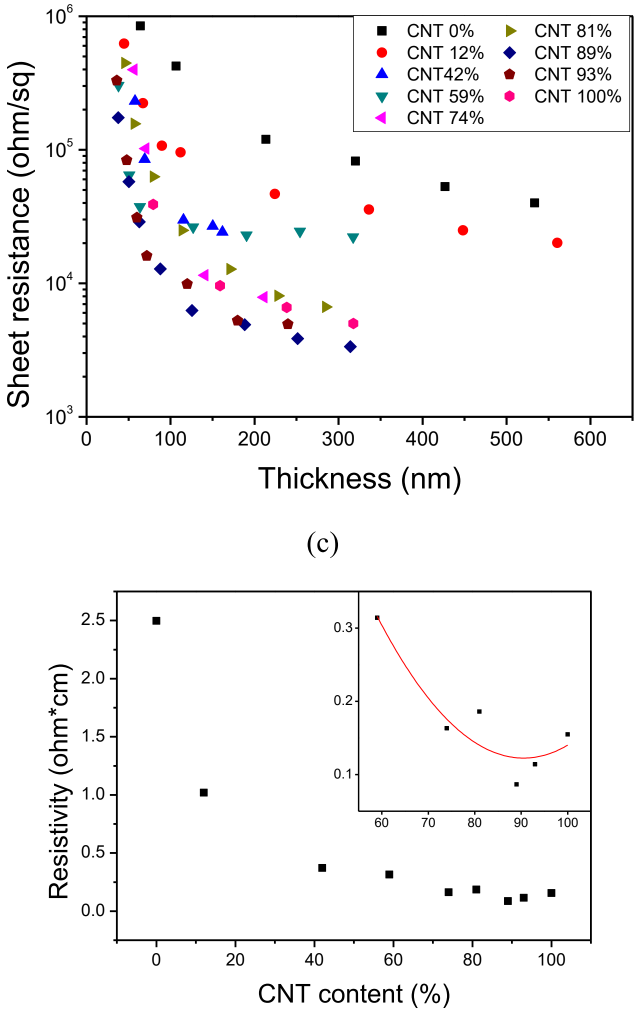

(c)

(d)

**Figure 3-15** Electrical properties of printed graphene and CNT inks. (a) Decreased sheet resistance of printed graphene and CNT inks as the number of printings increased. (b) Thickness of printed graphene and CNT inks as a function of the number of printings. (c) Sheet resistance of CNT/graphene hybrid inks as a function of the printed thickness and the CNT content. (d) Resistivity of the printed hybrid inks as a function of the CNT content, demonstrating a synergistic effect, i.e., the resistivity of the hybrid ink is lower than that of either pure CNT ink or graphene ink.

The electrical properties of the CNT/graphene hybrid inks are shown in Figures 3-15c–d. All of the hybrid inks printed on the photo paper exhibited decreased sheet resistance as the number of printings increased. The resistivity of the printed ink was calculated by linearly fitting the sheet resistance to 1/thickness. The resistivity of the printed hybrid inks decreased as the CNT content increased, because the increased number of interparticle contacts (see Figure 3-6a) expanded the conductive network. The resistivity of the printed hybrid inks exhibited a minimum lower than that of pure CNT ink at a given CNT content. The resistivities of printed graphene and CNT inks were 2.5 and 0.154 Ω·cm, respectively, while that of the printed hybrid ink with a CNT content of about 89% was 0.087 Ω·cm. This synergistic effect was predicted in the contacts calculation, i.e., that the number of CNT-to-CNT, graphene-to-graphene, and CNT-to-graphene interparticle contacts would be at a maximum at a specific CNT content. Figure 3-6b shows the effect of CNT diameter and graphene radius on CNT content at the maximum number of contacts.

The size of graphene and CNT when the maximum number of contacts occurs at certain composition can be calculated. We applied $\lambda = 5x$ μm, $r = 0.16\gamma$ μm, $N_C = km_C/x$ and $N_G = k(1 - m_C)/\gamma^2$ into Equation (71), resulting in Equation (92).

$$\overline{n_{tot}} = \frac{\pi k^2}{4V}\left(25Dm_C{}^2 + \frac{0.0257}{\gamma}(1-m_C)^2 + 0.256m_C(1-m_C)\right) \tag{92}$$

The CNT weight fraction at the maximum number of contacts ($m_{Cmax}$) can be calculated when Equation (92) is simplified into Equation (73) form and $m_{Cmax}$ is given by:

$$m_{C\max} = \frac{0.0514/\gamma - 0.256}{50D - 0.512 + 0.0514/\gamma} \tag{93}$$

In case of experimental results in our work, the maximum number of contacts occurred when the CNT content was 89%. When 89% is applied to $m_{Cmax}$, the relation between $D$ and $\gamma$ can be obtained:

$$D = \frac{1.28\times10^{-4}}{\gamma} + 4.5\times10^{-3}\mu m \tag{94}$$

Since $\gamma = \frac{r}{160nm}$, Equation (94) can be expressed in terms of the diameter of CNT and the radius of graphene as follows.

$$D = \frac{20.48}{r} + 4.5nm \tag{95}$$

This relation is plotted in Figure 3-16. It shows the diameter of CNT and radius of graphene when the maximum number of contacts at a CNT content of 89% occurs. The approach used in this study is thus suitable for investigating the properties of CNT/graphene hybrids, in particular the electrical conductivity.

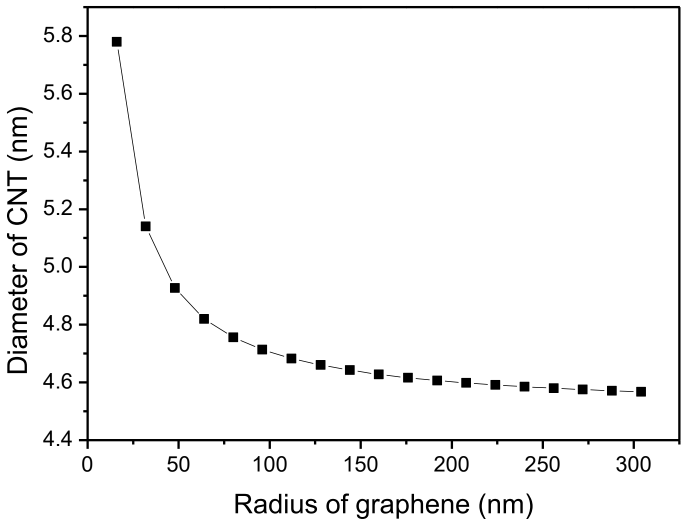

**Figure 3-16** Relation between the diameter of CNT and radius of graphene when the maximum number of contacts occurs at CNT content of 89%

## 3.5. Other examples using the model

### 3.5.1. Application of the models in SWNT/MWNT hybrid

The method used to calculate electrical conductivity of CNT/graphene hybrid can be applied to other electrically conductive composites. Electrical conductivity of CNT assemblies which is composed of two different types of CNTs are calculated using this method. In this work, we have predicted electrical conductivity of the SWNT/MWNT hybrid at different compositions and compared it with the experimental results. MWNT and SWNT used in this work has large difference in the diameter and length. The length and diameter of SWNT are 5~10μm and 1.2~2nm respectively. The length and diameter of MWNT are 50~150μm and 7~12nm respectively.

### 3.5.2. Predicted electrical conductivity of SWNT/MWNT hybrid

We assumed SWNT/MWNT hybrid of volume $V$ which is composed of $N_M$ MWNTs and $N_S$ SWNTs. $D_M$ and $\lambda_M$ are diameter and length of MWNT respectively. $D_S$ and $\lambda_S$ are diameter and length of SWNT respectively. Following the same method as in section 3.2.2., the number of MWNT-to-MWNT contacts ( $\overline{n_{MM}}$ ), SWNT-to-SWNT contacts ( $\overline{n_{SS}}$ ) and MWNT-to SWNT contacts( $\overline{n_{MS}}$ )can be calculated as in Equation (96)~(98)

$$\overline{n_{MM}} = \frac{\pi D_M \lambda_M{}^2 (N_M)^2}{4V} \tag{96}$$

$$\overline{n_{SS}} = \frac{\pi D_S \lambda_S{}^2 (N_S)^2}{4V} \tag{97}$$

$$\overline{n_{MS}} = \frac{\pi (D_M + D_S) \lambda_M \lambda_S N_M N_S}{4V} \tag{98}$$

The total number of contacts in the MWNT/SWNT hybrid is the sum of $\overline{n_{MM}}$ , $\overline{n_{SS}}$ and $\overline{n_{MS}}$ .

The diameter, length of SWNT and MWNT from the provided data were used. Figure 3-17 (a) shows measured data of electrical resistance of SWNT and MWNT composites at different concentrations. Figure 3-17 (b) shows calculated results of 1/(number of contacts) of SWNT and MWNT composites at different concentrations. Equation (96) and (97) are used in this calculation. Length, diameter of 7.5µm, 1.6nm were used for SWNT and length, diameter of 100µm, 9.5nm were used for MWNT. 1/(number of contacts) is proportional to electrical resistance. By comparing Figure 3-17 (a) and (b), it can be concluded that calculated results of resistance of SWNT and MWNT composites at different concentrations are similar to the experimental results. Experimental data were provided by Nepes corporation.

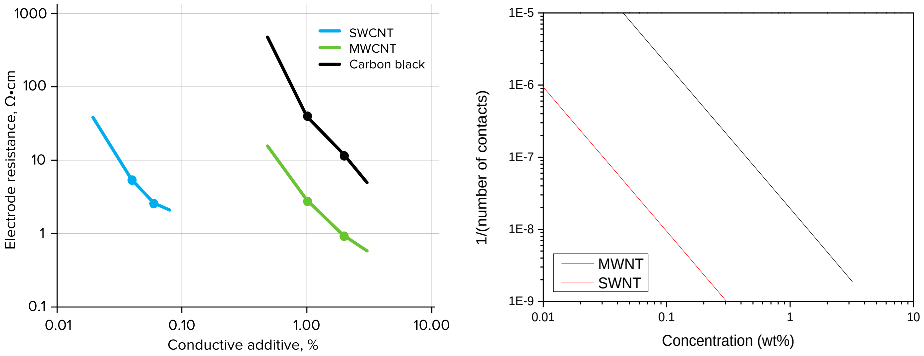

(a) (b)

**Figure 3-17** (a) Resistivity data of SWNT and MWNT composites at different concentrations from experiment. (b) Calculated results of 1/(number of contacts) of SWNT and MWNT composites at different concentrations.

Number of particles and number of contacts of SWNT/MWNT hybrid at different SWNT/(MWNT+SWNT) ratios were calculated. The number of each particle was calculated by dividing total volume of each particles by the volume of one particle. The number of contacts were calculated using the calculate number of particles and equation (96)~(98). The results are in Figure 3-18. Total number of CNT particles when the ratio of SWNT is 100%, is 470 times larger than when the ratio of SWNT is 0%. This difference comes from the large volume difference between SWNT and MWNT. Figure 3-18 (b) shows the calculated results of the number of contacts. Each type of contacts is plotted in this graph. The number of contacts which is proportional to the electrical conductivity, increases as the ratio of SWNT increases. Total number of contacts when the ratio of SWNT is 100%, is 209 times larger than when the ratio of SWNT is 0%. The reason for this large difference is the large increase in the number of particles.

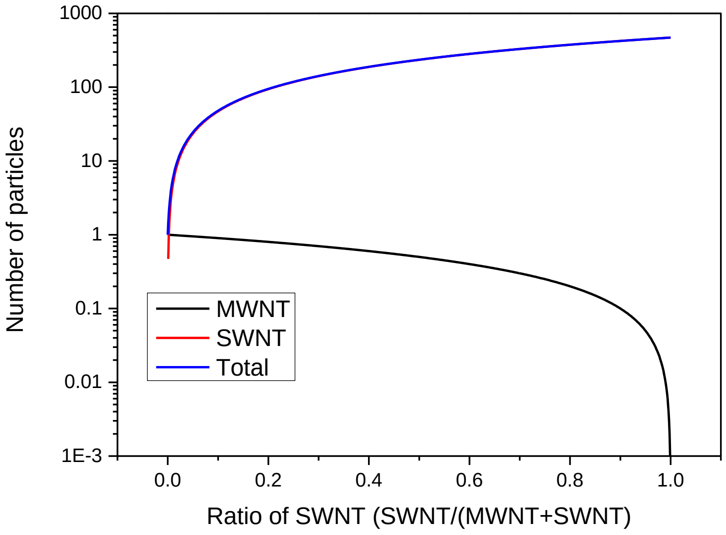

(a)

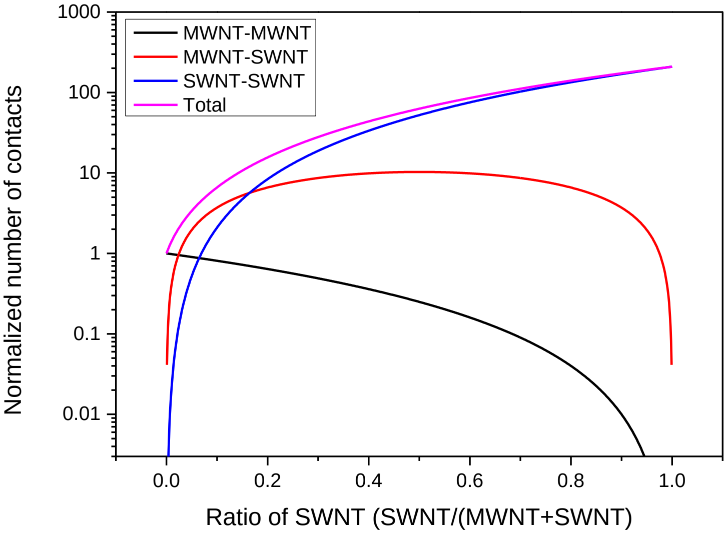

(b)

**Figure 3-18** (a) Calculated results of number of particles of SWNT/MWNT hybrid at different SWNT/(MWNT+SWNT) ratios. Total number of particles when the ratio of SWNT/(MWNT+SWNT) is 0, is normalized to 1. (b) Calculated results of number of contacts of SWNT/MWNT hybrids at different SWNT/(MWNT+SWNT) ratios. Number of contacts when the ratio of SWNT/(MWNT+SWNT) is 0, is normalized to 1.

### 3.5.3. Experimental result of the SWNT/MWNT hybrid

0.4% MWNT and 0.4% SWNT dispersed in NMP were mixed at different ratios and applied on PET film and dried. The coated samples, thickness and sheet resistance data were provided by Nepes corporation. The surface morphology of the film was observed using scanning electron microscope (SEM). Figure 3-19 shows the SEM images of the coated films. It shows that SWNT and MWNTs are well mixed in the hybrid film.

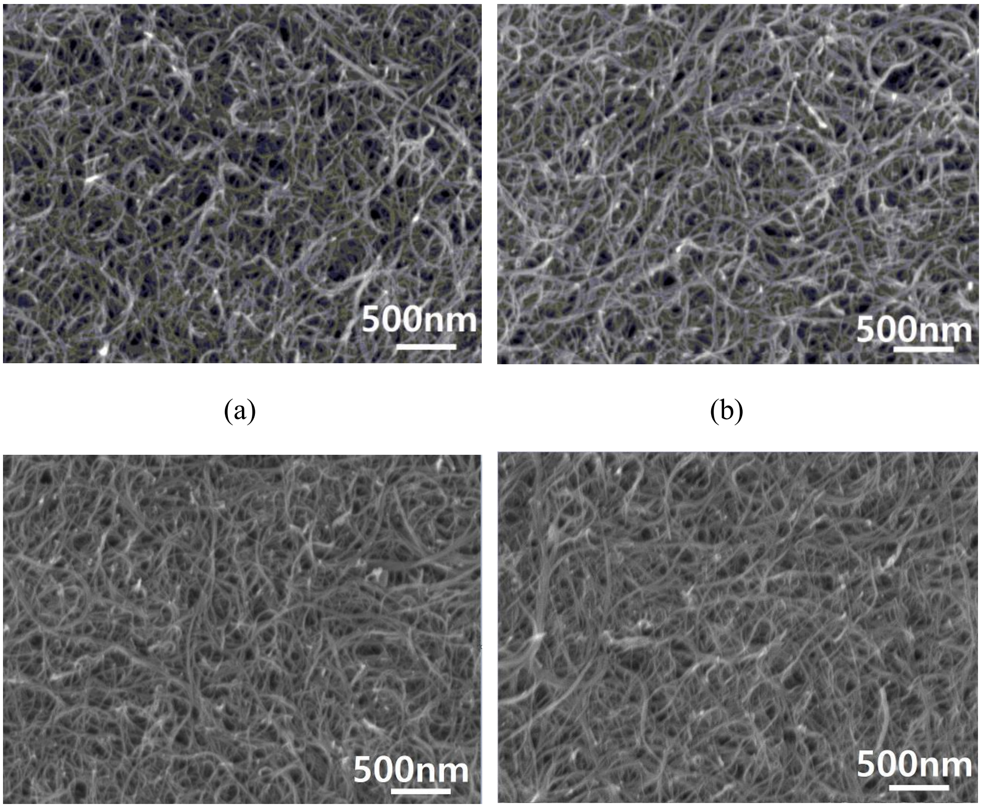

(a) (b)

(c) (d)

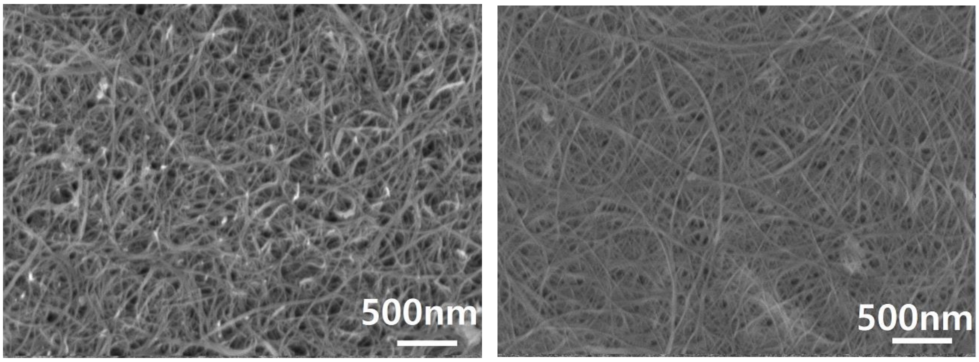

(e) (f)

**Figure 3-19** SEM images of SWNT/MWNT hybrid coated on PET film. Ratio of SWNT/(MWNT+SWNT) are (a) 0%, (b) 5%, (c) 10%, (d) 20%, (e) 30% and (f) 100%.

Figure 3-20 shows the resistivity and electrical conductivity of the coated films. Resistivity is obtained by multiplying measured sheet resistance and thickness of the film. Electrical conductivity is the inverse of resistivity. The results show that electrical conductivity increases as ratio of SWNT in the hybrid increases. Figure 3-21 shows comparison of the experimental results and the calculated results. The electrical conductivity at 0% SWNT ratio is normalized to 1. The calculated results in Figure 3-21 are obtained using provided SWNT and MWNT diameters. Blue line in the middle are conductivity calculated using average diameter of SWNT and MWNT. Minimum possible electrical conductivities are calculated with maximum diameter of SWNT and minimum diameter of MWNT. Maximum possible electrical conductivities are calculated with minimum diameter of SWNT and maximum diameter of MWNT. As shown in this figure, the normalized electrical conductivity from the experimental results are in the predicted range.

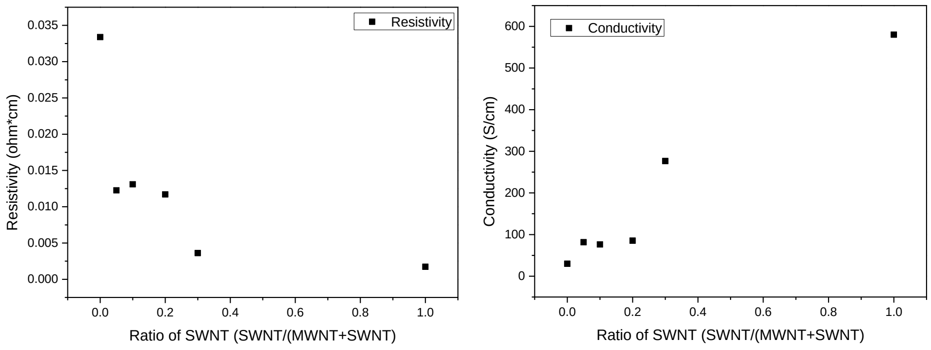

(a) (b)

**Figure 3-20** (a) Resistivity and (b) electrical conductivity of the SWNT/MWNT hybrid at different SWNT/(MWNT+SWNT) ratios.

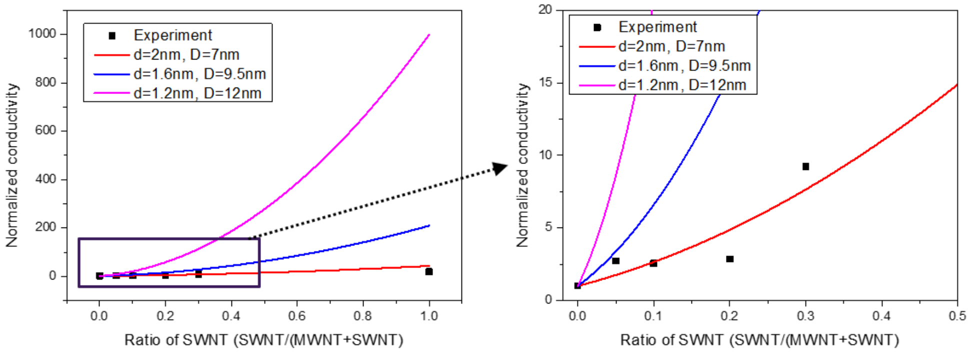

**Figure 3-21** Electrical conductivity of SWNT/MWNT hybrids at different SWNT ratios. Experimental results and calculated results are compared. The electrical conductivity (total number of contacts) at SWNT ratio of 0% is normalized to 1. Red line shows calculated results using maximum diameter of SWNT and minimum diameter of MWNT. Pink line shows calculated result using minimum diameter of SWNT and maximum diameter of MWNT. Blue line shows calculated result using average diameters of SWNT and MWNT.

## 3.6. Summary

The number of CNT-to-CNT, graphene-to-graphene, and graphene-to-CNT interparticle contacts was calculated using an orientation density function of graphene and CNT in a hybrid assembly. CNTs and graphene particles were assumed to be straight cylinders and disks, respectively. The probability of each type of contact was then calculated, from which the number of contacts was obtained. The total number of contacts followed a parabolic equation as a function of CNT concentration, suggesting the existence of a maximum at a specific composition ratio. This indicates a synergistic effect of the properties of the CNT/graphene hybrids, in particular those properties that are contact-dependent. This synergistic effect was experimentally investigated by using inkjet printing to prepare CNT/graphene hybrids. Hybrid inks, prepared at a certain composition ratio, had higher electrical conductivities than those of pure CNT or graphene, i.e., a synergistic effect. We have also found out that this calculation approach can be applied to SWNT/MWNT hybrid which has different length and diameters. These findings support the use of our statistical approach to investigate the properties of particulate hybrid materials involving contacts of the constituent elements.

# Chapter 4. piezoresistive behavior of CNT composites

## 4.1. Introduction

Residual stress forms during the fabrication of an adhesive joint via chemical contraction of the adhesive during curing [142]. Previous studies have shown that the failure strength of an adhesive joint increases with decreasing residual stress [142, 143]. If the residual stress is reduced via stress relaxation, then the failure strength of the adhesive joint can increase [143]. Therefore, in situ monitoring of adhesive stress relaxation is important. Residual stress can be measured using methods such as hole drilling, indentation, X-ray diffraction, and micro-Raman spectroscopy [142, 144, 145]. However, these methods are difficult to use in practical applications, especially when real-time measurement of residual stress change is required.

Carbon nanotube (CNT) composites have been developed as strain sensors because of their piezoresistive properties [18-21, 44, 45, 56, 146-148]. They can be used for real-time measurement of residual stress, because the resistance change of a CNT composite reflects stress relaxation behavior [58-61, 149, 150]. The tunneling effect, which refers to electron hopping through an insulating polymer matrix between CNTs, is the main mechanism underlying the electrical conductivity of CNT composites [52]. Resistance change during deformation can be explained by changes in tunneling resistance. Studies have established that changes in the distance between CNTs due to deformation of the composite affects the overall resistance thereof [50, 52, 54, 151, 152]. However, the mechanism of resistance change during stress relaxation is unclear. It has been proposed that rearrangement of polymer chains during stress relaxation disrupts the conductive filler network, leading to a change in the tunneling distance between CNTs [61, 150].

Various models have been developed to calculate the total resistance of a CNT composite [153, 154]. However, the merging of multiple pathways formed between CNTs into one conducting path has not been considered in these models, where multiple pathways can form at high concentrations.

In this work, we found experimentally that the resistance-change behavior of a CNT composite during stress relaxation depends on the CNT aspect ratio and concentration We propose a new resistor model that shows conductivity of CNT composite which considers multiple pathways between CNTs. A change in tunneling resistance during stress relaxation was simulated, assuming that the orientation of CNTs changes during stress relaxation. The resistance change of the conducting path at various concentrations and aspect ratios was calculated using the developed model. The simulation results revealed the dependence of resistance change on the CNT aspect ratio and concentration during stress relaxation and tensile testing.

## 4.2. Experiment

### 4.2.1. Materials and specimen

Epoxy resin (YD128; Kukdo Chemical), hardener (G-A0432; Kukdo Chemical), and multiwalled carbon nanotubes (MWNTs) with two different aspect ratios were used for the experiments. Long CNTs (MR99; Carbon Nano-material Technology) with a length of 10 μm and diameter of 10 nm (aspect ratio, ~1,000), and short CNTs (Applied Carbon Nano Technology) with a length of 1 μm and diameter of 20 nm (aspect ratio, ~50), were used.

The epoxy resin was mixed with CNTs using a planetary centrifugal mixer (ARE-310; THINKY) at 2,000 rpm for 1 h (Figure 4-1(a)). Then, the mixture was ultrasonicated for 60 min with a tip sonicator (VCX-750; Sonics & Materials) (Figure 4-1(b)). The pulse on/off time was 10 s/5 s, with 50% amplitude. After ultrasonication, the hardener was added to the resin at a resin:hardener ratio of 1:0.2. The combination was mixed at 2,000 rpm for 25 min and defoamed at 2,200 rpm for 5 min using the planetary centrifugal mixer. The mixture was cast into a dog-bone shaped mold and cured at 70°C for 3 h. Copper wires were attached to the sample for conductivity measurement. Figure 4-1(c) shows the dog bone specimen of the CNT composite.

(a) (b) (c)

**Figure 4-1** Pictures during dispersion process and the sample. (a) Planetary centrifugal mixer (b) Ultrasonication process using tip sonicator (c) Dog bone specimen of cured CNT composite.

CNT composite samples at different CNT concentrations were made. For CNT composite composed of high aspect ratio CNTs (~1000), concentration ranged from 0.1~0.6wt%. Concentration higher than 0.6wt% was not used due to difficulties during ultrasonication process. For CNT composite composed of low aspect ratio CNTs (~50), concentration ranged from 0.6~4wt%.

### 4.2.2. Characterization of CNT dispersion

Dispersion of CNT in the epoxy resin before curing was observed using optical microscopy. CNT dispersed epoxy resin was pressed between two cover glasses. Dispersion was measured at each dispersion step of the resin to see the effect of each step. In the optical microscope image, CNT agglomerates were found as dark spots.

The dispersion state of the resin can be estimated using the ratio of dark spots in the image. Dispersion of the CNT in the cured composite was observed using Scanning electron microscopy (SEM). Fractured surfaces of the CNT composites were observed. Dispersion of samples made with different CNT aspect ratio and concentrations were observed.

### 4.2.3. Resistance measurement during mechanical tests

Tests were performed using a tensile testing machine (Instron 5967; Instron). Tensile tests were done at a constant strain rate of 0.005/s until failure. Stress relaxation tests were carried out over 5 min at a strain of 0.008. Resistance of the sample during the test was measured via attached copper wires using a Keithley 6517B resistance meter (Tektronix).. Figure 4-2 shows the picture during the mechanical tests. Tests were done with CNT composites of various concentrations.

**Figure 4-2** Picture of tensile test and stress relaxation test setting. Resistance was measured with Keithley Resistance Meter through copper wire during the test.

## 4.3. Experimental results

### 4.3.1. Dispersion of CNTs in the epoxy resin

Dispersion of CNT in the epoxy resin before curing was observed by using optical microscopy. Optical images of CNT dispersion in epoxy resin are shown in Figure 4-3 and 4-4. Aspect ratio of CNTs in Figure 4-3 and 4-4 are 1000 and 50 respectively. The dark spots in the images are agglomerates of CNTs. These images show changes in dispersion state of CNTs in the resin during the dispersion processes. Area of the dark spots divided by the total area of the images will show how well the CNTs are dispersed. Area of dark spots decreases as sonication time increases. All CNT dispersed samples showed good dispersion after 60 minutes of sonication. Figure 4-4 (d) shows that when low aspect ratio(~50) CNTs are used, CNTs are well dispersed even at high concentration(1.2wt%).

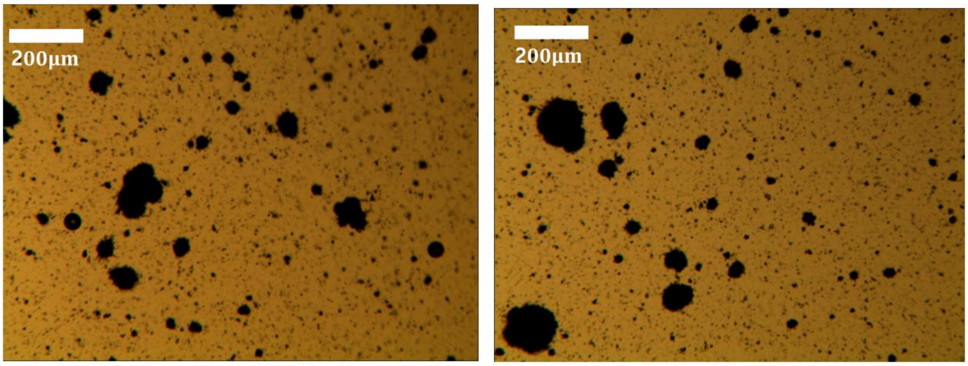

(a) (b)

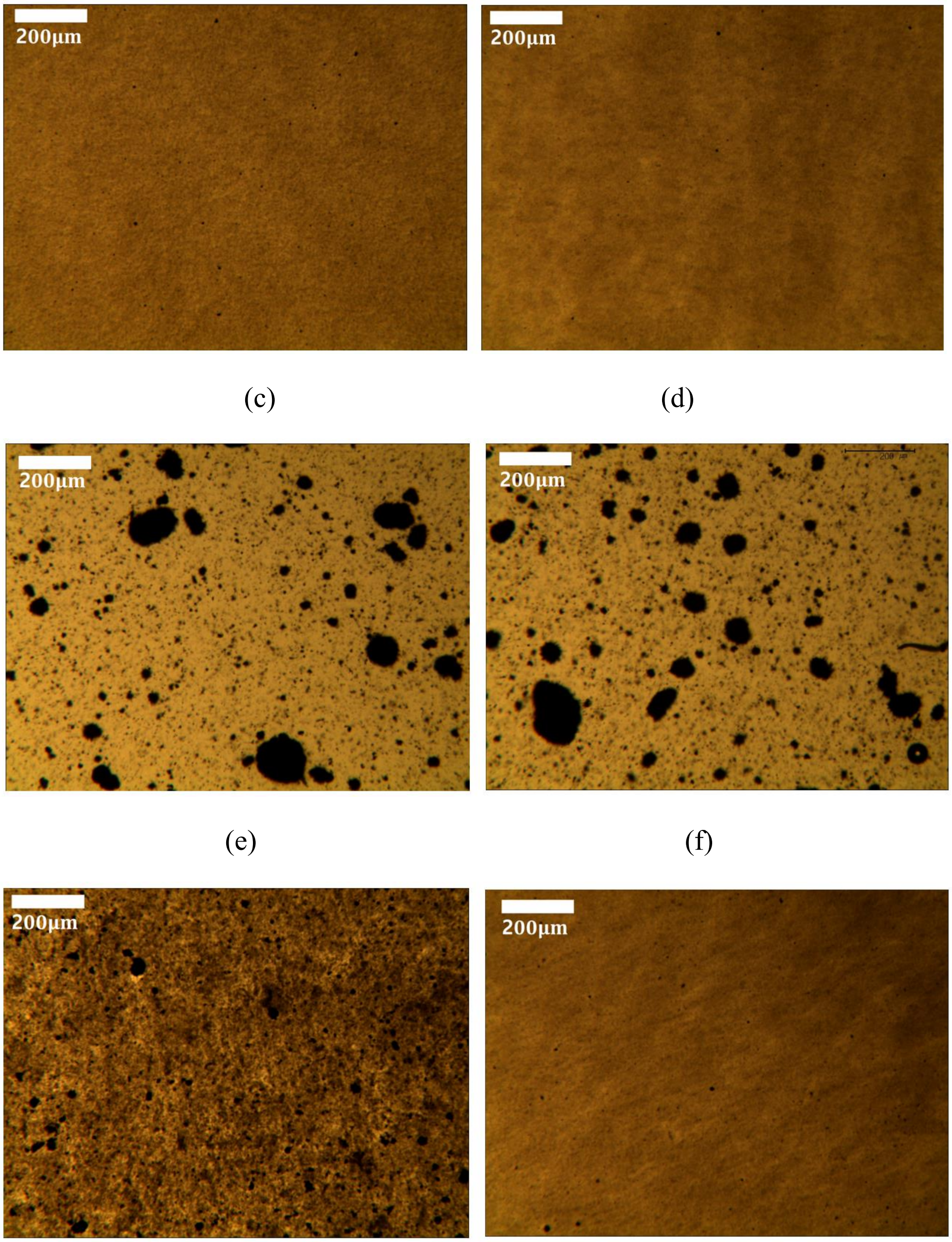

(c) (d)

(e) (f)

(g) (h)

**Figure 4-3** Optical images of CNT dispersion in epoxy resin. Aspect ratio of CNTs are 1000. (a)~(d) are images of 0.3wt% CNT dispersion. (a) 30min mixed. (b) 60min mixed. (c) 60min mixed+30min sonicated. (d) 60min mixed+60min sonicated. (e)~(h) are images of 0.5wt% CNT dispersion. (e) 30min mixed. (f) 60min mixed.

(g) 60min mixed+30min sonicated. (h) 60min mixed+60min sonicated.

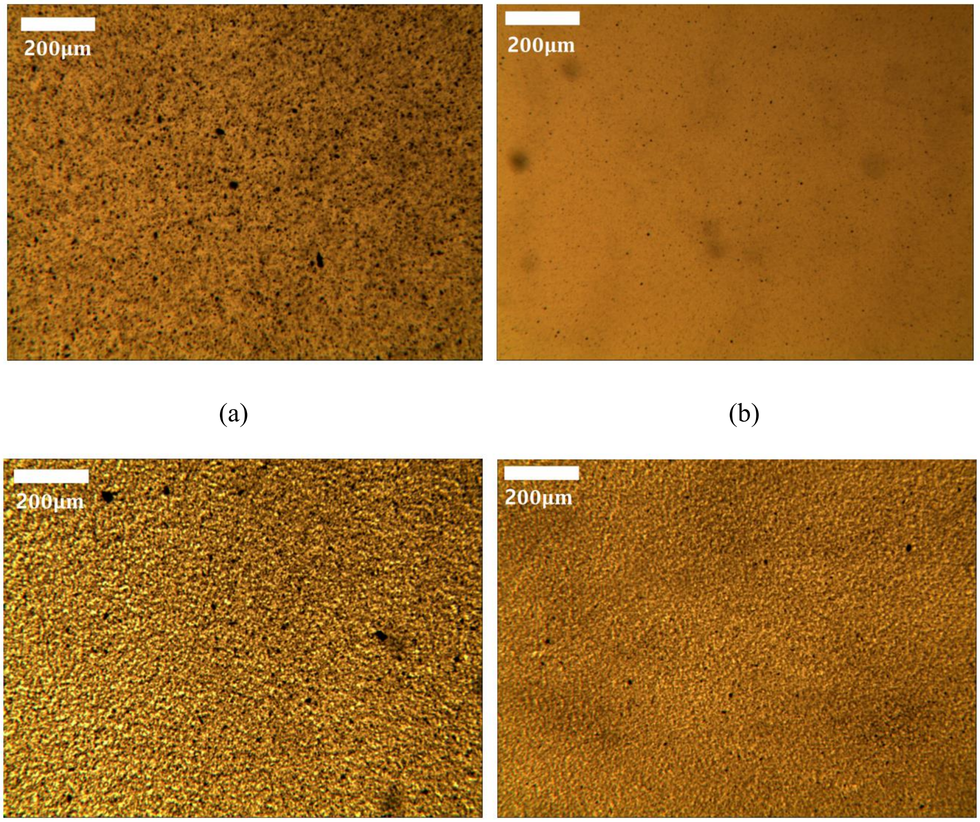

(a) (b)

(c) (d)

**Figure 4-4** Optical images of CNT dispersion in epoxy resin. Aspect ratio of CNTs are 50. (a) and (b) are images of 0.24wt% CNT dispersion. (a) 60min mixed. (b) 60min mixed+60min sonicated. (c)~(d) are images of 1.2wt% CNT dispersion. (c) 60min mixed. (d) 60min mixed+60min sonicated.

To see the dispersion state of the CNT in the cured CNT composites, scanning electron microscopy (SEM) was used. Figure 4-5 shows SEM images of fractured surfaces of CNT composites at different concentration and aspect ratios. Figure 4-5 (a)~(c) and (d)~(f) shows CNT composites with CNT aspect ratio of 1000 and 50 respectively. Figure 4-5 (a)~(c) shows that CNT of aspect ratio of 1000 are well dispersed in the composites with concentration of 0.2~0.6wt%. Figure 4-5 (d)~(f) shows that CNT of lower aspect ratio (~50) are also well dispersed in the composites with concentration of 0.6~1.5wt%. From the optical images and SEM images, it can be concluded that CNTs are well dispersed in the tested CNT concentration range.

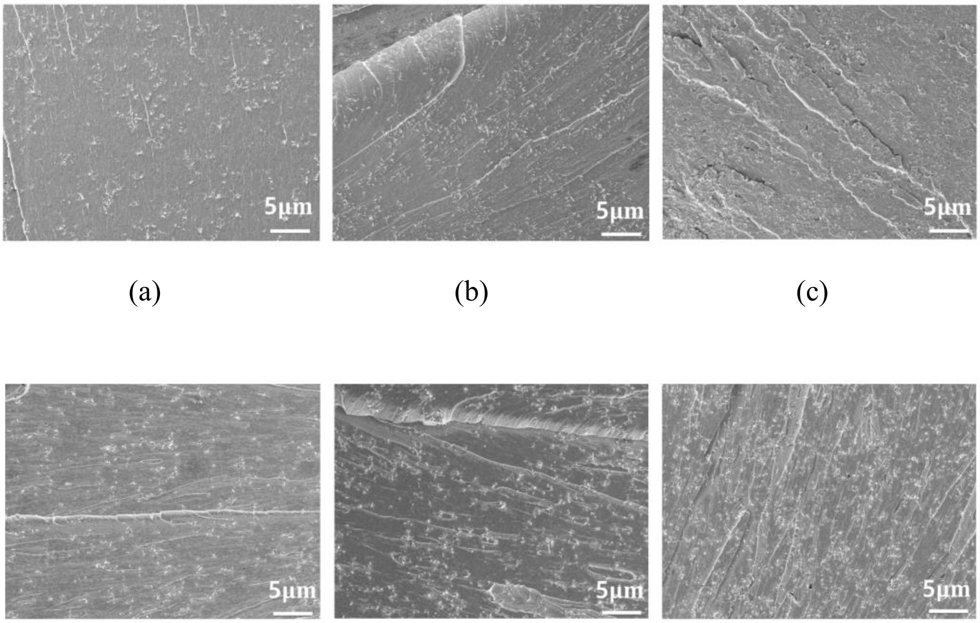

(a) (b) (c)

(e) (f) (g)

**Figure 4-5** SEM images of fractured surfaces of CNT composites. Aspect ratio of CNTs in (a)~(c) are 1000. (a) 0.2wt% (b) 0.4wt% (c) 0.6wt% Aspect ratio of CNTs in (d)~(f) are 50. (d) 0.6wt% (e) 1wt% (f) 1.5wt%

### 4.3.2. Electrical conductivity of the CNT composites

Figure 4-6 shows electrical conductivity of the fabricated CNT composite samples.

In this figure, electrical conductivity and CNT concentrations are in logarithmic scale. Both CNT composite composed of high aspect ratio CNTs (~1000) and low aspect ratio CNTs (~50) showed higher electrical conductivity at higher CNT concentrations. CNT composite composed of high aspect ratio CNT (~1000) showed much higher electrical conductivity even at lower concentrations. Percolation threshold of high aspect ratio CNT (~1000) is lower than 0.1wt%. In case of composite composed of low aspect ratio CNTs (~50), the Keithley Resistance Meter wasn't able to measure resistance of CNT composite at concentration of 0.4wt% due to very high resistance. Therefore, the percolation threshold is assumed to be between 0.4 and 0.6wt% in case of low aspect ratio CNTs.

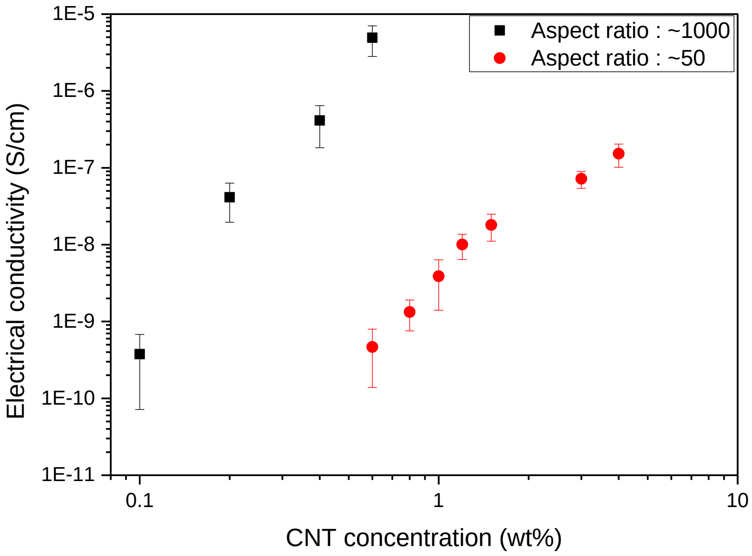

**Figure 4-6** Electrical conductivity of the CNT composites at different concentrations.

### 4.3.3. Resistance change during stress relaxation test

Resistance was measured during stress relaxation test of CNT composites. CNT composites at various concentration and CNT aspect ratio were tested. The change in the resistance right after deformation ($\Delta R_0$) and during stress relaxation ($\Delta R(t)$) were measured. Resistance right after deformation was normalized to 1. Normalized resistance change was defined as $\Delta R(t)/\Delta R_0$ in this work. Normalized resistance change at different CNT concentration and CNT aspect ratios were compared.

Figure 4-7 (a, b) shows the resistance change during stress relaxation of CNT composites containing long(Aspect ratio~1000) or short CNTs(Aspect ratio~50) at a concentration of 0.6 wt%.. Resistance change of CNT composite composed of long CNTs showed similar behavior to the relaxation modulus change. However, resistance tended to increase in case of CNT composite composed of short CNTs.

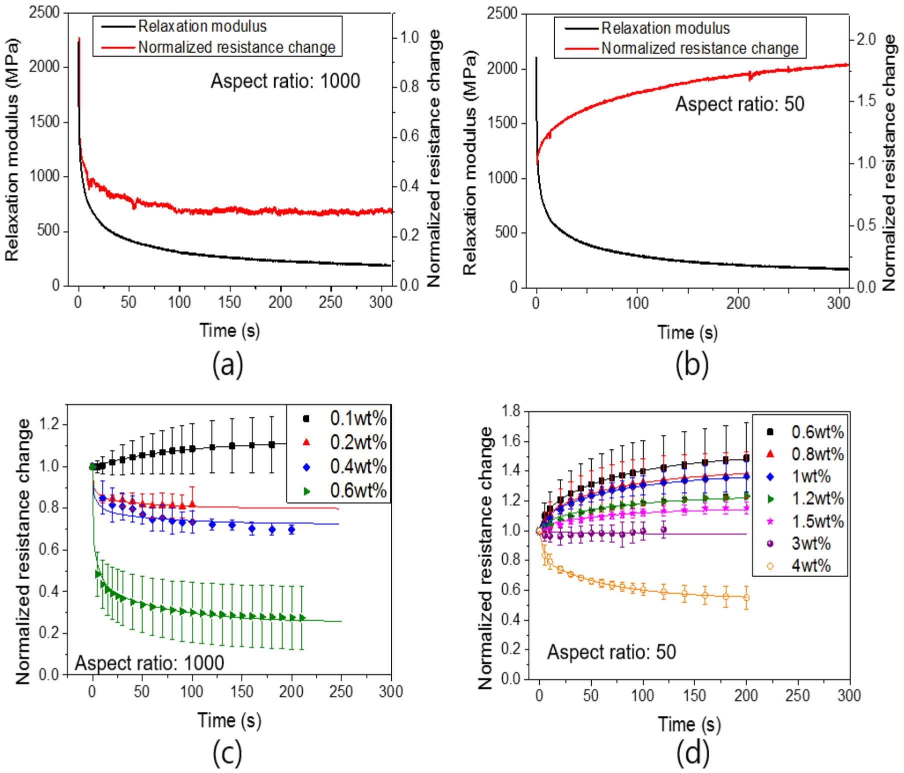

(a) (b)

(c) (d)

**Figure 4-7** (a, b) Changes in relaxation modulus and normalized resistance change $(\Delta R(t)/\Delta R_0)$ during stress relaxation of 0.6wt% CNT composite samples with CNT aspect ratio of 1000 and 50 respectively. (c, d) Resistance change during stress relaxation test of CNT composites at various CNT concentrations with CNT aspect ratio of 1000 and 50 respectively.

To see the overall trend of changes in resistance at different aspect ratio and concentration, we compared the resistance change of CNT composite composed of long CNT and short CNT at various concentrations. The results are shown in Figure 4-7(c, d). Figure 4-7(c) presents the resistance change of composites containing the long CNTs. It shows that the resistance tends to decrease during stress relaxation when CNT concentration is above 0.2wt%. Resistance tended to decrease more at higher concentration. At very low CNT concentration (0.1wt%), resistance tended to increase during stress relaxation. Figure 4-7(d) shows the resistance change of CNT composites composed of short CNTs. Resistance increased during stress relaxation at most of the tested CNT concentration range (0.6~1.5wt%). In this concentration range, resistance tended to increase more at lower CNT concentration. The CNT concentration should be much higher than CNT composite composed of long CNT in order for the resistance to decrease during stress relaxation. The resistance started to decrease when the concentration is above 3wt%. Both aspect ratio and CNT concentration affects the resistance changing behavior during stress relaxation.

To see the effect of viscoelasticity on the resistance changing behavior, resistance changing behavior during stress relaxation of CNT composite made with different resin:hardener ratios were compared. CNT composite composed of high aspect ratio CNTs (~1000) with 0.6wt% CNT concentration were used. Results using CNT composites with resin:hardener ratio of 1:0.4, 1:0.25 and 1:0.2 were compared. The results are shown in Figure 4-8. The dashed lines are normalized relaxation modulus. It shows that samples with lower hardener ratio shows more viscous behavior. ratio of hardener is lower. It also shows that normalized resistance change shows similar behavior to the stress relaxation behavior with different viscoelasticity. These results indicate that resistance change during stress relaxation is also dependent on the viscoelasticity of the polymer matrix.

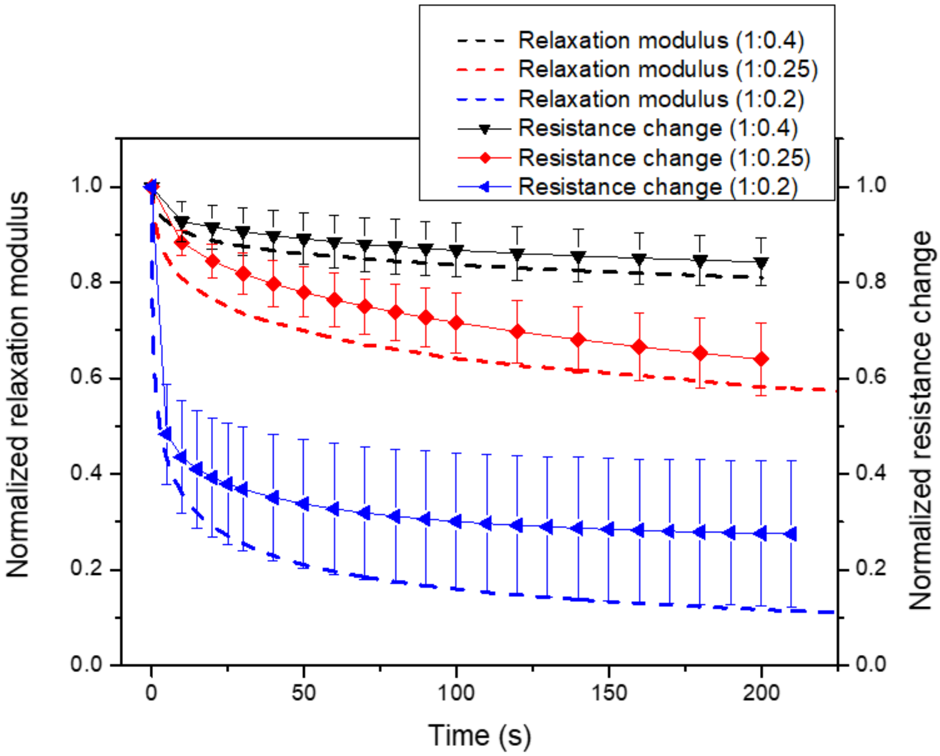

**Figure 4-8** Resistance change during stress relaxation test of CNT composite at 0.6wt% with CNT aspect ratio of 1000. Results of specimen made with different resin:hardener ratios (1:0.4, 1:0.25, 1:0.2) are shown.

### 4.3.4. Resistance change during tensile test

Resistance change during tensile test of CNT composites at different concentrations was also measured. Figure 4-9 shows resistance change during tensile test of CNT composites composed of high aspect ratio CNTs (~1000). It shows that resistance tends to increase as strain increases. At high concentration as in Figure 4-9 (b), resistance starts to decrease after certain strain level. This behavior is also shown in other researches [44, 45, 56]. Meeuw et al. [44] stated that the reason for the decrease in the resistance after certain strain level is the tunnel gap decrease. They said that the transverse displacement of the CNT, local plastic and viscoelastic deformation due to stress peaks formed by CNT particles, and the entanglement of CNTs in the polymer causes decrease in the tunnel gap. However, these are just assumptions and there are no proof to backup these mechanisms.

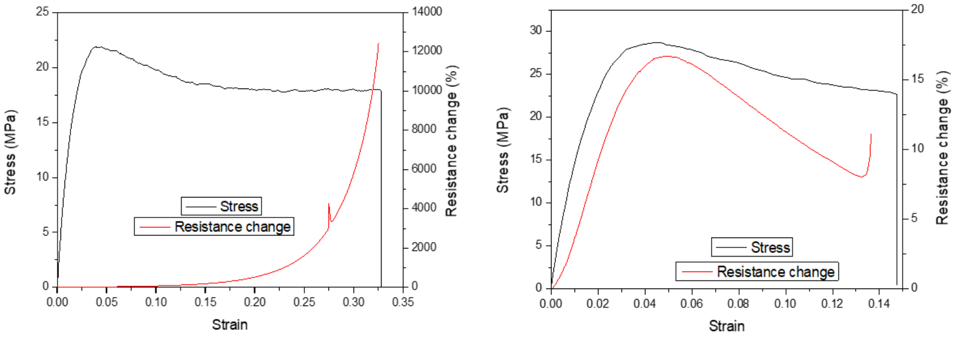

(a) (b)

**Figure 4-9** Tensile test results of CNT composites composed of high aspect ratio CNTs (~1000). Resistance change during tensile tests were also shown. (a) 0.2wt%, (b) 0.6wt%

Figure 4-10 shows the resistance change during tensile test of CNT composites composed of low aspect ratio CNTs (~50). It shows that the resistance tends to increase as strain increases at all strain levels in the tested CNT concentration range. During tensile test of CNT composite composed of low aspect ratio CNTs at 1.5wt%, the resistance increasing rate decreases after certain strain level (Figure 4-10 (b).

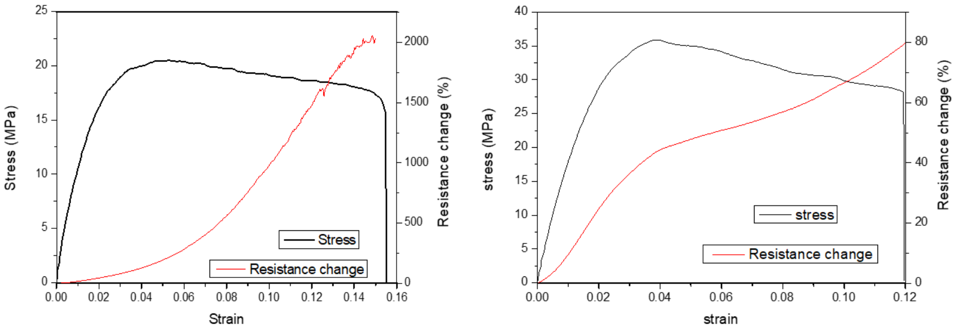

(a) (b)

**Figure 4-10** Tensile test results of CNT composites composed of low aspect ratio CNTs (~50). Resistance change during tensile tests were also shown. (a) 0.6wt% (b) 1.5wt%

Figure 4-11 shows overall resistance change during tensile tests at different CNT concentrations. It shows that resistance change is smaller at larger concentration at both CNT aspect ratios. When low aspect ratio CNT is used, resistance change is much larger than CNT composite composed of high aspect ratio CNTs at same concentrations. The resistance changing behavior at different CNT aspect ratios and concentrations is explained using calculation result using resistor model in section 4.4.

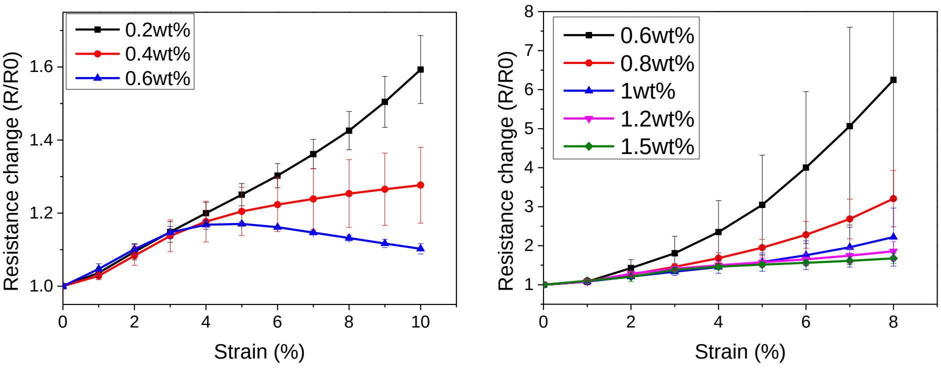

(a) (b)

**Figure 4-11** Resistance change during tensile test at various CNT concentrations. (a) CNT aspect ratio ~1000 (b) CNT aspect ratio ~50

## 4.4. Model

### 4.4.1. Resistor model

To explain this resistance changing behavior, we made a resistor model that can calculate the resistance of CNT composite as in Figure 4-12. Conductivity of a multi walled CNT is about $5 \times 10^3 \sim 5 \times 10^6 S/m$ while tunneling resistance is about $10^7 \sim 10^{18} \Omega$ [155]. Since the resistance of a CNT is much lower than the tunneling resistance between CNTs, the resistance of CNT is neglected. Each conducting path in Figure 4-12(a) can be expressed as series of resistor model in Figure 4-12(c). Number of paths (np) will increase when more CNTs are connected between two CNTs A and B as in Figure 4-12(b), therefore, more parallel resistor components will be added. Calculation of number of contacts between CNTs is necessary in this model.

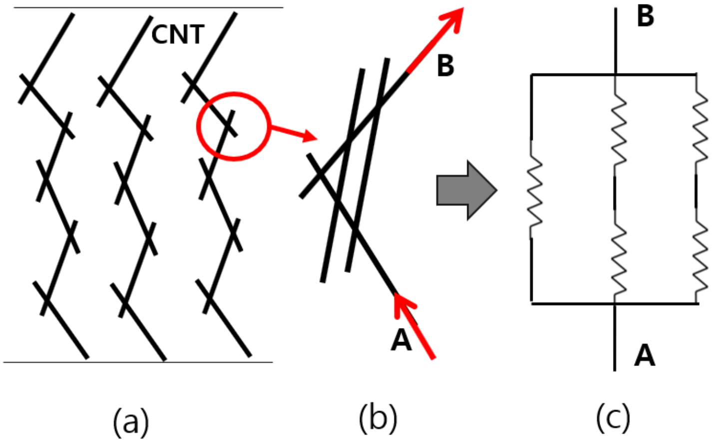

**Figure 4-12** Resistor model that shows the resistance of a conducting path in CNT composite.

### 4.4.2. Number of contacts between CNTs

Estimation of number of contacts between CNTs can be done by using method proposed by Komori and Makishima [137]. We assumed the CNTs to be straight and cylindrical. Assuming CNTs are oriented and distributed randomly in the composite, the average number of contacts on an arbitrary CNT having random orientation can be expressed as:

$$\overline{n_c} = \pi D L^2 N / 2V, \qquad (99)$$

where $L$, $D$, $V$ and $N$ are length of CNT, diameter of CNT, total volume of composite and total number of CNTs respectively [137]. From this, probability that a CNT contacts arbitrary CNT in the randomly oriented CNT composite can be obtained as:

$$p = \pi D L^2 / 2V. \qquad (100)$$

Proportion of CNTs having number of contacts of $x$ can be expressed as:

$$\frac{N!}{(N-x)!x!}(1-p)^{N-x}p^x. \qquad (101)$$

Number of CNTs in the composite ($N$) can be calculated using total volume of CNT composite, volume of one CNT and volume fraction of CNT ($\Phi$) as:

$$N = 4V\Phi / \pi D^2 L. \qquad (102)$$

Epoxy resin density of $1.17\mathrm{g/cm^3}$ were provided by the manufacturer (Kukdo

Chemical). MWNT density of $2.0\mathrm{g/cm^3}$ from literature was used [156]. Volume fraction of CNT was estimated using the density of epoxy resin and CNT. Distribution of contact numbers in arbitrary CNT are shown in Figure 4-13. The results show that the number of contacts is larger when higher aspect ratio CNT is used at same concentration. As shown in Figure 4-13(a) and(d), distribution of number of contacts are the same when the concentration of short CNT is 20 times larger than that of long CNT, which is the ratio of the aspect ratio of them.

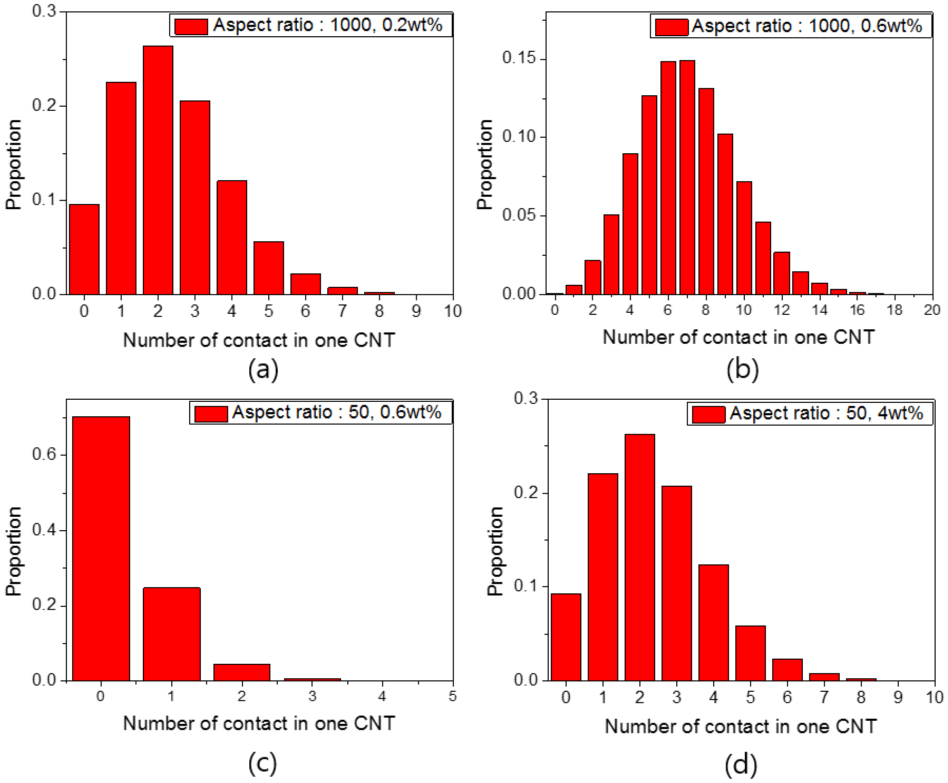

(a) (b)

(c) (d)

**Figure 4-13** Distribution of number of contacts in one CNT. (a) Aspect ratio: 1000, 0.2wt% (0.12vol%), (b) Aspect ratio: 1000, 0.6wt% (0.35vol%), (c) Aspect ratio: 50, 0.6wt% (0.35vol%), (d) Aspect ratio: 50, 4wt% (2.4vol%)

### 4.4.3. Calculation of tunneling resistance change

The followings are the procedure for calculating changes in distance between CNTs during deformation and stress relaxation using MATLAB. CNT A is generated at first. Then CNT B was generated randomly near CNT A so that the shortest distance between them to be 1nm. The generated CNTs should have random orientation. CNTs were generated with the polar and azimuthal angles as:

$$\theta = arcsin(1 - 2rand) + \pi/2, \qquad (103)$$

$$\varphi = rand \times \pi, \qquad (104)$$

where rand is random number generator between 0 and 1. After generating two CNTs, the effect of strain (z direction) was applied to the CNTs. The center of CNT $(x, y, z)$ was changed to $(x(1+\varepsilon)^{-\nu}, y(1+\varepsilon)^{-\nu}, z(1+\varepsilon))$ after deformation, where $\nu$ is the Poisson's ratio of the polymer matrix.

The polar angle $\theta$ also changes after deformation. Followings are procedure to calculate polar angle after deformation. Figure 4-14 shows polar angle and coordinates of CNT in a composite before and after deformation. Center of CNTs are set to (0,0,0) and CNTs are assumed to be aligned parallel to y=0 plane. The length of CNT $l$ remains unchanged after deformation. Coordinates of end of CNT $(x, 0, z)$ becomes $(x', 0, z')$ where $x = l/2 \sin\theta$, $z = l/2 \cos\theta$, $x' = x(1 +$

$\varepsilon)^{-\nu}$ and $z' = z(1+\varepsilon)$. $\tan\theta$ is x/z and $\tan\theta'$ is x′/z′. Using the above relationship, $\tan\theta'$ can be expressed as in Equation (105).

$$\tan\theta' = \frac{x'}{z'} = \tan\theta\,(1+\varepsilon)^{-(1+\nu)} \qquad (105)$$

The polar angle after deformation can be calculated using Equation (105). Only polar angle changes and the azimuthal angle remains unchanged when the tensile deformation is in z direction. The orientation of CNTs changes from $(\theta, \varphi)$ to $(arctan((1+\varepsilon)^{-(1+\nu)}tan\theta), \varphi)$.

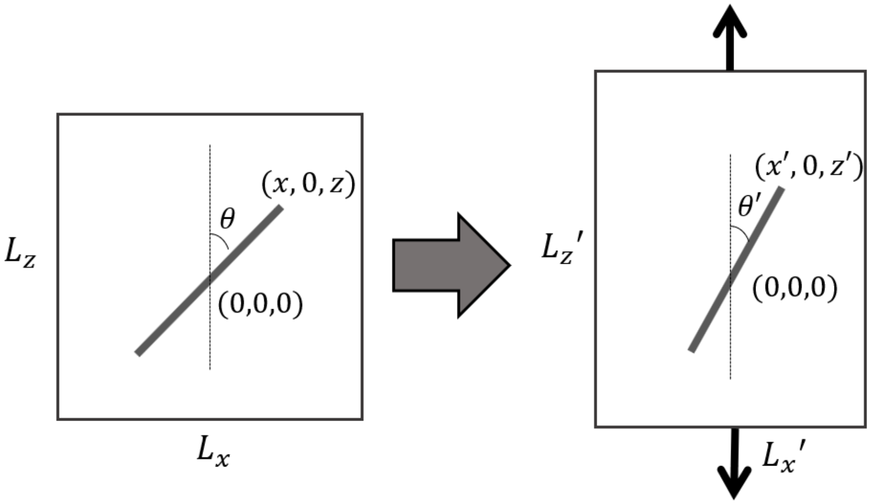

(a) (b)

**Figure 4-14** CNT in a composite (a) before deformation and (b) after deformation. CNTs are aligned parallel to y=0 plane. Center of CNT is set to (0,0,0)

During stress relaxation, polymer matrix will make the CNT to move [61, 150]. However, since the strain of the composite remains constant, we assumed the CNTs to rotate during stress relaxation while center location of CNTs remain unchanged. Azimuthal angles are unchanged while polar angles change from $arctan((1+\varepsilon)^{-(1+\nu)}tan\theta)$ to $arctan((1+(1+k)\varepsilon)^{-(1+\nu)}tan\theta)$. The parameter $k$ indicates the ratio of additional rotation. Orientation changes as if strain $(1+k)\varepsilon$ is applied additionally. If the value of $k$ is 0, it means there is no additional rotation after strain $\varepsilon$ is applied. $k$ values ranging from 0 to 0.03 was used in this calculation.

The simulation was repeated 5000 times. The changes in shortest distance between two CNTs were measured. Figure 4-15 shows tunneling distance after deformation (k=0) and after additional rotation (k=0.002, 0.005) plotted against angle between tensile direction vector and shortest distance vector between two CNTs. Figure 4-15 (a) and (b) shows tunneling distance distribution after deformation and additional rotation when the aspect ratio of CNT is 1000. It is shown in these figures that additional rotation of CNT causes the distance between CNTs to either increase or decrease. As the amount of additional rotation increases, the amount of changes in tunneling distance increases. Figure 4-15 (c) and (d) shows tunneling distance distribution when the aspect ratio of CNT is 50. This also shows that additional rotation of CNT causes the distance between CNT increases but not as much as when the aspect ratio of CNT is 1000.

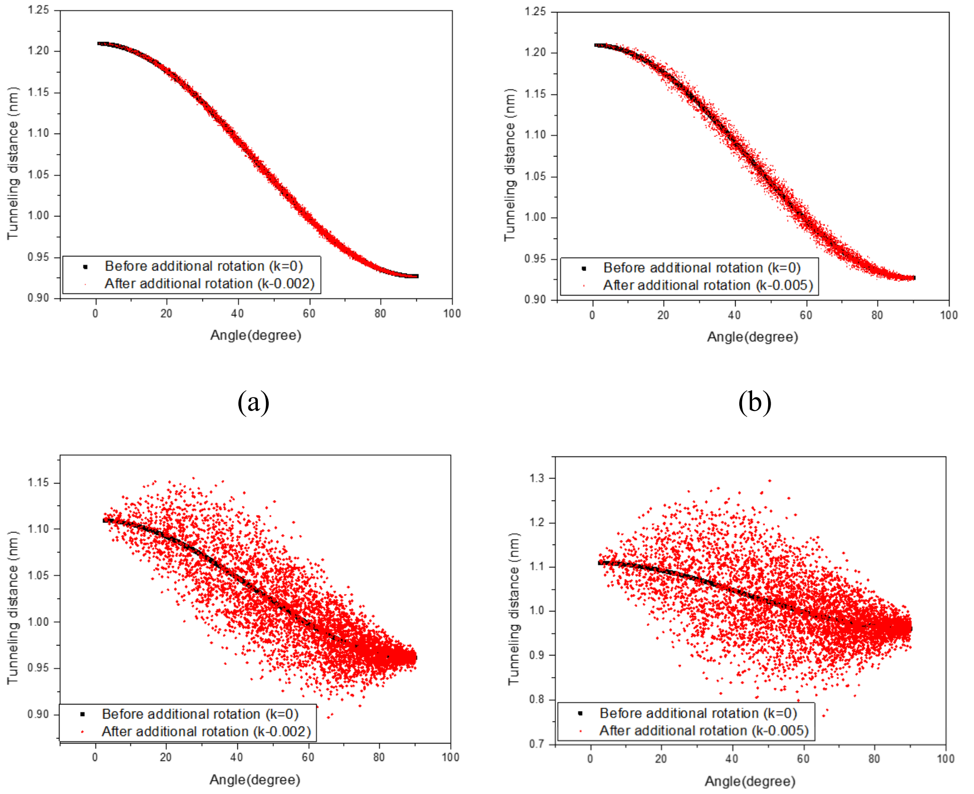

(a) (b)

(c) (d)

**Figure 4-15** Tunneling distance after deformation (k=0) and after additional rotation (k=0.002, 0.005) plotted against angle between tensile direction vector and shortest distance vector between two CNTs. (a,b) Tunneling distance distribution when the aspect ratio of CNT is 1000. (c,d) Tunneling distance distribution when the aspect ratio of CNT is 50.

Tunneling resistance between two CNTs was calculated using equation (106):

$$R_{tunnel} = \frac{h^2 d}{Ae^2\sqrt{2m\Psi}} \exp\left(\frac{4\pi\sqrt{2m\Psi}}{h} d\right) \qquad (106)$$

where $h$, $\Psi$, $A$, $m$ and $d$ are Planck's constant, work function of CNT, contact area, mass of electron and distance between two CNTs respectively. 5eV is used for

$\Psi$ [157]. Contact area $A$ is assumed to be $D^2$, where $D$ is the diameter of a CNT.

### 4.4.4. Effect of aspect ratio and concentration on resistance change

Average resistance change of the conducting path is calculated using the tunneling resistance results from the simulation in section 4.4.3 and the model in Figure 4-12(c). The resistance change after additional rotation of the CNTs are plotted in Figure 4-16. The plotted resistance change is $R/R_0$, where $R$ is resistance after rotation of CNT and $R_0$ is initial resistance before deformation. It shows that resistance tend to increase during additional rotation of CNTs when the number of paths (np) between two CNTs in the conducting path is smaller. Since the number of contacts is larger for higher aspect ratio CNTs and at higher concentration as in Figure 4-13, this result can explain the different behavior at different aspect ratio and concentration observed in the experimental result in Figure 4-7. Estimation of aspect ratio and concentration of CNT where the resistance changing behavior changes from increasing trend to decreasing trend is possible using this approach.

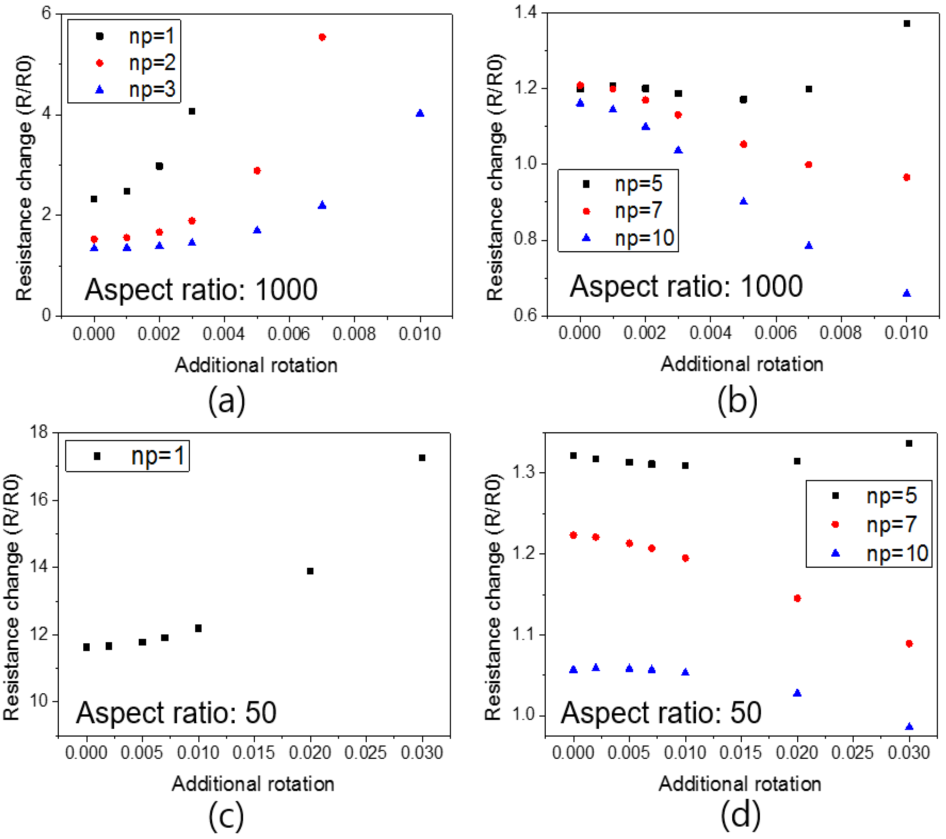

**Figure 4-16** Resistance change as additional rotation of CNT occurs after deformation. Additional rotation indicates value of $(1 + k)$. (a,b) Aspect ratio: 1000, (c,d) Aspect ratio: 50

Resistance change during tensile test can also be calculated using this approach. Figure 4-17 shows experimental and simulation results of resistance change during tensile test of CNT composites. Experimental results show that resistance change is more sensitive at lower CNT concentrations and when lower aspect ratio CNT is used. Experimental result of CNT composite composed of long CNTs at higher CNT concentration also shows resistance decreasing behavior after certain strain level is reached. These behaviors are shown in the simulated results. However, in case of short CNT, concentration should be 20 times higher than composite composed of long CNT in order to show resistance decreasing behavior after certain strain level. Due to dispersion difficulties at high concentration, short CNT at high concentration was not tested.

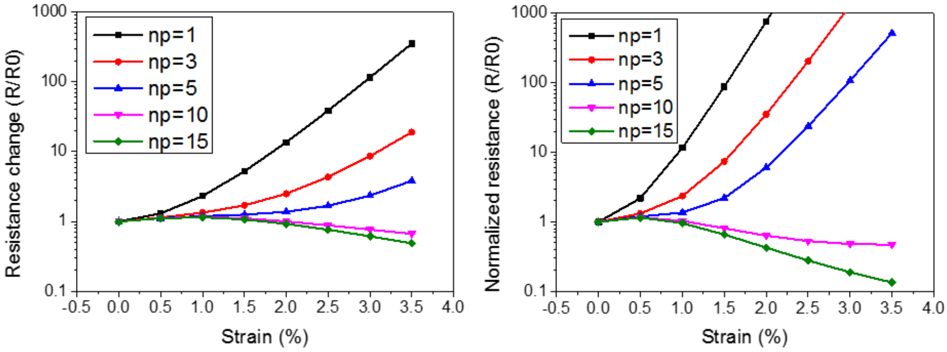

(a) (b)

**Figure 4-17** (a,b) Simulated results of resistance change of CNT composite during tensile test at various concentrations with CNT aspect ratio of 1000 and 50 respectively.

## 4.5. Application in residual stress measurement

### 4.5.1. Experimental procedure

Measurement of residual stress in the adhesive joint is important because the residual stress affects the failure strength of the adhesive joint [142]. Different curing cycle or cooling can cause residual stress to occur in the adhesive joint. Residual stress cannot be measured using strain sensors. However, if CNT composite is used as an adhesive, residual stress and its reduction due to stress relaxation can be measured.

For the experiment, adhesive joint was made with CNT composite as an adhesive. GFRP plate with 1mm thickness was used as an adherend. CNT with aspect ratio of 1000 was dispersed in the epoxy resin with concentration of 0.72wt%. The resin was mixed with hardener with the resin:hardener ratio of 1:0.25. Figure 4-18 shows how CNT composite adhesive joint was made. The thickness of the CNT composite adhesive was controlled with GFRP plate attached on the side of the adherend. GFRP plates were attached using instant adhesive (Loctite 401, Henkel). Copper wire was attached on the adherends for resistance measurement purposes. After applying uncured resin on the GFRP plate, it was covered with another GFRP plate and cured on the hot plate at 70°C. After the CNT composite was cured it was cooled to 24°C. The resistance was measured during cooling. The temperature change during cooling which is measured using thermocouple, is shown in Figure 4-19.

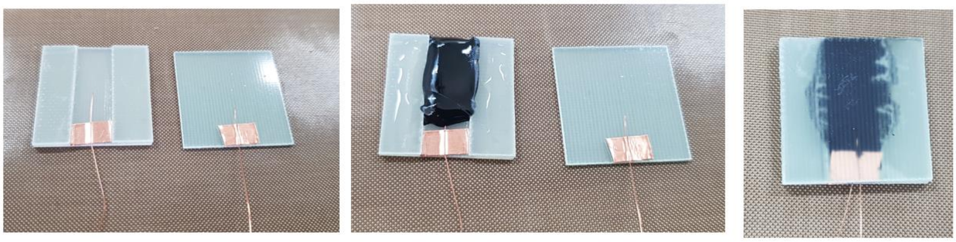

(a) (b) (c)

**Figure 4-18** Preparation of CNT composite adhesive joint

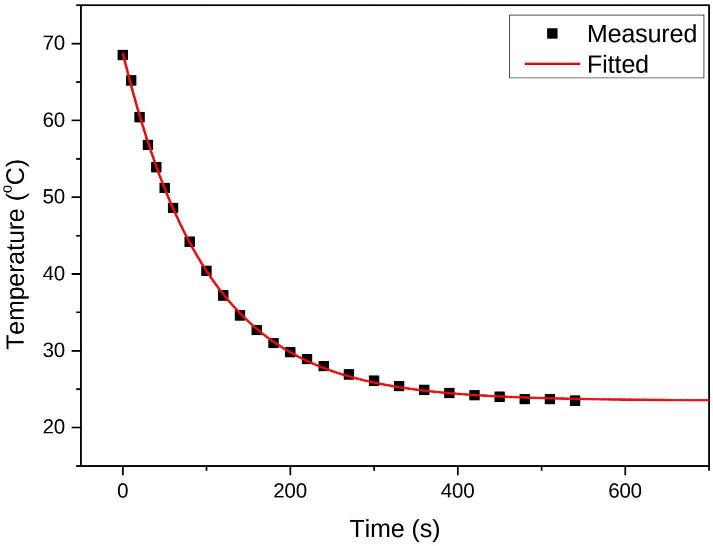

**Figure 4-19** Changes in the temperature measured during cooling of the CNT composite adhesive joint.

Temperature dependence of the resistance of the CNT composite used in the adhesive joint was also measured. The CNT composite was made into rectangular shape. The width, thickness and length of the composite is 4.5mm, 1.25mm, 10mm respectively. Figure 4-20 shows how it was measured. The temperature of the CNT composite was controlled by putting it on the hot plate. Resistance was measured at different temperatures.

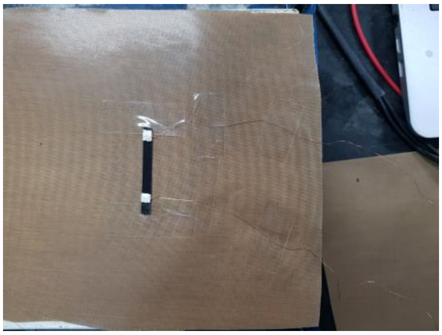

**Figure 4-20** Resistance measurement of CNT composite at different temperature on the hot plate.

Material properties of CNT composite (adhesive) and GFRP plate (adherend) are needed for numerical simulation of the adhesive joint during cooling. Material properties needed in the simulation are the viscoelastic property of CNT composite, elastic modulus of GFRP plate, thermal expansion coefficient of CNT composite and the GFRP plate. Viscoelastic property of CNT composite at different temperature was measured by dynamic mechanical analysis (DMA) test (Temperature range: 10~80°C, Frequency range: 0.1~100/s). Elastic modulus of GFRP plate (50GPa) was obtained from the literature [158]. Thermal expansion coefficients of CNT composite and GFRP plate are measured using DMA and TMA respectively.

### 4.5.2. Experimental results

#### 4.5.2.1. Resistance change of adhesive joint during cooling

Temperature dependence of electrical resistance of CNT composite was measured. No other forces were acting on the composite during this measurement. The results are on Figure 4-21. The result shows that electrical resistance tends to decrease when the temperature increases. The temperature dependence of the resistivity value was fitted in linear equation as:

$$\rho = 1.28 \times 10^5 - 780T\ (\Omega \cdot \mathrm{cm}) \qquad (107)$$

where temperature $T$ is in degrees Celsius. The reason for the electrical conductivity increase as temperature increases is found in other researches [159, 160]. The electrical conductivity of CNT decreases when temperature increases. However, in CNT/polymer composites, the electrical conductivity is determined by the tunneling between CNTs. The temperature dependence of the electrical conductivity of CNT composite is explained with thermal fluctuation induced tunneling. Potential barrier height varies due to temperature fluctuations at higher temperature, leading to lower tunneling resistance.

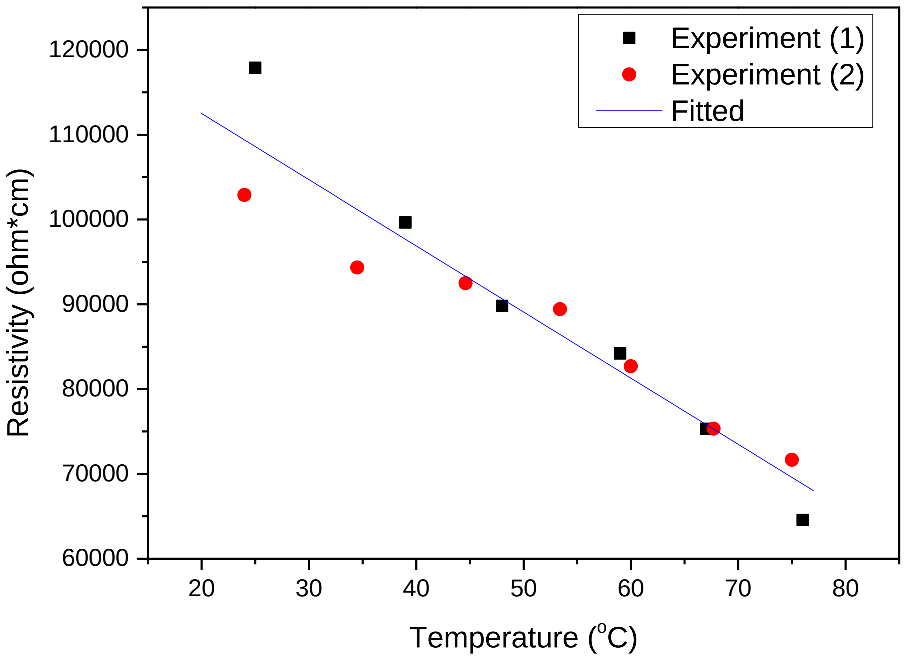

**Figure 4-21** Resistivity of CNT composite at different temperatures.

Electrical resistance of CNT composite adhesive joint during cooling from 70°C to 24°C was measured. The cooling condition is shown in section 4.5.1 and Figure 4-19. The measured resistance change during the experiment is shown in Figure 4-22. The plotted resistance change is the measured resistance (R) divided by the resistance before cooling (R0). It shows the resistance increases very fast due to fast temperature changing rate. Then the resistance increasing rate decreases as temperature starts to change slowly. From the measured temperature profile in Figure 4-19 and the relationship of resistivity and temperature in Equation (107), effect of temperature on the resistance change were calculated. The temperature effect on the resistance change was plotted in Figure 4-22 as red line. Effect of residual stress on the resistance can be calculated by excluding the temperature effect from the total resistance change. From the result, it is possible to know how the residual stress changed during the test. Changes in residual stress (normal stress) will have similar trend as the blue line in Figure 4-22. Residual stress increases during cooling since the thickness of the adhesive is fixed at 1mm while the CNT composite adhesive tends to shrink due to decreased temperature. After the temperature became stable, residual stress remained almost constant.

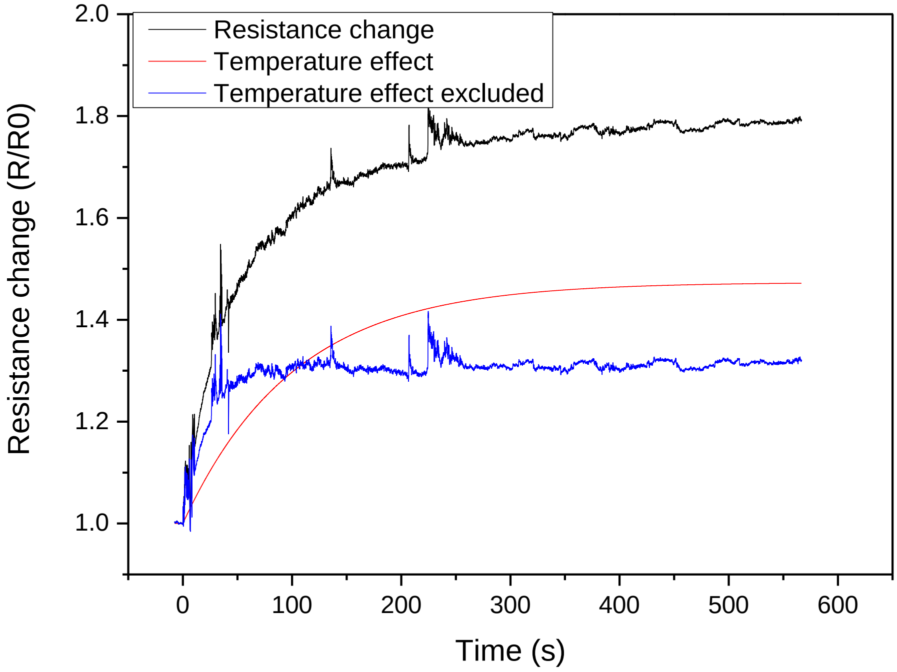

**Figure 4-22** Resistance change measured during cooling of CNT composite adhesive joint (black line). The temperature effect on the resistance change (red line) and the effect of residual stress on the resistance change (blue line) were also plotted.

### 4.5.2.2. Material property measured for numerical simulation

The followings are material parameters obtained from experiment for numerical simulation of the adhesive joint during cooling. Viscoelastic property of CNT composite was measured by DMA test. Figure 4-23 (a) shows master curve of DMA test results obtained by using time-temperature superposition. This master curve was fitted using Prony series. Figure 4-23 (b) shows shift factor which is obtained during time-temperature superposition of storage modulus. Shift factor was fitted as Equation (108) and (109).

$$\log(a_T) = -0.26(T - 273) + 4.68 \quad (\text{T<51.7°C}) \qquad (108)$$

$$\log(a_T) = -0.13(T - 273) - 2.01 \quad (\text{T<51.7°C}) \qquad (109)$$

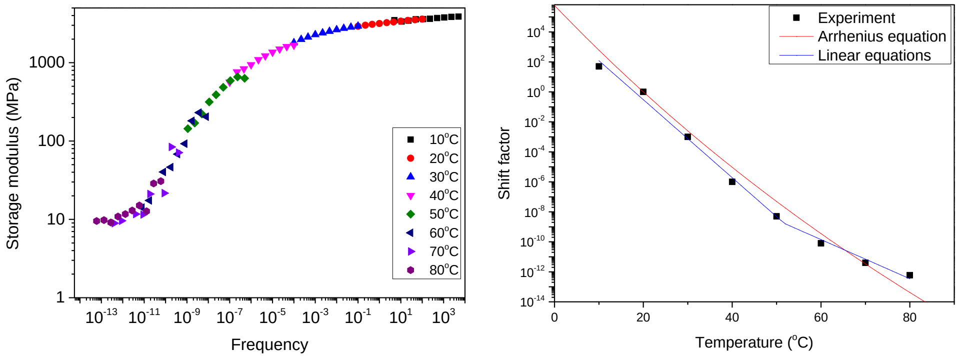

(a) (b)

**Figure 4-23** DMA test results (a) Master curve of storage modulus obtained using time-temperature superposition (b) Shift factor

Figure 4-24 shows linear thermal expansion of GFRP plate and CNT composite. They were measured using TMA and DMA test respectively. The results show that thermal expansion of CNT composite is much larger than GFRP plate. These results are used in the simulation.

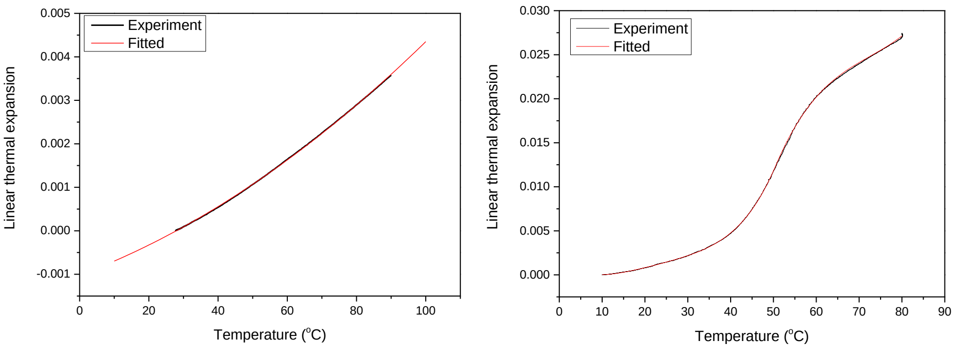

(a) (b)

**Figure 4-24** Linear thermal expansion of (a) GFRP plate and (b) CNT composite.

### 4.5.3. Simulation result of residual stress in the adhesive joint

ABAQUS was used for the numerical simulation of the CNT composite adhesive joint during cooling. Figure 4-25 (a) shows the geometry and boundary conditions of the simulated model. 3D stress element (C3D8R) was used. The geometry of the model is the same as the specimen used in the experiment (adherend length, width: 25mm; adherend thickness: 1mm; adhesive width: 5mm; adhesive length: 19mm; adhesive thickness: 1mm). Temperature of the adhesive and the adherend is assumed to change equally. Figure 4-25 (b) shows the input temperature condition, which is obtained from the measured result during experiment in Figure 4-19.

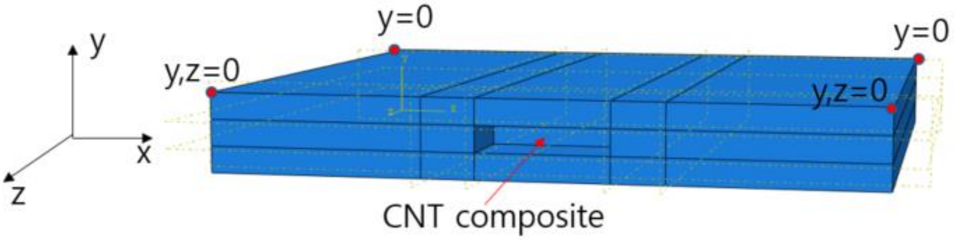

(a)

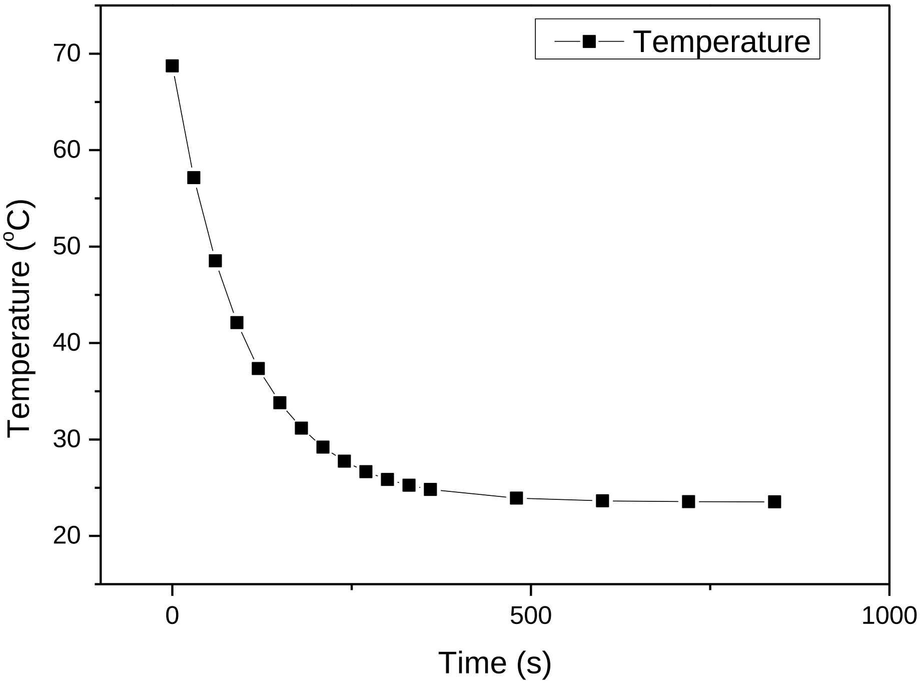

(b)

**Figure 4-25** (a) Geometry of the simulated model. (b) Input temperature condition which is obtained from measured data.

Figure 4-26 shows the normal stress formed at the adhesive from the simulation result. Stresses increases at first due to cooling, and then stress remains nearly constant as temperature becomes stable. Decrease in the stress (stress relaxation) after cooling didn't occur in the simulation. Stress relaxation occurs much faster at higher temperature (see Figure 4-23). Slow cooling rate made most of the relaxation to occur before the temperature becomes stable. The resistance changing trend with temperature effect exclude, from the experiment (Figure 4-22), and the normal stress change from the simulation (Figure 4-26) are similar. This shows that changes in the residual stress can be measured from the resistance change. This result suggests that CNT composite has potential for residual stress measurement when used as an adhesive.

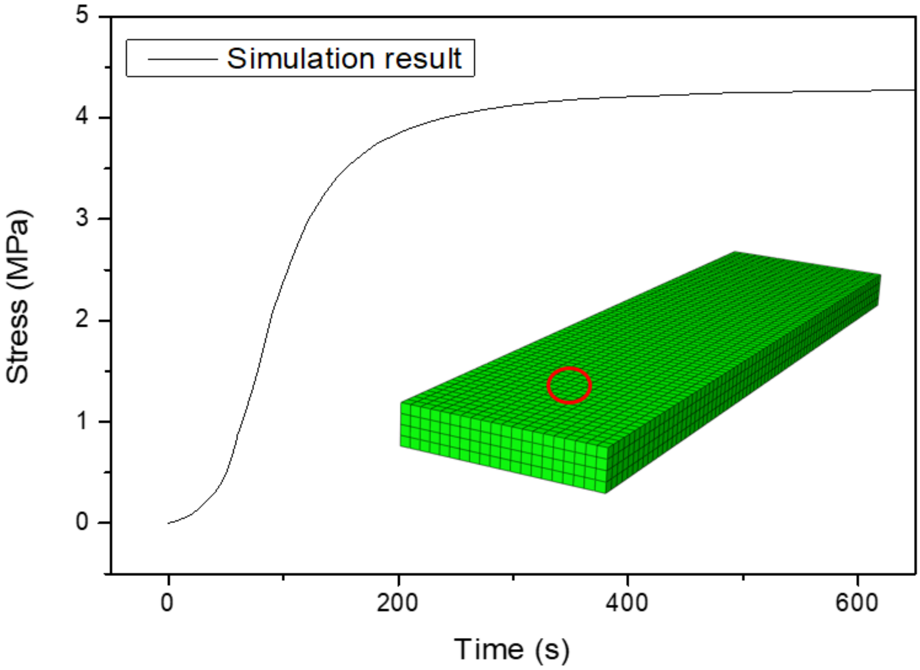

**Figure 4-26** Simulation results of normal stress at the adhesive formed during cooling. The figure inside the graph is the adhesive part and shows where the normal stress was measured.

To clearly see the effect of temperature and cooling rates on the residual stress formation and its relaxation behavior, more simulations at different conditions were done. Simulation results in Figure 4-27 show the effect of temperature on the stress relaxation behavior. When cooled to 24°C, the stress relaxation behavior after cooling is not observed. However, when cooled to 50°C, stress relaxation behavior is clearly shown after cooling. This is because stress relaxation occurs faster at higher temperature. Simulation results in Figure 4-28 show the effect of cooling rate on the stress relaxation behavior. The temperatures were cooled from 70°C to 50°C and then the temperature remained constant. Cooling rates of 0.02°C/s and 0.2°C/s were used in this simulation. The simulation results show that when the cooling rate is faster, after cooling is done, the amount of relaxed stress is larger. This proves that stress relaxation also occurs during cooling and the amount of stress relaxation will be smaller when cooled slower.

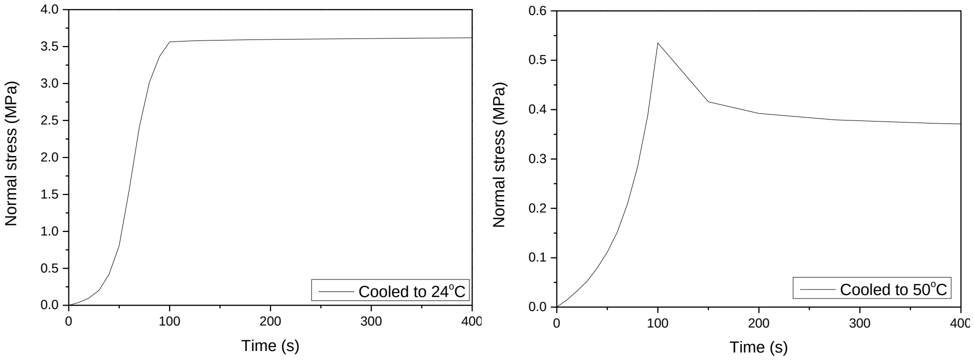

(a) (b)

**Figure 4-27** Simulation results of normal stress at the adhesive formed during two different cooling conditions. (a) Cooled from 70 °C to 24 °C for 100s and temperature remained constant after cooling. (b) Cooled from 70°C to 50°C for 100s and temperature remained constant after cooling.

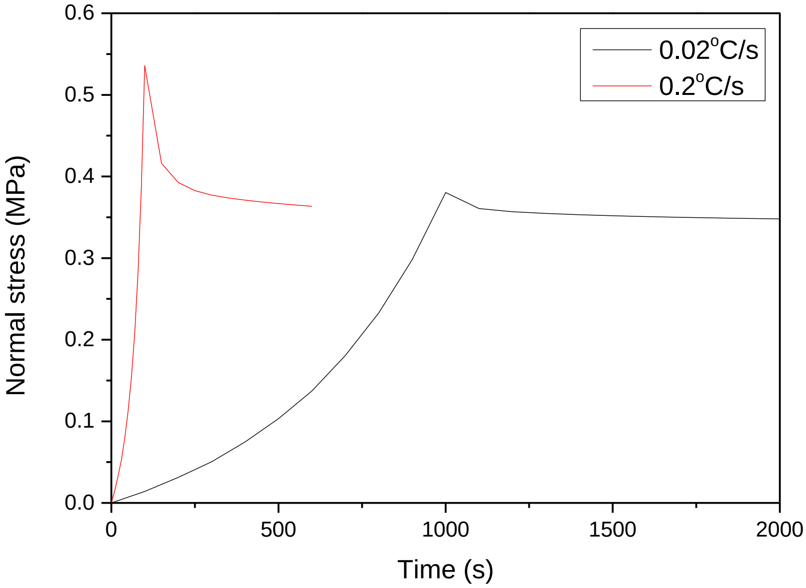

**Figure 4-28** Simulation results of normal stress at the adhesive formed during two different cooling conditions. Both were cooled from 70 °C to 50 °C and the temperature remained constant after cooling is done. The cooling rates are 0.02°C/s and 0.2°C/s each.

From the fact that stress relaxation also occurs during cooling and faster at higher temperature, it can be concluded that residual stress can be reduced by changing the cooling rate. Figure 4-29 shows simulation results of normal stress formed at different cooling rates. Temperature was cooled from 70°C to 24°C with cooling rates of 0.046°C/s, 0.092°C/s and 0.46°C/s each. Temperature remained constant after cooling. Figure 4-29 shows that slower cooling results in lower residual stress in the adhesive.

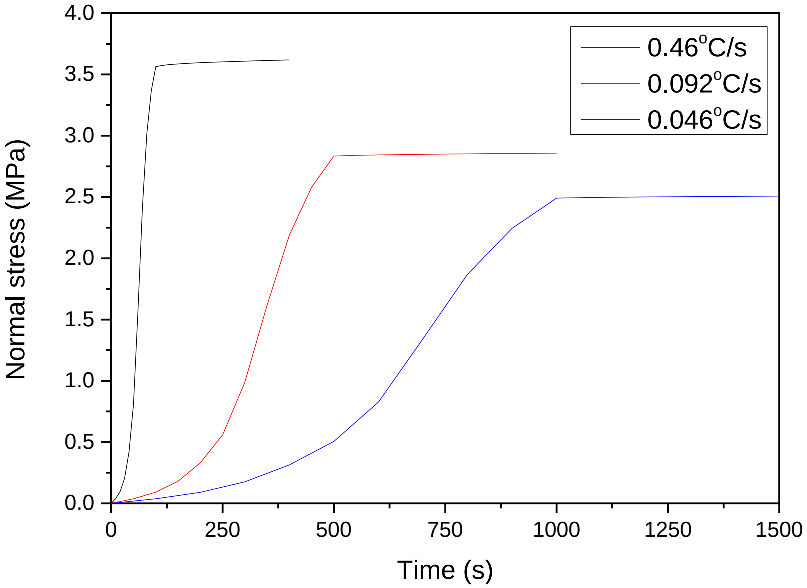

**Figure 4-29** Simulation results of normal stress at the adhesive formed during three different cooling conditions. Temperature was cooled from 70°C to 24°C and the temperature remained constant after cooling is done. The cooling rates are 0.046°C/s, 0.092°C/s and 0.46°C/s each.

## 4.6. Summary

In summary, we have experimentally found that resistance change behavior during stress relaxation of CNT/polymer composite is strongly dependent on the aspect ratio and concentration of CNTs. To investigate the detailed mechanism, we have developed a simulation model relying on a resistor model and the number of contacts between CNTs within the tunneling distance. Calculation of the resistance change of CNT/polymer composite during their stress relaxation reveals that the number of contacts between CNT at low concentration is not enough to form multiple conducting pathways, thus resulting in the increased resistance as the relaxation proceeded. This trend changes as the CNT concentration increases due to the increased number of contacts between CNTs. The developed model has been also validated to analyze the aspect ratio and concentration dependence of the resistance change during tensile test. CNT composite is also used as an adhesive and the resistance change during cooling of the adhesive joint was measured. It was compared with the numerical simulation results using ABAQUS and showed similar results to the resistance change from the experimental result. This suggests that CNT composite can be used as an adhesive that can detect the residual stress change.

# Chapter 5. Conclusion

The purpose of this study was to model the electrical resistance change during the stress relaxation of CNT/polymer composites. A model to calculate electrical conductivity of CNT/graphene hybrids was proposed. Using this model and the new resistor model we have proposed, the resistance change of CNT/polymer composites during stress relaxation can be explained. A method to numerically simulate nonlinear viscoelastic behavior of CNT/polymer composites was also developed to correlate the mechanical behavior and the resistance change.

A nonlinear viscoelastic model was used to describe the mechanical behavior of adhesives. Schapery's model was chosen as the nonlinear viscoelastic model. A procedure for implementing Schapery's model with strain-dependent parameters into a numerical simulation was derived. Reduced strain rate dependent failure criterion was used so that failure strain at different strain rate and temperature can be calculated. Implementation in the ABAQUS finite element software was done via a UMAT subroutine and the thermomechanical deformation behavior of the adhesive was simulated. Comparison of the simulation and experimental results showed that the nonlinear viscoelastic model was well-implemented into the finite-element software. The simulation results of lap shear testing at different strain rates and temperatures were in good agreement with the experimental data at every strain level. The results also demonstrated that the mechanical properties of the adhesive at very high strain rates, which are experimentally unobtainable, can be predicted with confidence using a nonlinear viscoelastic model

Predictive model that describes the synergistic effect of CNT and graphene in the electrical conductivity of the hybrid was proposed using statistical approach. Number of CNT-to-CNT, graphene-to-graphene and graphene-to-CNT contacts were calculated, and the sum of these numbers followed a parabolic equation as a function of CNT fractions, showing that there’s optimum point that shows maximum number of contacts at certain composition. Since electrical conductivity is proportional to the number of contacts between conductive particles, CNT/graphene hybrid film at certain composition is expected to show higher electrical conductivity than graphene film and CNT film. To validate this model, inkjet-printed CNT/graphene film was used. Films made with CNT/graphene hybrid inks at certain composition showed higher electrical conductivity than those made of pure CNT ink and graphene ink. The experimental results support the predictive model we have proposed.

The resistance change during stress relaxation of a CNT/polymer composite was strongly dependent on the CNT aspect ratio and concentration. To investigate the detailed mechanism, we developed a simulation model that was based on a new resistor model and the number of contacts between CNTs within tunneling distance. Calculation of the resistance change of a CNT/polymer composite during stress relaxation revealed that the number of contacts between CNTs at low concentration is insufficient to form multiple conducting pathways, thus resulting in increased resistance as relaxation progresses. This trend changes as the CNT concentration increases, due to the increased number of contacts between CNTs. The developed model was validated by the experimental CNT aspect ratio and concentration dependence of the resistance change seen during tensile testing.

Finally, CNT composite was used as an adhesive and the residual stress during cooling was measured by measuring the resistance change. The resistance change, which excluded the temperature effect, was proportional to the residual stress formed during cooling. Numerical simulation result using viscoelastic model showed similar result to the resistance change measured in experiment. This result suggest that CNT composite can be used in structural health monitoring of an adhesive which can also detect the residual stress change in the adhesive.

# Reference

1. Iijima, S., *Helical microtubules of graphitic carbon.* nature, 1991. **354**(6348): p. 56-58.
2. Iijima, S. and T. Ichihashi, *Single-shell carbon nanotubes of 1-nm diameter.* Nature, 1993. **363**: p. 603-605.
3. Zhang, M., et al., *Strong, Transparent, Multifunctional, Carbon Nanotube Sheets.* Science, 2005. **309**(5738): p. 1215-1219.
4. Wu, Z., et al., *Transparent, Conductive Carbon Nanotube Films.* Science, 2004. **305**(5688): p. 1273-1276.
5. Biercuk, M., et al., *Carbon nanotube composites for thermal management.* Applied physics letters, 2002. **80**(15): p. 2767-2769.
6. Graham, A., et al., *Towards the integration of carbon nanotubes in microelectronics.* Diamond and related materials, 2004. **13**(4-8): p. 1296-1300.
7. Yu, M.-F., et al., *Strength and breaking mechanism of multiwalled carbon nanotubes under tensile load.* Science, 2000. **287**(5453): p. 637-640.
8. Salvetat, J.-P., et al., *Mechanical properties of carbon nanotubes.* Applied Physics A, 1999. **69**(3): p. 255-260.
9. Pop, E., et al., *Thermal conductance of an individual single-wall carbon nanotube above room temperature.* Nano letters, 2006. **6**(1): p. 96-100.
10. Wilder, J.W., et al., *Electronic structure of atomically resolved carbon nanotubes.* Nature, 1998. **391**(6662): p. 59-62.
11. Rafique, I., et al., *Exploration of epoxy resins, hardening systems, and epoxy/carbon nanotube composite designed for high performance materials: a review.* Polymer-Plastics Technology and Engineering, 2016. **55**(3): p. 312-333.
12. Jeon, S.-Y., D. Kwon, and W.-R. Yu, *Tension-induced twist of twist-spun carbon nanotube yarns and its effect on their torsional behavior.* Scientific reports, 2018. **8**(1): p. 1-11.
13. Zhang, Q., et al., *Dry spinning yarns from vertically aligned carbon nanotube arrays produced by an improved floating catalyst chemical vapor deposition method.* Carbon, 2010. **48**(10): p. 2855-2861.

14. Cai, D., M. Song, and C. Xu, *Highly Conductive Carbon-Nanotube/Graphite-Oxide Hybrid Films.* Advanced Materials, 2008. **20**: p. 1706–1709.

15. Andrade, M.J., et al., *Electrical properties of transparent carbon nanotube networks prepared through different techniques* physica status solidi, 2007. **1**(5): p. 178-180.

16. Kwon, O., et al., *Fabrication and characterization of inkjet-printed carbon nanotube electrode patterns on paper.* Carbon, 2013. **58**: p. 116-127.

17. Li, C., et al., *Graphene Nano-"patches" on a Carbon Nanotube Network for Highly Transparent/Conductive Thin Film Applications.* Journal of Physical Chemistry C, 2010. **114**: p. 14008-14012.

18. Georgousis, G., et al., *Piezoresistivity of conductive polymer nanocomposites: Experiment and modeling.* Journal of Reinforced Plastics and Composites, 2018. **37**(17): p. 1085-1098.

19. Georgousis, G., et al., *Strain sensing in polymer/carbon nanotube composites by electrical resistance measurement.* Composites Part B: Engineering, 2015. **68**: p. 162-169.

20. Stuckey, J.P., et al., *Damage detection in epoxy embedded carbon nanotubes using electrical resistance and acoustic emission.* Journal of Nanomechanics and Micromechanics, 2017. **7**(3): p. 06017001.

21. Leopold, C., et al., *Influence of carbon nanoparticle modification on the mechanical and electrical properties of epoxy in small volumes.* Journal of colloid and interface science, 2017. **506**: p. 620-632.

22. Izadi-Najafabadi, A., et al., *Extracting the Full Potential of Single-Walled Carbon Nanotubes as Durable Supercapacitor Electrodes Operable at 4 V with High Power and Energy Density* Advanced Materials, 2010. **22**(35): p. E235-E241.

23. Fan, S., et al., *Self-Oriented Regular Arrays of Carbon Nanotubes and Their Field Emission Properties.* Science, 1999. **283**(5401): p. 512-514.

24. Kong, J., M.G. Chapline, and H. Dai, *Functionalized Carbon Nanotubes for Molecular Hydrogen Sensors.* Advanced Materials, 2001. **13**(18): p. 1384-1386.

25. Shim, W., et al., *Optimally conductive networks in randomly dispersed CNT: graphene hybrids.* Scientific reports, 2015. **5**: p. 16568.

26. Tung, V.C., et al., *Low-Temperature Solution Processing of Graphene-Carbon Nanotube Hybrid Materials for High-Performance Transparent Conductors.* Nano Letters, 2009. **9**(5): p. 1945-1955.

27. Yu, A., et al., *Enhanced Thermal Conductivity in a Hybrid Graphite Nanoplatelet-Carbon Nanotube Filler for Epoxy Composites.* Advanced Materials, 2008. **20**(24): p. 4740-4744.

28. Sun, H., et al., *Novel Graphene/Carbon Nanotube Composite Fibers for Efficient Wire-Shaped Miniature Energy Devices.* Advanced Materials, 2014. **26**(18): p. 2868-2873.

29. Cheng, H., et al., *Textile electrodes woven by carbon nanotube-graphene hybrid fibers for flexible electrochemical capacitors.* Nanoscale, 2013. **5**: p. 3428-3434.

30. Fan, Z., et al., *A Three-Dimensional Carbon Nanotube/Graphene Sandwich and Its Application as Electrode in Supercapacitors.* Advanced Materials, 2010. **22**(33): p. 3723-3728.

31. Peng, L., et al., *Transparent, Conductive, and Flexible Multiwalled Carbon Nanotube/Graphene Hybrid Electrodes with Two Three-Dimensional Microstructures.* Journal of Physical Chemistry C, 2012. **116**: p. 4970-4978.

32. Xin, G., et al., *A graphene sheet exfoliated with microwave irradiation and interlinked by carbon nanotubes for high-performance transparent flexible electrodes.* Nanotechnology, 2010. **21**(40): p. 405201.

33. King, P.J., et al., *Improvement of Transparent Conducting Nanotube Films by Addition of Small Quantities of Graphene.* ACS Nano, 2010. **4**(7): p. 4238-4246.

34. Hsiao, K.-T., J. Alms, and S.G. Advani, *Use of epoxy/multiwalled carbon nanotubes as adhesives to join graphite fibre reinforced polymer composites.* Nanotechnology, 2003. **14**(7): p. 791.

35. Song, Y.S. and J.R. Youn, *Influence of dispersion states of carbon nanotubes on physical properties of epoxy nanocomposites.* Carbon, 2005. **43**(7): p. 1378-1385.

36. Ayatollahi, M., et al., *Effect of multi-walled carbon nanotube aspect ratio on mechanical and electrical properties of epoxy-based nanocomposites.* Polymer Testing, 2011. **30**(5): p. 548-556.
37. Bai, J. and A. Allaoui, *Effect of the length and the aggregate size of MWNTs on the improvement efficiency of the mechanical and electrical properties of nanocomposites—experimental investigation.* Composites Part A: applied science and manufacturing, 2003. **34**(8): p. 689-694.
38. Sekitani, T., et al., *Stretchable active-matrix organic light-emitting diode display using printable elastic conductors.* Nature materials, 2009. **8**(6): p. 494-499.
39. Yu, C., et al., *Stretchable supercapacitors based on buckled single-walled carbon-nanotube macrofilms.* Advanced Materials, 2009. **21**(47): p. 4793-4797.
40. Kumar, S., M.A. Alam, and J.Y. Murthy, *Computational model for transport in nanotube-based composites with applications to flexible electronics.* 2007.
41. Kovacs, J.Z., et al., *Two percolation thresholds in carbon nanotube epoxy composites.* Composites Science and Technology, 2007. **67**(5): p. 922-928.
42. Kumar, V. and A. Rawal, *Tuning the electrical percolation threshold of polymer nanocomposites with rod-like nanofillers.* Polymer, 2016. **97**: p. 295-299.
43. Tarlton, T., et al., *The role of agglomeration in the conductivity of carbon nanotube composites near percolation.* Journal of applied physics, 2017. **121**(8): p. 085103.
44. Meeuw, H., et al., *Morphological influence of carbon nanofillers on the piezoresistive response of carbon nanoparticle/epoxy composites under mechanical load.* European Polymer Journal, 2016. **85**: p. 198-210.
45. Cao, X., et al., *Strain sensing behaviors of epoxy nanocomposites with carbon nanotubes under cyclic deformation.* Polymer, 2017. **112**: p. 1-9.
46. Spinelli, G., et al., *Experimental and theoretical study on piezoresistive properties of a structural resin reinforced with carbon nanotubes for strain sensing and damage monitoring.* Composites Part B: Engineering, 2018.

**145**: p. 90-99.

47. Yin, G., et al., *A carbon nanotube/polymer strain sensor with linear and anti-symmetric piezoresistivity.* Journal of composite materials, 2011. **45**(12): p. 1315-1323.

48. Kang, I., et al., *A carbon nanotube strain sensor for structural health monitoring.* Smart materials and structures, 2006. **15**(3): p. 737.

49. Pham, G.T., et al., *Processing and modeling of conductive thermoplastic/carbon nanotube films for strain sensing.* Composites Part B: Engineering, 2008. **39**(1): p. 209-216.

50. Tallman, T. and K. Wang, *An arbitrary strains carbon nanotube composite piezoresistivity model for finite element integration.* Applied Physics Letters, 2013. **102**(1): p. 011909.

51. Nirmalraj, P.N., et al., *Electrical Connectivity in Single-Walled Carbon Nanotube Networks.* Nano Letters, 2009. **9**(11): p. 3890-3895.

52. Rahman, R. and P. Servati, *Effects of inter-tube distance and alignment on tunnelling resistance and strain sensitivity of nanotube/polymer composite films.* Nanotechnology, 2012. **23**(5): p. 055703.

53. Kaiyan, H., et al., *A fabrication process to make CNT/EP composite strain sensors.* High Performance Polymers, 2018. **30**(2): p. 224-229.

54. Wang, Z. and X. Ye, *A numerical investigation on piezoresistive behaviour of carbon nanotube/polymer composites: mechanism and optimizing principle.* Nanotechnology, 2013. **24**(26): p. 265704.

55. Hu, N., et al., *Piezoresistive strain sensors made from carbon nanotubes based polymer nanocomposites.* Sensors, 2011. **11**(11): p. 10691-10723.

56. Wichmann, M.H., et al., *Piezoresistive response of epoxy composites with carbon nanoparticles under tensile load.* Physical Review B, 2009. **80**(24): p. 245437.

57. Oskouyi, A.B., U. Sundararaj, and P. Mertiny, *Tunneling conductivity and piezoresistivity of composites containing randomly dispersed conductive nano-platelets.* Materials, 2014. **7**(4): p. 2501-2521.

58. Liu, C.-X. and J.-W. Choi, *Analyzing resistance response of embedded PDMS and carbon nanotubes composite under tensile strain.*

Microelectronic engineering, 2014. **117**: p. 1-7.

59. Wang, L. and Y. Han, *Compressive relaxation of the stress and resistance for carbon nanotube filled silicone rubber composite.* Composites Part A: Applied Science and Manufacturing, 2013. **47**: p. 63-71.

60. Can-Ortiz, A., et al., *Electrophoretic deposition of carbon nanotubes onto glass fibers for self-sensing relaxation-induced piezoresistivity of monofilament composites.* Journal of materials science, 2019. **54**(3): p. 2205-2221.

61. Rizvi, R., et al., *Piezoresistance characterization of poly (dimethyl-siloxane) and poly (ethylene) carbon nanotube composites.* Smart materials and structures, 2011. **20**(9): p. 094003.

62. Rauh, A., R. Hinterhölzl, and K. Drechsler, *Application of the time-temperature superposition principle to the mechanical characterization of elastomeric adhesives for crash simulation purposes.* The European Physical Journal Special Topics, 2012. **206**(1): p. 15-24.

63. Banea, M., L.d. Silva, and R. Campilho, *Effect of temperature on tensile strength and mode I fracture toughness of a high temperature epoxy adhesive.* Journal of adhesion science and technology, 2012. **26**(7): p. 939-953.

64. Kim, J., et al., *Improved adhesion of metal–polymer sandwich composites using a spontaneous polymer grafting process.* Functional Composites and Structures, 2019.

65. Najib, M.F. and A.S. Nobari, *Nonlinear viscoelastic constitutive model identification for a polyurethane adhesive in a bonded joint using structural dynamic model updating.* Mechanics of Materials, 2016. **100**: p. 72-85.

66. Smith, T.L., *Dependence of the ultimate properties of a GR-S rubber on strain rate and temperature.* Journal of polymer science, 1958. **32**(124): p. 99-113.

67. Aubrey, D. and M. Sherriff, *Peel adhesion and viscoelasticity of rubber–resin blends.* Journal of Polymer Science: polymer chemistry edition, 1980. **18**(8): p. 2597-2608.

68. Kaelble, D., *Theory and analysis of peel adhesion: rate-temperature dependence of viscoelastic interlayers.* Journal of colloid science, 1964. **19**(5): p. 413-424.

69. Kin Loch, A. and S. Shaw, *The fracture resistance of a toughened epoxy adhesive.* The Journal of Adhesion, 1981. **12**(1): p. 59-77.

70. Kaelble, D., *Dynamic and tensile properties of epoxy resins.* Journal of Applied Polymer Science, 1965. **9**(4): p. 1213-1225.

71. Smith, T.L., *Deformation and failure of plastics and elastomers.* Polymer Engineering & Science, 1965. **5**(4): p. 270-279.

72. Miyagi, Z. and K. Yamamoto, *Viscoelastic analysis of shear adhesion test for pressure-sensitive adhesive tape.* The Journal of Adhesion, 1987. **21**(3-4): p. 243-250.

73. Majda, P. and J. Skrodzewicz, *A modified creep model of epoxy adhesive at ambient temperature.* International Journal of Adhesion and Adhesives, 2009. **29**(4): p. 396-404.

74. Costa, I. and J. Barros, *Tensile creep of a structural epoxy adhesive: Experimental and analytical characterization.* International Journal of Adhesion and Adhesives, 2015. **59**: p. 115-124.

75. Peretz, D. and Y. Weitsman, *Nonlinear Viscoelastic Characterization of FM-73 Adhesive.* Journal of rheology, 1982. **26**(3): p. 245-261.

76. Arzoumanidis, G.A. and K.M. Liechti, *Linear Viscoelastic Property Measurement and Its Significance for Some Nonlinear Viscoelasticity Models.* Mechanics of Time-Dependent Materials, 2003. **7**(3): p. 209-250.

77. Schapery, R.A., *On the characterization of nonlinear viscoelastic materials.* Polymer Engineering & Science, 1969. **9**(4): p. 295-310.

78. Schapery, R.A., *An engineering theory of nonlinear viscoelasticity with applications.* International Journal of Solids and Structures, 1966. **2**(3): p. 407-425.

79. Spathis, G. and E. Kontou, *Modeling of nonlinear viscoelasticity at large deformations.* Journal of Materials Science, 2008. **43**(6): p. 2046-2052.

80. Liu, Z. and L.E. Bilston, *Large deformation shear properties of liver tissue.* Biorheology, 2002. **39**(6): p. 735-742.

81. Govindjee, S. and S. Reese, *A presentation and comparison of two large deformation viscoelasticity models.* 1997.
82. Xu, Q. and B. Engquist, *A mathematical model for fitting and predicting relaxation modulus and simulating viscoelastic responses.* Proceedings of the Royal Society A: Mathematical, Physical and Engineering Sciences, 2018. **474**(2213): p. 20170540.
83. Marzi, S., A. Rauh, and R.M. Hinterhölzl, *Fracture mechanical investigations and cohesive zone failure modelling on automotive composites.* Composite Structures, 2014. **111**: p. 324-331.
84. Campilho, R.D., et al., *Modelling adhesive joints with cohesive zone models: effect of the cohesive law shape of the adhesive layer.* International Journal of Adhesion and Adhesives, 2013. **44**: p. 48-56.
85. Alfano, M., et al., *Mode I fracture of adhesive joints using tailored cohesive zone models.* International Journal of Fracture, 2008. **157**(1): p. 193.
86. Li, S., et al., *Mixed-mode cohesive-zone models for fracture of an adhesively bonded polymer–matrix composite.* Engineering Fracture Mechanics, 2006. **73**(1): p. 64-78.
87. May, M., et al., *Rate dependent behavior of crash-optimized adhesives–Experimental characterization, model development, and simulation.* Engineering Fracture Mechanics, 2015. **133**: p. 112-137.
88. Musto, M. and G. Alfano, *A fractional rate-dependent cohesive-zone model.* International Journal for Numerical Methods in Engineering, 2015. **103**(5): p. 313-341.
89. McCrum, N., C. Buckley, and C. Bucknall, *Principles of Polymer Engineering.* 2nd ed. 1997: Oxford University Press.
90. Schapery, R., *A Theory of Nonlinear Thermoviscoelasticity Based on Irreversible Thermodynamics.* Proceedings of the 5th U.S. National Congress on Applied mechanics, 1966. **511**: p. 511-530.
91. Pacheco, J.E.L., C.A. Bavastri, and J.T. Pereira, *Viscoelastic relaxation modulus characterization using Prony series.* Latin American Journal of Solids and Structures, 2015. **12**(2): p. 420-445.
92. Lai, J. and A. Bakker, *3-D Schapery representation for non-linear*

*viscoelasticity and finite element implementation.* Computational Mechanics, 1996. **18**(3): p. 182-191.

93. Sundararajan, G., *The Monkman-Grant relationship.* Materials Science and Engineering: A, 1989. **112**: p. 205-214.
94. Williams, M.L., R.F. Landel, and J.D. Ferry, *The Temperature Dependence of Relaxation Mechanisms in Amorphous Polymers and Other Glass-forming Liquids.* Journal of the American Chemical Society, 1955. **77**(14): p. 3701-3707.
95. McGarry, M., et al., *An octahedral shear strain-based measure of SNR for 3D MR elastography.* Physics in Medicine & Biology, 2011. **56**(13): p. N153.
96. Guedes, R.M., J.A. Simões, and J.L. Morais, *Viscoelastic behaviour and failure of bovine cancellous bone under constant strain rate.* Journal of Biomechanics, 2006. **39**(1): p. 49-60.
97. Reifsnider, K., et al., *Strain rate and temperature effects in polymeric matrices for composite materials.* Recent Developments in Durability Analysis of Composite Systems, 2000: p. 229-236.
98. Guedes, R., et al., *Response of CFRP Laminates under High Strain Rate Compression until Failure.* Science and Engineering of Composite Materials, 2005. **12**: p. 145-151.
99. Broughton, W. and G. Hinopoulos, *Evaluation of the single-lap joint using finite element analysis*. 1999: National Physical Laboratory. Great Britain, Centre for Materials ....
100. Her, S.-C. and C.-F. Chan, *Interfacial Stress Analysis of Adhesively Bonded Lap Joint.* Materials, 2019. **12**(15): p. 2403.
101. Jiang, X., et al., *Analysis on adhesively-bonded joints of FRP-steel composite bridge under combined loading: arcan test study and numerical modeling.* Polymers, 2016. **8**(1): p. 18.
102. Tsai, M. and J. Morton, *An evaluation of analytical and numerical solutions to the single-lap joint.* International Journal of Solids and Structures, 1994. **31**(18): p. 2537-2563.
103. Goland, M., *The stresses in cemented joints.* J. appl. Mech., 1944. **17**: p. 66.

104. Her, S.-C., *Stress analysis of adhesively-bonded lap joints.* Composite structures, 1999. **47**(1-4): p. 673-678.

105. Loureiro, A., et al., *Comparison of the mechanical behaviour between stiff and flexible adhesive joints for the automotive industry.* The Journal of Adhesion, 2010. **86**(7): p. 765-787.

106. Ju, M.L., et al. *A comparison among Polynomial model, Reduced polynomial model and Ogden model for polyurethane foam*. in *Advanced Materials Research*. 2014. Trans Tech Publ.

107. Nunes, L., *Mechanical characterization of hyperelastic polydimethylsiloxane by simple shear test.* Materials Science and Engineering: A, 2011. **528**(3): p. 1799-1804.

108. Shi, W., G. Liu, and Z. Chen, *Effects of the bulk compressibility on rubber isolator's compressive behaviors.* Advances in Mechanical Engineering, 2017. **9**(5): p. 1687814017699352.

109. Novoselov, K.S., et al., *Room-Temperature Quantum Hall Effect in Graphene.* Science, 2007. **315**(5817): p. 1379.

110. Novoselov, K.S., et al., *Unconventional quantum Hall effect and Berry's phase of 2π in bilayer graphene.* nature physics, 2006. **2**: p. 177-180.

111. Cheng, Q., et al., *Graphene and nanostructured MnO2 composite electrodes for supercapacitors.* Carbon, 2011. **49**: p. 2917-2925.

112. Liu, C., et al., *Graphene-Based Supercapacitor with and Ultrahigh Energy Density.* Nano Letters, 2010. **10**(12): p. 4863-4868.

113. Ye, D., et al., *Highly Efficient Electron Field Emission from Graphene Oxide Sheets Supported by Nickel Nanotip Arrays.* Nano Letters, 2012. **12**(3): p. 1265-1268.

114. Xu, Y., et al., *Flexible Graphene Films via the Filtration of Water-Soluble Noncovalent Functionalized Graphene Sheets.* Journal of American Chemical Society, 2008. **130**: p. 5856-5857.

115. Li, J., et al., *Efficient Inkjet Printing of Graphene.* Advanced Materials, 2013. **25**: p. 3985-3992.

116. Torrisi, F., et al., *Inkjet-Printed Graphene Electronics.* American Chemical Society, 2012. **6**(4): p. 2992-3006.

117. Kim, K.S., et al., *Large-scale pattern growth of graphene films for stretchable transparent electrodes.* Nature, 2009. **457**: p. 706-710.

118. Li, C., et al., *Graphene Nano-"patches" on a Carbon Nanotube Network for Highly Transparent/Conductive Thin Film Applications.* The Journal of Physical Chemistry C, 2010. **114**: p. 14008-14012.

119. Kim, Y. and D. Min, *Durable Large-Area Thin Films of Graphene/Carbon Nanotube Double Layers as a Transparent Electrode.* Langmuir Letter, 2009. **25**(19): p. 11302-11306.

120. Kim, S.H., et al., *Carbon Nanotube and Graphene Hybrid Thin Film for Transparent Electrodes and Field Effect Transistors.* Advanced Materials, 2014. **26**: p. 4247-4252.

121. Kholmanov, I.N., et al., *Optical, Electrical, and Electromechanical Properties of Hybrid Graphene/Carbon Nanotube Films.* Advanced Materials, 2015. **27**(19): p. 3053-3059.

122. Zheng, Q., et al., *Highly transparent and conducting ultralarge graphene oxide/single-walled carbon nanotube hybrid films produced by Langmuir-Blodgett assembly.* Journal of Materials Chemistry, 2012. **22**: p. 20572-20582.

123. Yan, Z., et al., *Rebar Graphene.* ACS Nano, 2014. **8**(5): p. 5061-5068.

124. Lin, X., et al., *Development of an ultra-thin film comprised of a graphene membrane and carbon nanotube vein support.* nature communications, 2013. **4**.

125. Sun, H., et al., *Novel Graphene/Carbon Nanotube Composite Fibers for Efficient Wire-Shaped Miniature Energy Devices.* Advanced Materials, 2014. **26**(18).

126. Peng, L., et al., *Transparent, Conductive, and Flexible Multiwalled Carbon Nanotube/Graphene Hybrid Electrodes with Two Three-Dimensional Microstructures.* The Journal of Physical Chemistry C, 2012. **116**: p. 4970-4978.

127. Xin, G., et al., *A graphene sheet exfoliated with microwave irradiation and interlinked by carbon nanotubes for high-performance transparent flexible electrodes.* Nanotechnology, 2010. **21**(40): p. 405201(1-7).

128. Lv, R., E. Cruz-Silva, and M. Terrones, *Building Complex Hybrid Carbon Architectures by Covalent Interconnections: Graphene-Nanotube Hybrids and MoreACS.* ACS Nano, 2014. **8**(5): p. 4061-4069.

129. Hong, T., et al., *Transparent, Flexible Conducting Hybrid Multilayer Thin Films of Multiwalled Carbon Nanotubes with Graphene Nanosheets.* ACS Nano, 2010. **4**(7): p. 3861-3868.

130. Huang, Z., et al., *Self-assembled reduced graphene oxide/carbon nanotube thin films as electrodes for supercapacitors.* Journal of Materials Chemistry, 2012. **22**: p. 3591-3599.

131. Singh, M., et al., *Inkjet Printing—Process and Its Applications.* Advanced Materials, 2010. **22**: p. 673-685.

132. Beecher, P., et al., *Ink-jet printing of carbon nanotube thin film transistors.* Journal of Applied Physics, 2007. **102**.

133. Secor, E., et al., *Inkjet Printing of High Conductivity, Flexible Graphene Patterns.* Physical Chemistry Letters, 2013. **4**: p. 1347-1351.

134. Kwon, Y., et al., *Improving dispersion of MWCNTs and graphenes using a common non-covalent modifier.* submitted to ACS Applied Materials and Interfaces, 2015.

135. Žeželj, M. and I. Stankovi´c, *From percolating to dense random stick networks: Conductivity model investigation.* Physical Review B, 2012. **86**(134202): p. 1-6.

136. Nirmalraj, P.N., et al., *Nanoscale Mapping of Electrical Resistivity and Connectivity in Graphene Strips and Networks.* Nano Letters, 2011. **11**: p. 16-22.

137. Komori, T. and K. Makishima, *Numbers of Fiber-to-Fiber Contacts in General Fiber Assemblies.* Textile research journal, 1977. **47**: p. 13-17.

138. Munson-McGee, S.H., *Estimation of the critical concentration in an anisotropic percolatin network.* Physical Review B, 1991. **43**(4): p. 3331-3336.

139. Hu, N., et al., *Effect of fabrication process on electrical properties of polymer/multi-wall carbon nanotube nanocomposites.* Composites Part A : Applied Science and Manufacturing, 2008. **39**: p. 893-903.

140. Fujifilm. *Materials Printer & Cartridge DMP-2800 series Printer & DMC-11600 Series Cartridge FAQs*. 2008; Available from: http://www.fujifilmusa.com/shared/bin/FAQs_DMP-2800_Series_Printer_DMC-11600+Series+Cartridge.pdf.

141. Denneulin, A., et al., *Impact of ink formulation on carbon nanotube network organization within inkjet printed conductive films.* Carbon, 2011. **49**: p. 2603-2614.

142. Ma, C., et al., *Study of the effect of curing residual stress on the bonding strength of the single lap joint using a high-temperature phosphate adhesive.* Materials, 2018. **11**(7): p. 1198.

143. Reedy, E. and T. Guess, *Butt joint strength: effect of residual stress and stress relaxation.* Journal of Adhesion Science and technology, 1996. **10**(1): p. 33-45.

144. Pak, S.Y., et al., *Measurement of residual stresses in polymeric parts by indentation method.* Polymer testing, 2013. **32**(5): p. 946-952.

145. Withers, P.J. and H. Bhadeshia, *Residual stress. Part 1–measurement techniques.* Materials science and Technology, 2001. **17**(4): p. 355-365.

146. Park, M., H. Kim, and J.P. Youngblood, *Strain-dependent electrical resistance of multi-walled carbon nanotube/polymer composite films.* Nanotechnology, 2008. **19**(5): p. 055705.

147. Zhao, J., et al., *A comparison between strain sensing behaviors of carbon black/polypropylene and carbon nanotubes/polypropylene electrically conductive composites.* Composites Part A: Applied Science and Manufacturing, 2013. **48**: p. 129-136.

148. Jung, Y.-T., et al., *Strain sensing and progressive failure monitoring of glass-fiber-reinforced composites using percolated carbon nanotube networks.* Functional Composites and Structures, 2020. **2**(1): p. 015006.

149. Yang, H., et al., *Strain-sensitive electrical conductivity of carbon nanotube-graphene-filled rubber composites under cyclic loading.* Nanoscale, 2019. **11**(2): p. 578-586.

150. Zhai, T., et al., *Piezoresistive and compression resistance relaxation behavior of water blown carbon nanotube/polyurethane composite foam.*

Composites Part A: Applied Science and Manufacturing, 2015. **72**: p. 108-114.

151. Gong, S., Z. Zhu, and S. Meguid, *Carbon nanotube agglomeration effect on piezoresistivity of polymer nanocomposites.* Polymer, 2014. **55**(21): p. 5488-5499.

152. Panozzo, F., M. Zappalorto, and M. Quaresimin, *Analytical model for the prediction of the piezoresistive behavior of CNT modified polymers.* Composites Part B: Engineering, 2017. **109**: p. 53-63.

153. Kuronuma, Y., et al., *Electrical resistance-based strain sensing in carbon nanotube/polymer composites under tension: Analytical modeling and experiments.* Composites Science and Technology, 2012. **72**(14): p. 1678-1682.

154. Li, D., et al., *Micro-contact reconstruction of adjacent carbon nanotubes in polymer matrix through annealing-Induced relaxation of interfacial residual stress and strain.* Journal of Applied Polymer Science, 2015. **132**(33).

155. Bao, W., et al., *Tunneling resistance and its effect on the electrical conductivity of carbon nanotube nanocomposites.* Journal of Applied Physics, 2012. **111**(9): p. 093726.

156. Sridhar, I. and K.R. Narayanan, *Processing and characterization of MWCNT reinforced aluminum matrix composites.* Journal of materials science, 2009. **44**(7): p. 1750-1756.

157. Li, C., E.T. Thostenson, and T.-W. Chou, *Dominant role of tunneling resistance in the electrical conductivity of carbon nanotube–based composites.* Applied Physics Letters, 2007. **91**(22): p. 223114.

158. Seo, D.-W., et al., *Enhancement in elastic modulus of GFRP bars by material hybridization.* Engineering, 2013. **5**(11): p. 865-869.

159. Logakis, E., et al., *Electrical/dielectric properties and conduction mechanism in melt processed polyamide/multi-walled carbon nanotubes composites.* Polymer, 2009. **50**(21): p. 5103-5111.

160. Neitzert, H.C., L. Vertuccio, and A. Sorrentino, *Epoxy/MWCNT composite as temperature sensor and electrical heating element.* IEEE transactions

on nanotechnology, 2010. **10**(4): p. 688-693.

# Korean abstract

탄소나노튜브(CNT)는 우수한 전기적 및 기계적 특성으로 인해 많은 구조적 및 전자적 응용 분야에서 연구되었다. CNT가 강화제로서 복합재의 충전제로서 사용될 수 있음이 많은 연구에서 드러났다. CNT/고분자 복합재는 압 저항 거동을 보이며 변형 감지 분야에 적용 가능하다. CNT 복합재는 구조적 건강 상태 모니터링 목적을 위한 접착제로 사용될 것으로 기대된다. 이 연구에서는 CNT 복합재의 응력 완화 동안 저항 변화 거동을 실험적, 이론적으로 나타내고 이를 활용하여 잔류응력을 나타내는 것을 목표로 하였다. 이 목적을 달성하기 위해 다음과 같은 연구들이 진행되었다.

접착제의 기계적 거동을 예측하는 것은 중요하다. 왜냐하면 접착제는 접착구조의 파괴강도 및 신뢰성에 큰 영향을 주기 때문이다. 파단 강도 등 접착제의 기계적 거동에 대한 속도 및 온도 의존성을 연구하였다. ABAQUS 소프트웨어에서 3D 구현을 위한 Schapery의 비선형 점탄성 모델을 도출하였고 이를 이용하여 접착제의 거동을 해석하였다. 모델의 파라미터들을 구하기 위해 기계적 분석(DMA)와 랩 조인트 시편의 응력 완화 시험을 하였다. 변형 속도에 따라 파괴할 때까지의 변형률이 다른 특성을 해석에 적용하였다. 여기에는 쉬프트 팩터와 여러 온도, 변형 속도에서의 랩 조인트 시편의 시험 결과를 사용하였다. 다양한 변형속도, 온도에서 접착제가 파괴가 일어날 때까지의 접착제의 거동을 시뮬레이션으로 나타냈고 실험과 비교하여 이 접근 방법이 유효하다는 것을 보였다.

CNT/그래핀 하이브리드의 전기적 특성이 연구되었다. 이 연구에서, CNT/그래핀 하이브리드에서 CNT와 그래핀이 시너지 효과를 내는 것을 정량적으로 예측할 수 있는 모델을 제안하였다. CNT-CNT, 그래핀-그

래핀, 그래핀-CNT의 접촉점 수는 하이브리드에서 입자가 랜덤하게 분포되어 있다고 가정하고 계산하였다. 이 계산 결과는 특정 CNT/그래핀 비율에서 최적의 전기전도도가 나온다는 것을 보여주었다. 이 계산 결과는 잉크젯 프린팅으로 만든 CNT/그래핀 하이브리드 필름의 전기전도도를 측정하여 실험적으로 입증되었다.

마지막으로 응력 완화가 일어나는 동안 CNT/고분자 복합재의 전기전도도 변화에 대해 연구하였다. 이 저항 변화가 CNT 종횡비, 농도와 어떤 연관이 있는지에 대해 연구하였다. CNT/에폭시 복합재를 만들어 응력 완화 시험을 하면서 저항을 동시에 측정하였다. CNT 종횡비와 농도에 따라 저항 변화 거동이 달라지는 것을 확인하였다. 이 거동을 설명하기 위해 새로운 저항 모델과 터널링 거리 내의 CNT 사이 접촉점 수를 기반으로 한 시뮬레이션 모델을 개발하였다. 이 모델을 사용하여 인장 시험하는 동안 저항 변화가 CNT 종횡비, 농도에 따라 달라지는 현상 또한 설명할 수 있었다. 또한 CNT 복합재를 접착제로 사용하여 온도를 낮추는 동안 생기는 잔류 응력을 측정하는 데에 사용하였다. 점탄성 모델을 사용한 시뮬레이션 결과에서 나온 접착제에 발생한 응력 변화는 실험에서 측정한 저항 변화와 비슷한 경향을 보였다. 이를 통해 CNT 복합재를 사용하여 접착제의 구조 안정성 모니터링과 잔류 응력 변화를 측정하는 데에 활용할 수 있다는 것을 보였다.

핵심어: 탄소나노튜브/고분자 복합재, 압저항 현상, 점탄성, 응력 완화, 전기전도도

학번: 2014-21444